NASA Contractor Report 166078

NASA-CR-166078
19850021605

Nonlinear Potential Analysis Techniques For Supersonic/ Hypersonic Configuration Design

W. C. Clever and V. Shankar

ROCKWELL INTERNATIONAL CORPORATION
Los Angeles, California 90009

CONTRACT NASI-15820
MARCH 28, 1983

NASA
National Aeronautics and Space Administration

Langley Research Center
Hampton Virginia 23665

NASA Contractor Report 166078

NONLINEAR POTENTIAL ANALYSIS TECHNIQUES FOR SUPERSONIC/ HYPERSONIC CONFIGURATION DESIGN

W. C. Clever and V. Shankar

ROCKWELL INTERNATIONAL CORPORATION
Los Angeles, California 90009

CONTRACT NAS1-15820
MARCH 28, 1983

FOREWORD

This final report was prepared by the Los Angeles Aerodynamics Group and the Science Center of Rockwell International, Los Angeles, California for the Langley Research Center, National Aeronautics and Space Administration, Hampton, Virginia. The work was performed under Contract No. NAS1-15820, "Development of Second Order Potential Analysis/Design and Full Potential Analysis Aero Prediction Technology for Hypersonic Configuration Design." Mr. Noel Talcott and Mr. Kenneth Jones were the Project Monitors of this contract.

Mr. E. Bonner was the Program Manager; Drs. W. C. Clever and V. Shankar were the Principal Investigators.

SUMMARY

Approximate nonlinear inviscid theoretical techniques for predicting aerodynamic characteristics and surface pressures for relatively slender vehicles at moderate hypersonic speeds were developed. Emphasis was placed on approaches that would be responsive to preliminary configuration design level of effort. Second order small disturbance and full potential theory was utilized to meet this objective.

Numerical pilot codes were developed for relatively general three dimensional geometries to evaluate the capability of the approximate equations of motion considered. Results from the computations indicate good agreement with higher order solutions and experimental results for a variety of wing, body, and wing-body shapes for values of the hypersonic similarity parameter $M\delta$ approaching one. Case computational times of a minute were achieved for practical aircraft arrangements.

TABLE OF CONTENTS

1. INTRODUCTION

An examination of the literature for airbreathing hypersonic concepts provides an indication of the flexibility and generality required for a prediction technique. Typical configuration development variables include wing section, incidence, height, dihedral, planform, effectiveness of longitudinal control surfaces for trim, effectiveness of empennage for directional stability, and propulsion system-airframe interactions.

State-of-the-art response to these prediction requirements is provided by hypersonic impact methods as well as linearized analysis and design algorithms. These approaches can treat complex geometries with minimum response time and cost, with efficient predicted data coverage in terms of Mach number, angle of attack, trim deflection, yaw angle, etc. Shortcomings are present, however, in both the impact and linearized methods. For the former, interference between surface elements is totally ignored in implementations such as classical Newtonian, tangent wedge, and cone theories. Cross-flow interactions and stagnation point singularities are also implicitly disregarded. In the latter, shocks, vorticity, and entropy wakes and layers are excluded. Furthermore, superposition of elementary solutions such as those for thickness and angle of attack freely used in linear models are, strictly speaking, invalid at hypersonic speeds.

A need exists for new aerodynamic prediction techniques to optimize vehicles designed to travel at supersonic/hypersonic speeds. One requirement of a new aerodynamic prediction is that it be more accurate than simple non-interfering panel methods. Another specification is that it be more computationally efficient than currently available explicit finite-difference methods so that it can be incorporated into a practical design procedure. The new approach should include enough of the physics of the flow to allow realistic optimization and should permit consideration of appropriate interactions between components of promising hypersonic arrangements, since this has been found to be the key to increasing aerodynamic efficiency at supersonic speeds. Nonlinear potential theoretical formulations hold the promise of meeting this objective and providing economic design codes which are responsive to preliminary vehicle definition efforts.

2. LIST OF SYMBOLS*

AR	aspect ratio, b^2/S
b	wing span
c	chord
$\bar{c}$	mean aerodynamic chord
C_D	drag coefficient, $\frac{D}{qS}$
C_L	lift coefficient, $\frac{L}{qS}$
C_m	pitching moment coefficient $\frac{M}{qS\bar{c}}$
C_p	pressure coefficient, $\frac{P-P_\infty}{q_\infty}$
D	drag
e	unit normal
k	second order coefficient,
L	lift
M	Mach number or pitching moment
n	normal
P	static pressure
q	dynamic pressure
S	reference area
t	maximum thickness
u,v,w	axial, lateral, and vertical perturbation velocity
x,y,z	axial, lateral, vertical body axis cartesian coordinates
α	angle of attack
β	$\sqrt{M^2_\infty-1}$
γ	ratio of specific heats

δ	flow deflection angle
η	wing span station/(b/2)
θ	dihedral angle of aerodynamic surface
λ	taper ratio, c_t/c_r
Λ	sweep
ϕ	first order velocity perturbation potential
$\phi^{(2)}$	second order velocity perturbation potential
Φ	total velocity potential
ψ (x,y)	surface displacement

SUBSCRIPTS

ac	aerodynamic center
b	body
LE	leading edge
r	root
t	tip
x,y,z	derivative with respect to x,y,z respectively
ℓ	lower surface
u	upper surface
c,γ	camber
t,τ	thickness
n	normal
∞	free stream
α	angle of attack

*Additional specialized nomenclature is defined in the theoretical sections at the point of introduction

3. METHODOLOGY

Emphasis is placed on approximate theoretical approaches which are capable of treating relatively general three dimensional problems but still sufficiently simple to be responsive to vehicle preliminary design efforts. The basic intent of the methodology is to produce improvement in lift-drag ratio of hypersonic cruise vehicles. As a result of the strong impact that favorable interference has had on supersonic design and the use of such concepts in recent advanced hypersonic aircraft studies, candidate analysis should be general enough to systematically treat such problems. Finally, interest in high aerodynamic efficiency emphasizes relatively slender configurations at modest angle of attack; that is, moderate values of the hypersonic similarity parameter.

Prior theoretical effort[1,2] has advanced the supersonic/hypersonic aerodynamic prediction state-of-the-art at the preliminary design level. Numerical second-order potential small disturbance analysis was developed as a first step up from the widely used linear theory. Such a formulation incorporates nonlinear behavior by iteration of the Prandtl-Glauert approximation. This approach is known to extend the prediction success for airfoil and cone surface pressure to substantially higher values of the hypersonic similarity parameter than the first-order theory. A typical three-dimensional prediction improvement provided by the numerical second-order analysis[2] is presented in figures 3.1 and 3.2. These results support extensions to treat multiple-surface analysis and wing-body design problems in the present study. The next level of theoretical richness vis-a-vis a full-potential equation of motion formulation was explored in parallel[2]. This analysis eliminates edge singularities and improves treatment of characteristic surfaces but still retains the isentropic assumption. Typical prediction success for a conical wing-body is presented in figure 3.3. These results indicate sufficient promise to pursue extension of the analysis to general wing-body configurations.

Hypersonic small disturbance theory was considered in an earlier study[1] in recognition of the progressive non-isentropic behavior of the flow as the value of the hypersonic similarity parameter increases. Finite difference analysis of this approximation[3] indicated that the solution was essentially as complex as that for the Euler equation and thus would not be particularly responsive to preliminary design level of effort. This approach was not pursued in the present study on the basis of this finding and the previously cited success of potential analysis at moderate hypersonic conditions.

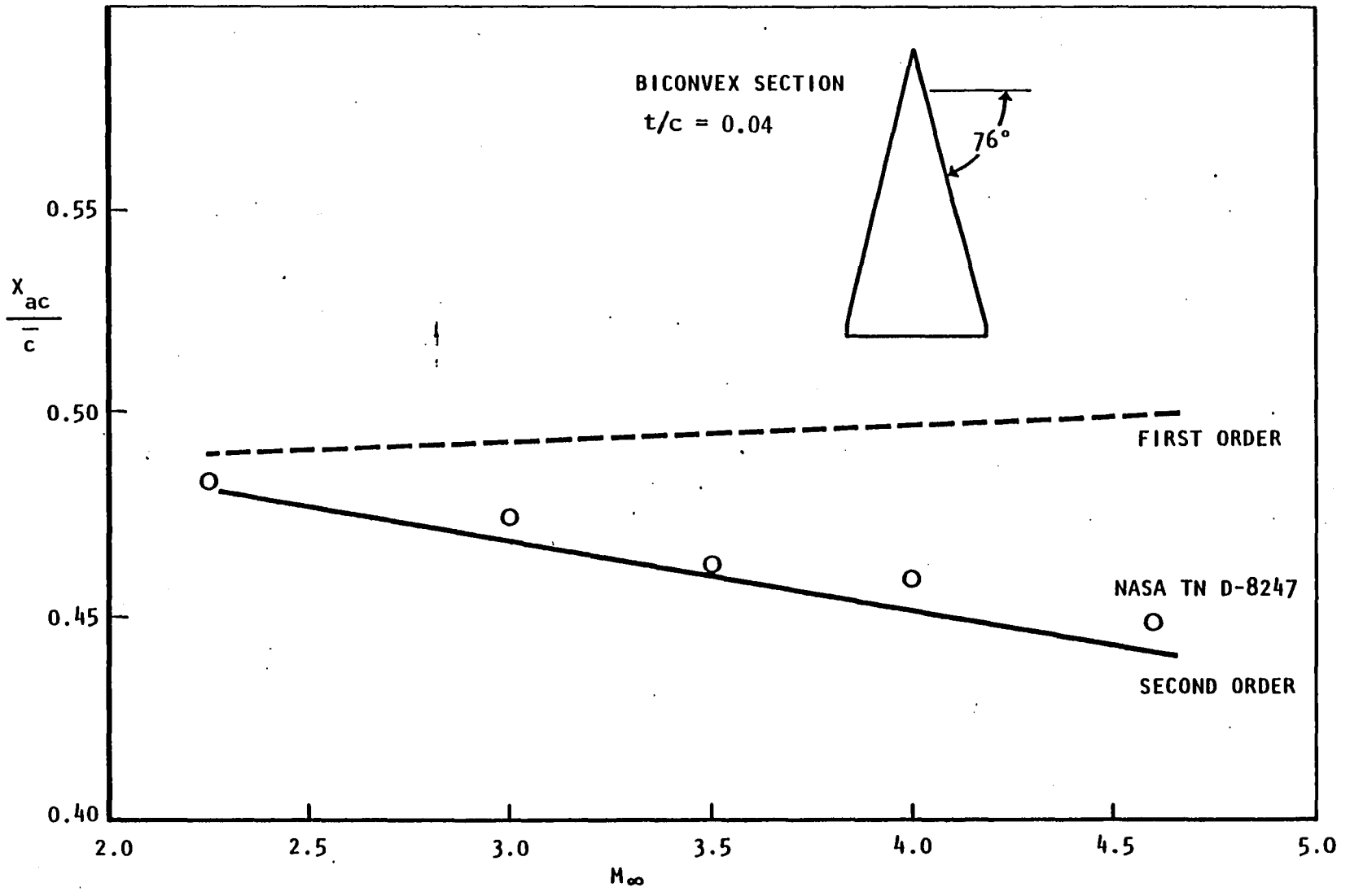

Figure 3.1. Predicted Aerodynamic Center Location of a Subsonic Edge Delta Wing

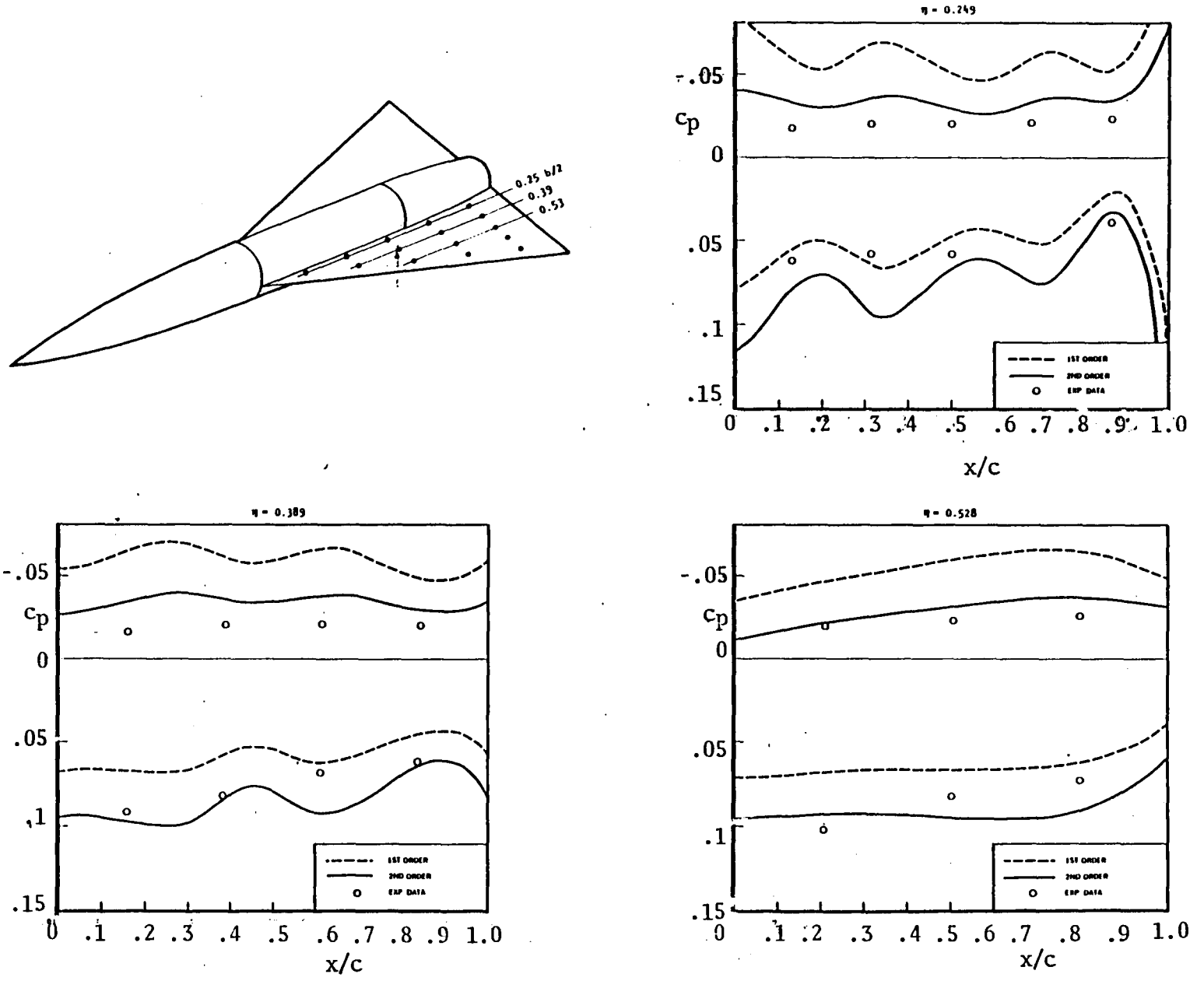

Figure 3.2. Comparison of Wing Surface Pressures in Presence of Body at M = 6, α = 8°

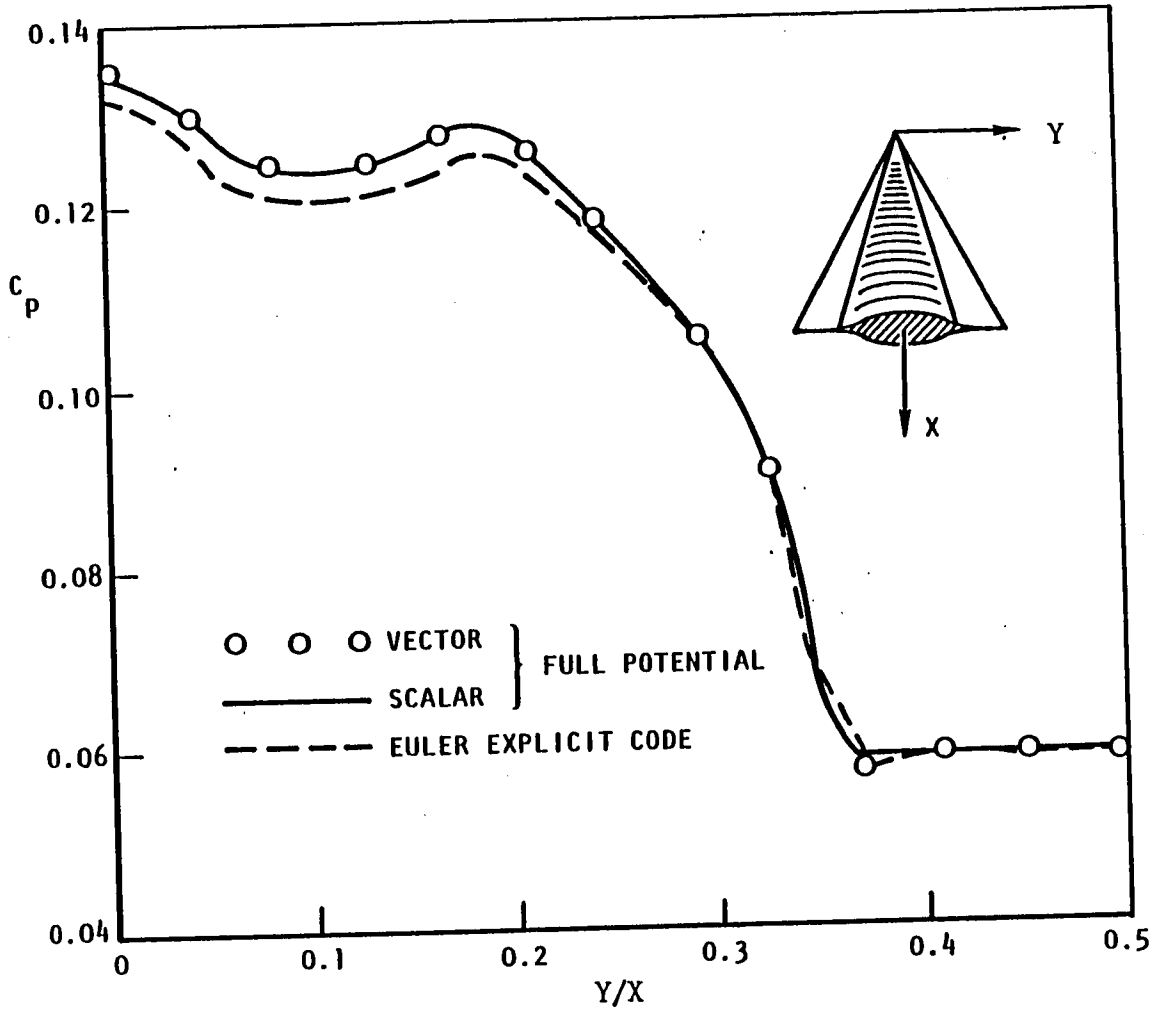

Figure 3.3. Predicted Compression Surface Pressures for a Conical Wing-Body at $M_\infty = 4$, $\alpha = 5°$

4. SECOND ORDER POTENTIAL ANALYSIS/DESIGN

4.1 APPROACH

The solution accurate to second order for the flow around wing-body combinations of aerodynamic interest may be represented by the velocity potential, Φ , written as the sum of the first and second order velocity potentials.

$$\Phi(x,y,z) = \phi(x,y,z) + \phi^{(2)}(x,y,z)$$

The condition of no flow through the boundary requires that

$$[\ \cos\alpha_\infty\, \vec{e}_x + \sin\alpha_\infty\, \vec{e}_z + \nabla\Phi\ ]\cdot\vec{n} = 0$$

on the surface of the configuration. The solution , ϕ, accurate to first order, must satisfy the Prandtl-Glauert equation,

$$\Box^2\phi = \left\{ (1-M_\infty^2)\frac{\partial^2}{\partial x^2} + \frac{\partial^2}{\partial y^2} + \frac{\partial^2}{\partial z^2} \right\} \phi = 0$$

and the the boundary condition

$$[\ \vec{e}_x + \alpha_\infty\, \vec{e}_z + \nabla\phi\ ]\cdot\vec{n} = 0$$

on the surface. For the configurations of interest the aerodynamic surfaces are assumed to be thin, and the first order boundary condition is satisfied on the mean camber line in accordance with thin wing theory.

$$\frac{\partial\phi}{\partial n} = \frac{\partial\Psi}{\partial x} - \alpha_\infty \cos\theta$$

where, θ, is the local dihedral angle and, $z = \Psi(x,y)$, is the equation for the surface deflection written in a coordinate system with the z axis perpendicular to the local mean camber plane, and the x and y axis located within this plane, with the x axis in the streamwise direction. To first order there is no effect on the solution if a distinction is made between the angle of attack of the freestream and the angle of attack of the

configuration. To second order there also should be no difference in the solution, but for numerical computation purposes a distinction should be made, and the angle of attack should be accounted for by α_∞, and not by $\Psi(x,y)$.

The method used to obtain a first order solution made use of axial singularities and quadrilateral source panels on the body surface in conjunction with quadrilateral source and vortex panels to represent the (thin) aerodynamic surfaces. The vortex panels, used to represent lift, were of constant strength, while the source panels, used to represent thickness, could be of constant strength or could be made to vary linearly in both the chordwise and spanwise directions. The vortex panel and body source panel strengths where obtained by solving a set of simultaneous linear equations and thereby satisfying the boundary conditions at a set of control points. The singularities used to simulate a multiple surface-body configuration are summarized on the following sketch.

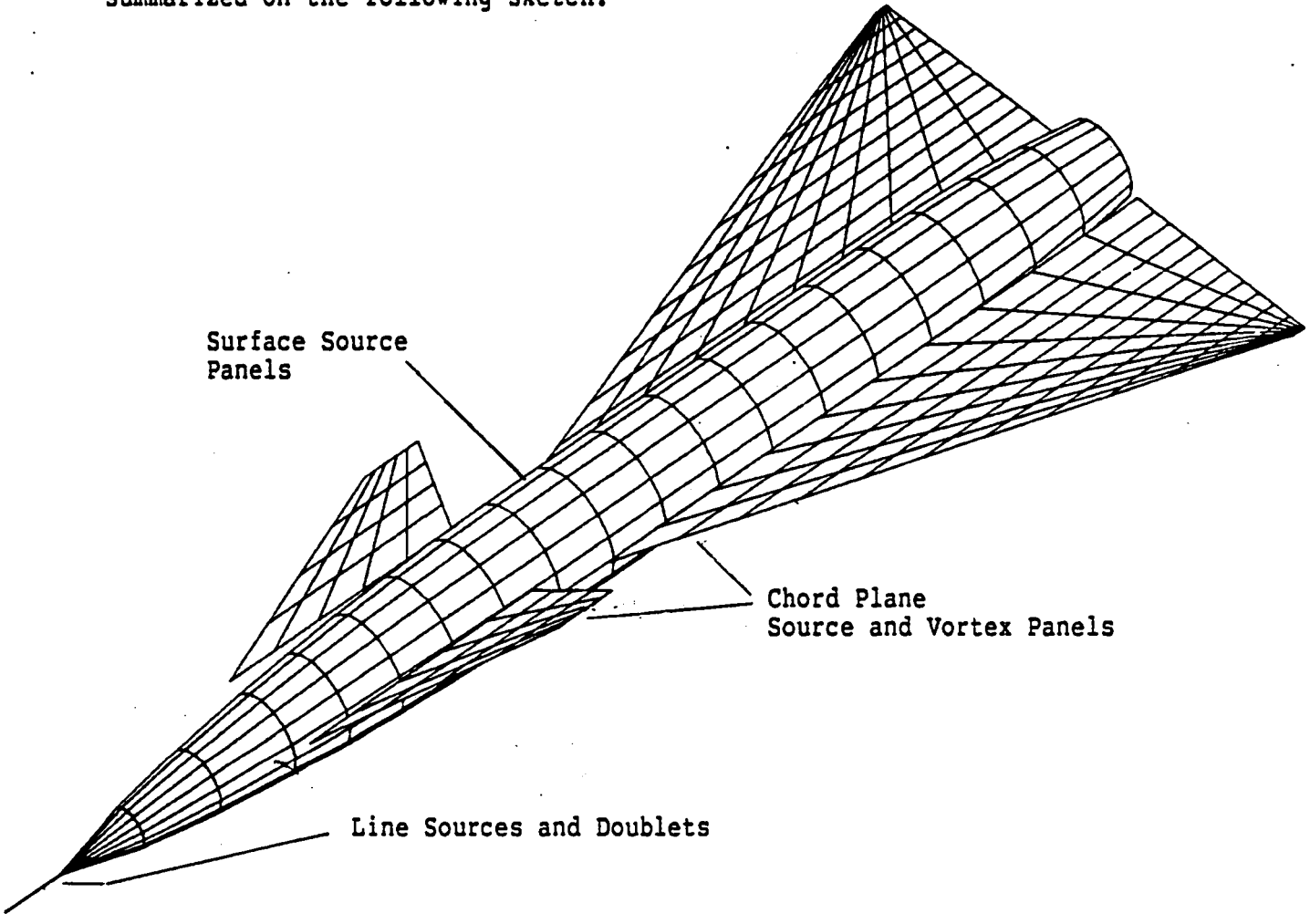

Distribution of Singularities on an Arbitrary Configuration

When the panel singularity strengths were obtained the first order flow properties could be determined anywhere in the field. The second order potential, $\phi^{(2)}$, utilizes the first order solution. It must satisfy the nonhomogeneous Prandtl-Glauert equation:

$$\Box^2 \phi^{(2)} = M_\infty^2 \frac{\partial}{\partial x}\left\{\left[(1-M_\infty^2) + \frac{\gamma+1}{2} M_\infty^2\right] \phi_x^2 + \phi_y^2 + \left[\phi_z + a_\infty\right]^2\right\}$$

as well as enable the boundary conditions to be satisfied to second order on the surface.

A second order solution using the source volume formulation described in reference 1, encounters numerical difficulties for complex configurations, wings with subsonic edges, and supersonic wing-body configurations. The primary reason is that source volume strengths require the calculation of spatial derivatives, and these cannot be obtained accurately enough from the first order solution when using the panel formulation. In addition the velocity discontinuities present in supersonic flow are accentuated, since the discontinuities introduced by the panel corners and edges do not attenuate with distance. Also no reasonable mesh density of spatial source volumes can properly account for the large gradients in flow properties near subsonic edges.

Therefore an approximate method which does not require the use of a spatial distribution of sources was developed. This method requires no calculation of flow properties off of the surface, and can be used even when large gradients are present (e.g. with subsonic edges). The method of solution is a three dimensional modification, based on an infinitely skewed wing transformation, of the exact second order solution for the pressure coefficient on thin airfoils in two dimensions. Using this method, the solution for the thin aerodynamic lifting surfaces is given by the following:

$$Cp(x,y) = -2\left\{\phi_x + k(M)\left[\tfrac{1}{2}(1-M_\infty^2)\phi_x^2 + \tfrac{1}{2}\phi_y^2 + \tfrac{1}{2}(\phi_z + a_\infty)^2 - \tfrac{1}{2}\alpha_\infty^2 + \Psi\phi_{xz} + \varphi_x\right]\right\}_{z=0}$$

where $\Box^2 \varphi = 0$, $k(M) = \dfrac{1}{(1-M^2)}\left\{1 + \dfrac{\gamma+1}{4}\dfrac{M^4}{(1-M^2)}\right\}$

and $\varphi_z(x,y,0) = (1-M_\infty^2)\,\phi_x \Psi_x + \phi_y \Psi_y + \Psi\left[(1-M_\infty^2)\,\phi_{xx} + \phi_{yy}\right]$

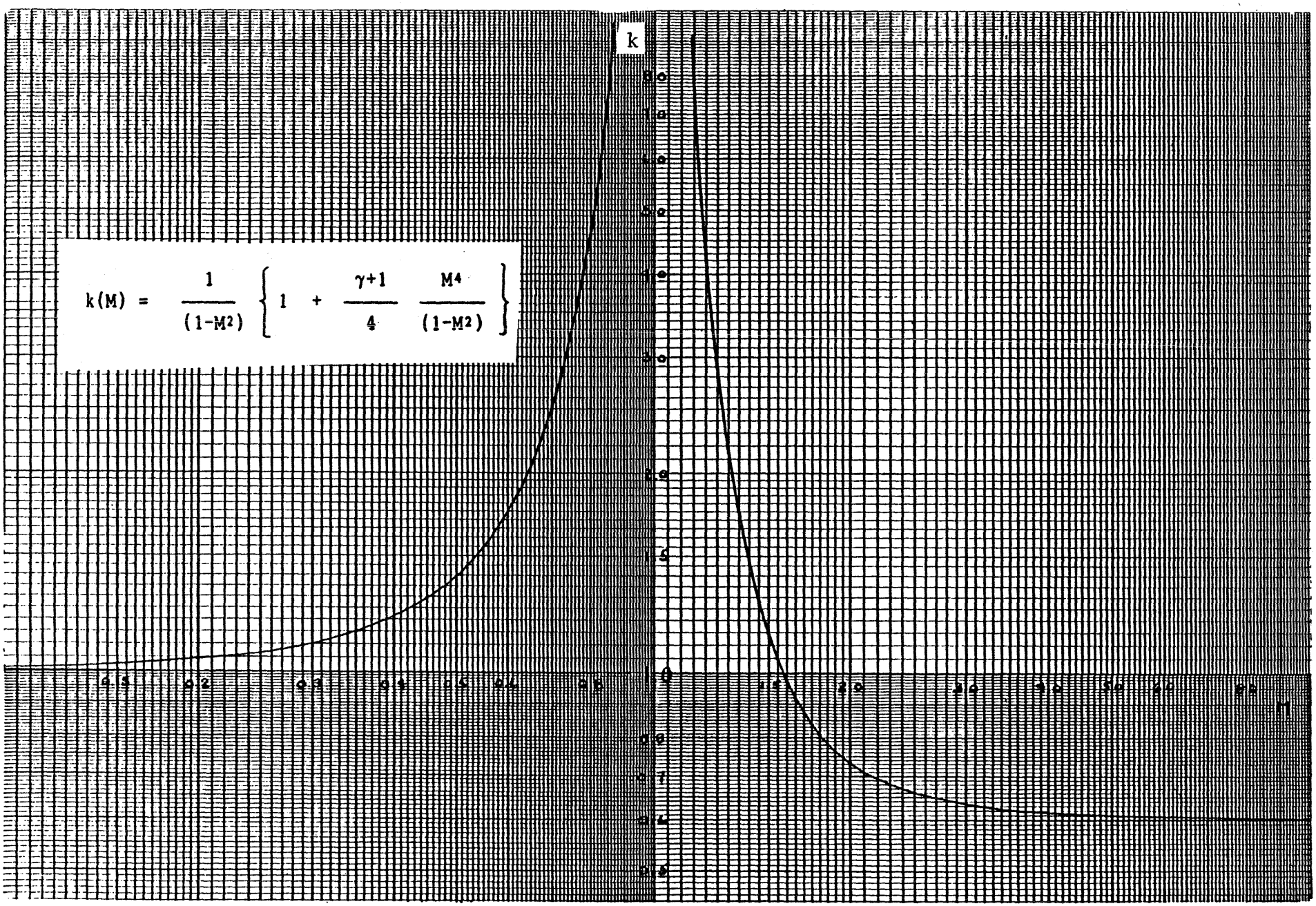

Figure 4.1.1. Second Order Coefficient k

$\Psi(x,y)$ represents the upper or lower surface of the airfoil. This solution, in effect, represents a local type solution, and all first order velocities represented above should be in a coordinate system rotated to make the z-axis normal to the local surface (e.g. with nonplanar configurations), but with no local angle of incidence.

When applied in three dimensions the transformed two dimensional equation should give the exact second order pressures whenever the flow is locally two dimensional and may be approximated by an infinite skewed system. The Mach number, M, used in calculating the coefficient k(M) is equal to

$$M_{\sim} = M_{\infty} \cos \Lambda \qquad \text{(i.e. the normal Mach number)}$$

Whenever $M = M_{\sim}$ is equal to unity, k(M) becomes infinite, indicating the second order solution is not valid near M = 1. If M_{∞} is used for calculating k(M) the solution remains finite except near $M_{\infty} = 1$. Since k(M) is a slowly varying function of M (see page 11), except near $M_{\infty} = 1$, $k(M_{\infty})$ can be substituted for $k(M_{\sim})$ without a significant change in the result.

The second order modifications to the pressure on the body are influenced only by the function φ used to satisfy the second order boundary condition. However, in a sense, the second order requirements on the body are not as stringent as on the aerodynamic surfaces, since the boundary conditions on the body are satisfied on the actual surface, rather than the mean camber line. In addition the nonlinear expression for Cp in terms of the velocities is used on the body. The terms missing from the complete second order solution on the body are due to the spatial term in the non-homogeneous Prandtl-Glauert equation for $\phi^{(2)}$.

4.2 FULL CONFIGURATION ANALYSIS

The first order solution is obtained by solving for the panel strengths required to satisfy the first order boundary conditions. The panel strengths enable the calculation of first order perturbation velocities, used for the calculation of second order velocities, at panel control points. Since the first order solution is linear, the solution and the resulting perturbation velocities can be considered to be the appropriate sum of the following four basic solutions:

1. Contributions from all panels due to an incremental change in angle of attack (add load velocities).
2. The incremental contribution from all panels due to the twist and camber of the aerodynamic surfaces.
3. The velocity perturbations due to thickness.
4. The velocity perturbations due to the body in axial flow.

On the thin lifting surfaces, (chord plane vortex panels), some components have an odd or even part with respect to the local z = 0 plane. Odd symmetry terms are those which are of equal magnitide but of opposite sign across the z = 0 plane, while even symmetry terms are those which are continuous across the z = 0 plane. Therefore if we define:

α = angle of attack of the free stream.

γ = a camber coefficient (= 1.0 for camber, = 0.0 without)

τ = thickness coefficient (= 1.0 with, = 0.0 without)

b = body contribution

Then we can write,

$$u = \phi_x = \alpha \left(u_\alpha \pm \tfrac{1}{2}\Delta u_\alpha \right) + \gamma \left(u_\gamma \pm \tfrac{1}{2}\Delta u_\gamma \right) + \tau \left(u_\tau \pm \tfrac{1}{2}\Delta u_\tau \right) + \left(u_b \pm \tfrac{1}{2}\Delta u_b \right)$$

$$v = \phi_y = \alpha \left(v_\alpha \pm \tfrac{1}{2}\Delta v_\alpha \right) + \gamma \left(v_\gamma \pm \tfrac{1}{2}\Delta v_\gamma \right) + \tau \left(v_\tau \pm \tfrac{1}{2}\Delta v_\tau \right) + \left(v_b \pm \tfrac{1}{2}\Delta v_b \right)$$

$$w = \phi_z = \alpha w_\alpha + \gamma w_\gamma + \tau \left(\pm \Psi_{\tau_x} \right)$$

where ± indicate upper or lower surface. The contributions having a ± have an odd symmetry with respect to the local z = 0 plane.

The surface displacements Ψ are composed of three parts.

1. Displacements due to angle of attack of the configuration.
2. Displacements due to twist and camber.
3. Displacements due to thickness.

Therefore we can write,

$$\Psi = \alpha \Psi_\alpha + \gamma \Psi_\gamma \pm \tau \Psi_\tau$$

All contributions to the second order terms are composed of products of first order terms. These terms will have either an odd or an even symmetry with respect to the local z = 0 plane. The odd symmetry terms in the Cp expression contribute to a ΔCp across the aerodynamic surface while the even symmetry terms contribute to an equal Cp on each side. Therefore since,

$$Cp = -2\,k(M)\left\{ \tfrac{1}{2}(1-M_\infty^2)\phi_x^2 + \tfrac{1}{2}\phi_y^2 + \tfrac{1}{2}(\phi_z + a_\infty)^2 - \tfrac{1}{2}a_\infty^2 + \Psi\phi_{zx} + \Phi_x \right\}$$

where the boundary condition for the potential function $\varphi(x,y,z)$, used to satisfy the second order boundary condition is,

$$\varphi_z(x,y,0) = (1-M_\infty^2)\phi_x \Psi_x + \phi_y \Psi_y + \Psi\,[\,(1-M_\infty^2)\phi_{xx} + \phi_{yy}\,]$$

with

$$\Box^2\varphi(x,y,z) = 0$$

we can write the expression for the second order contribution to ΔCp as:

$$\Delta Cp^{(2)} = -2\,k(M)\Big\{(1-M^2)\,[au_\alpha + \gamma u_\gamma + \tau u_\tau + u_b][a\Delta u_\alpha + \gamma\Delta u_\gamma + \tau\Delta u_\tau + \Delta u_b]$$

$$+ [av_\alpha + \gamma v_\gamma + \tau v_\tau + v_b][a\Delta v_\alpha + \gamma\Delta v_\gamma + \tau\Delta v_\tau + \Delta v_b]$$

$$+ 2\,\gamma\tau\,[\,w_\gamma \Psi_{\tau_x} + w_{\gamma_x}\Psi_\tau + \Psi_\gamma \Psi_{\tau_{xx}}] + \Delta\,\varphi_x\Big\}$$

where

$$\varphi_z = (1-M_\infty^2)[\gamma\,\Psi_{\gamma_x}(au_\alpha + \gamma u_\gamma + \tau u_\tau + u_b) + \tfrac{1}{2}\tau\Psi_{\tau_x}(a\Delta u_\alpha + \gamma\Delta u_\gamma + \tau\Delta u_\tau + \Delta u_b)$$

$$+ \gamma\,\Psi_{\gamma_y}(av_\alpha + \gamma v_\gamma + \tau v_\tau + v_b) + \tfrac{1}{2}\tau\Psi_{\tau_y}(a\Delta v_\alpha + \gamma\Delta v_\gamma + \tau\Delta v_\tau + \Delta v_b)]$$

$$+ \gamma\,\Psi_\gamma[(1-M_\infty^2)(au_{\alpha_x} + \gamma u_{\gamma_x} + \tau u_{\tau_x} + u_{b_x}) + (av_{\alpha_y} + \gamma v_{\gamma_y} + \tau v_{\tau_y} + v_{b_y})]$$

$$+ \tfrac{1}{2}\tau\Psi_\tau[(1-M_\infty^2)(a\Delta u_{\alpha_x} + \gamma\Delta u_{\gamma_x} + \tau\Delta u_{\tau_x} + \Delta u_{b_x}) + (a\Delta v_{\alpha_y} + \gamma\Delta v_{\gamma_y} + t\Delta v_{\tau_y} + \Delta v_{b_y})]$$

The expression φ_x is calculated by differentiating the solution for the function φ which is used to satisfy the boundary conditions to second order. The odd symmetry second order boundary conditions will be satisfied by a solution using source (thickness) panels, while the even symmetry second order boundary conditions will be satisfied using vortex panels and will contribute to a net ΔCp across the surface.

By setting the various coefficients a, γ, or τ equal to zero, the second

order effect of various combinations of angle of attack, camber ($\gamma = 1.0$) or no camber ($\gamma = 0.0$), and thickness ($\tau = 1.0$) or no thickness ($\tau = 0.0$), may be analyzed from the basic solutions. The term Δu_τ comes from the lift generated by the thickness and is generally small, and in fact is zero for planar configurations. The term Δu_b constitutes the lift induced by the body in axial flow and is also, in general, small. For planar configurations or when there is symmetry about the z = 0 plane, the velocity expressions simplify,

$$u = \phi_x = \alpha \left(u_\alpha \pm \tfrac{1}{2}\Delta u_\alpha \right) + \gamma \left(u_\gamma \pm \tfrac{1}{2}\Delta u_\gamma \right) + \tau\, u_\tau$$

$$v = \phi_y = \alpha \left(v_\alpha \pm \tfrac{1}{2}\Delta v_\alpha \right) + \gamma \left(v_\gamma \pm \tfrac{1}{2}\Delta v_\gamma \right) + \tau\, v_\tau$$

$$w = \phi_z = \alpha\, w_\alpha + \gamma\, w_\gamma \pm \tfrac{1}{2}\tau \Delta\Psi_{\tau_x}$$

4.3 WING-BODY DRAG OPTIMIZATION

4.3.1 Force Calculation

The first or second order formulations for the near field force determination for any configuration are similar. Basically the calculation involves multiplying the local value of Cp times the projected area. The lift and drag coefficients can be written as integrals of the pressure coefficient over the surface area.

$$C_L = - \iint Cp\, n_z\, dS$$

$$C_D = - \iint Cp\, n_x\, dS$$

where the local normal is $\vec{n} = (n_x, n_y, n_z)$

In general for thin aerodynamic lifting surfaces,

$$\text{drag/area} = (Cp_u w_u - Cp_l w_l)$$

$$= - 0.5 (Cp_l - Cp_u) (w_u + w_l)$$

$$+ 0.5 (Cp_l + Cp_u) (w_u - w_l)$$

$$= - \Delta Cp \, w_c + 2 \overline{Cp} \, w_t$$

where u and l refer to upper and lower surfaces, and:

$wv = 0.5 (w_u + w_l)$ (camber normal velocity)

$wt = 0.5 (w_u - w_l)$ (thickness normal velocity)

$\Delta Cp = (Cp_l - Cp_u)$ (normal force Cp)

$2 \overline{Cp} = (Cp_l + Cp_u)$ (even symmetry Cp)

Using this formulation the integrals may be changed to a sum over all vortex and thickness panels, which are used on the aerodynamic surfaces, and over all source panels, which are used on the body.

$$C_L = \sum_{i=1}^{NTV} \Delta Cp_i \cos\theta_i \, Pa_i - \sum_{i=1}^{NTB} Cpb_i \, nz_i \, Pab_i$$

$$C_D = - \sum_{i=1}^{NTV} \Delta Cp_i \, wv_i \, Pa_i - \sum_{i=1}^{NTB} Cpb_i \, nx_i \, Pab_i$$

$$- 2 \sum_{i=1}^{NTV} \overline{Cp}_i \, wt_i \, Pa_i$$

where

ΔCp_i = the Cp across vortex panel i.

$\overline{Cp}_i$ = the even symmetry Cp on vortex (or source) panel i.

Cpb_i = the local Cp on the body source panel i.

wv_i = the camber normal velocity on panel i.

wt_i = the thickness normal velocity on panel i.

$\cos\theta_i$ = the cosine of the dihedral angle of vortex panel i.

nx_i = the x component of the normal of body panel i.

nz_i = the z component of the normal of body panel i.

Pa_i = the (area / reference area) of panel i.

Pab_i = the (area / reference area) body source panel i.

On each panel the odd symmetry normal velocity, wt, is due to the thickness, while the even symmetry normal velocity, wv, is primarily due to camber (or angle of attack). The total number of vortex panels used to represent the configuration is equal to NTV, and the total number of body panels is equal to NTB. The Cp's on the vortex (or thickness) panels may be further divided into Cp's of order one and two.

$$\Delta Cp = \Delta Cp^{(1)} + \Delta Cp^{(2)}$$

$$\overline{Cp} = \overline{Cp}^{(1)} + \overline{Cp}^{(2)}$$

The Cp on the body, Cpb_i, can be written in terms of the induced velocities. To first order:

$$Cpb_i = -2\,Ux_i$$

where the perturbation velocity at the control point of panel i is:

$$\vec{U}_i = (Ux_i, Uy_i, Uz_i) \quad \text{and} \quad \vec{U}_i \cdot \vec{n} = Un_i$$

If desired, higher order formulas may be used, although in the present formulation the velocities induced on the body are not fully accurate to second order.

In performing the optimization we can assume the thickness distribution and body geometry to be given. The optimization procedure consists of finding the body angle of attack and, the twist and camber of all lifting surfaces. This optimum results in a minimum value for the drag expression, while satisfying a set of constraints on lift coefficient, center of pressure, etc.

4.3.2 First Order Optimization

To first order the thickness drag is nearly independent of lift, and therefore may be neglected in any optimization procedure. Therefore only the induced ΔCp's on the vortex (thickness) panels must be considered. These panel ΔCp's will be simply written as Cp_i. For a fixed body geometry, the local angle of attack at the vortex panel control points, Un_i, and the body angle of attack α, may comprise a set of independent variables. Then a set of dependent variables which may be solved for are:

1. The vortex panel strengths Cp_j $\quad j=1,NTV$

2. The source panel strengths σ_j $\quad j=1,NTB$

where NTV and NTB are the total numbers of vortex and source panels respectively. The equations used for the solution are the conditions of flow tangency at the vortex and source panel control points. Using the computed aerodynamic influence coefficients, A, for each panel we can express the normal velocity on each panel in the form:

$$Un_i = \sum_{j=1}^{NTV} An_{ij} Cp_j + \sum_{l=1}^{NTB} Anb_{il} \sigma_l \qquad i=1,NTP$$

where NTP = NTV + NTB

Alternately, the source strengths σ, can be solved for as a function of the Cp's on the vortex panels, and α.

$$\sum_{l=1}^{NTB} Anb_{il} \sigma_l = \sum_{j=1}^{NTV} An_{ij} Cp_j - nz_i \alpha \qquad i=1,NTB$$

or

$$\sigma_l = \sum_{j=1}^{NTV} B_{lj} Cp_j - B_{lm} \alpha \qquad l=1,NTB$$

where m = NTV + 1

This means we can consider the independent variables to be the Cp's on the vortex panels and α:

$$(Cp_j, \alpha) \qquad j = 1, NTV$$

Everything of interest may be written in terms of these variables. For example, using the aerodynamic influence coefficients for the x-velocity, we can express the x-velocities in terms of the dependent variables:

$$Ux_i = \sum_{j=1}^{NTV} Ax_{ij} Cp_j + \sum_{l=1}^{NTB} Axb_{il} \sigma_l \qquad i=1,NTP$$

becomes

$$Ux_i = \sum_{j=1}^{NTV} Ax_{ij} Cp_j + \sum_{\ell=1}^{NTB} Axb_{i\ell} \left[\sum_{j=1}^{NTV} B_{\ell j} Cp_j - B_{\ell m} \alpha \right]$$

$$= \sum_{j=1}^{NTV} \left[Ax_{ij} + \sum_{\ell=1}^{NTB} Axb_{i\ell} B_{\ell j} \right] Cp_j - \sum_{\ell=1}^{NTB} Axb_{i\ell} B_{\ell m} \alpha$$

$$= \sum_{j=1}^{NTV} Bx_{ij} Cp_j + Bx_{im} \alpha$$

or, since on the body panels, $Cpb_i = -2\, Ux_i$

$$Cpb_i = \sum_{j=1}^{NTV} Bp_{ij} Cp_j + Bp_{im} \alpha$$

and

$$C_L = \sum_{i=1}^{NTV} Cp_i \cos\theta_i Pa_i - \sum_{i=1}^{NTB} Cpb_i nz_i Pab_i$$

becomes

$$C_L = \sum_{i=1}^{NTV} Cp_i \cos\theta_i Pa_i$$

$$- \sum_{i=1}^{NTB} nz_i Pab_i \left(\sum_{j=1}^{NTV} Bp_{ij} Cp_j + Bp_{im} \alpha \right)$$

The drag coefficient may be written as a quadratic function of the set of independent variables (Cp_j, α).

$$C_D = -\sum_{i=1}^{NTV} Cp_i \, Un_i \, Pa_i - \sum_{i=1}^{NTB} Cpb_i \, nx_i \, Pab_i$$

becomes

$$C_D = -\sum_{i=1}^{NTV} Pa_i \, Cp_i \left[\sum_{j=1}^{NTV} Bn_{ij} Cp_j + Bn_{im} \alpha \right]$$

$$-\sum_{i=1}^{NTB} nx_i \, Pab_i \left[\sum_{j=1}^{NTV} Bp_{ij} Cp_j + Bp_{im} \alpha \right]$$

or

$$C_D = -\sum_{i=1}^{NTV} \left\{ \sum_{j=1}^{NTV} Pa_i \, Bn_{ij} Cp_i Cp_j + Pa_i Bn_{im} Cp_i \alpha \right\}$$

$$-\sum_{j=1}^{NTV} \sum_{i=1}^{NTB} nx_i Pab_i Bp_{ij} Cp_j - \sum_{i=1}^{NTB} nx_i Pab_i Bp_{im} \alpha$$

or, written as a quadratic function

$$= -\sum_{i=1}^{NTV} \left\{ \sum_{j=1}^{NTV} Q_{ij} Cp_i Cp_j + Q_{im} Cp_i \alpha + Q_{im} Cp_i \right\} - Q_{mm} \alpha$$

where $n = m + 1 = NTV + 2$, and

$$Q_{ij} = Pa_i Bn_{ij}$$

$$Q_{im} = Pa_i Bn_{im}$$

$$Q_{im} = -\sum_{k=1}^{NTB} n_{x_k} Pab_k Bp_{ki}$$

$$Q_{nm} = -\sum_{k=1}^{NTB} n_{x_k} Pab_k Bp_{km}$$

Other constraints may be written as a linear function of the independent variables (Cp_j, α) in a similar manner. The optimization consists of minimizing the expression for Cd subject to the constraint equations. Since the expression for Cd is quadratic in the unknowns, the minimization may be performed using the method of Lagrange multipliers. The unknowns can then be used to solve for the Cp's and also the normal velocities on the aerodynamic surfaces. The normal velocities on the aerodynamic surfaces determine the twist and camber.

4.3.3 An Exact Second Order Optimization In Two Dimensions

In two-dimensional supersonic flow an exact 2nd order solution is available. This example will serve to demonstrate the necessity of including the thickness drag in optimizing drag due to lift, when second order pressures are considered.

$$Cp_u = \frac{2}{\beta}(w_t + w_c) + 2 k (w_t + w_c)^2$$

$$Cp_l = \frac{2}{\beta}(w_t - w_c) + 2 k (w_t - w_c)^2$$

where $\beta^2 = M_\infty^2 - 1$

and $k = k(M_\infty)$ where, $k(M) = \frac{1}{(1-M^2)} \left\{ 1 + \frac{\gamma+1}{4} \frac{M^4}{(1-M^2)} \right\}$

therefore

$$\Delta Cp = -\frac{4}{\beta}[w_c + 2 \beta k w_c w_t]$$

$$2 \overline{Cp} = \frac{4}{\beta}[w_t + \beta k (w_t^2 + w_c^2)]$$

and drag/area $= \frac{4}{\beta}[w_c + 2 \beta k w_c w_t] w_c$

$$+ \frac{4}{\beta}[w_t + \beta k (w_t^2 + w_c^2)] w_t$$

$$= \frac{4}{\beta}[(1 + 3 \beta k w_t) w_c^2 + (1 + \beta k w_t) w_t^2]$$

Therefore the thickness and camber interact to give additional drag terms from both

$$- \Delta Cp \, w_c \quad \text{and} \quad 2 \overline{Cp} \, w_t$$

With a fixed thickness distribution the drag may be minimized subject to a given lift. Ignoring the terms which depend on thickness only:

$$\text{minimize} \qquad C_D = \frac{4}{\beta}\int_0^1 (1 + 3 \beta k w_t) w_c^2 \, dx$$

$$\text{subject to} \qquad C_L = -\frac{4}{\beta}\int_0^1 (1 + 2 \beta k w_t) w_c \, dx$$

The solution may be obtained using a variational approach.

$$\text{let} \qquad w_c(x) = W(x,\lambda) + \delta\eta(x)$$

where $\delta\eta(x)$ is an arbitrary function which is allowed to vary, and λ is a constant which can be adjusted to satisfy the C_L constraint. If $W(x,\lambda)$ is the function which gives the minimum drag, subject to the C_L constraint, then the addition of any function $\delta\eta(x)$ will increase the drag. Therefore:

$$\frac{\partial}{\partial\delta} (C_D - \lambda C_L) = 0 \qquad \text{at} \quad \delta = 0$$

and since $$\frac{\partial}{\partial\delta} w_c(x) = \eta(x)$$

$$\int_0^1 [2 (1 + 3 \beta k w_t) W + \lambda(1 + 2 \beta k w_t)] \eta(x) \, dx = 0$$

Since this relation holds for all functions $\eta(x)$, we must have:

$$W(x,\lambda) = -\frac{\lambda}{2} \frac{[1 + 2\beta k w_t(x)]}{[1 + 3\beta k w_t(x)]}$$

but since $$C_L = \frac{4}{\beta}\frac{\lambda}{2}\int_0^1 \frac{[1 + 2\beta k w_t(\xi)]^2}{[1 + 3\beta k w_t(\xi)]} \, d\xi$$

or $$\frac{\lambda}{2} = \frac{C_L}{\frac{4}{\beta}\int_0^1 \frac{[1 + 2\beta k w_t(\xi)]^2}{[1 + 3\beta k w_t(\xi)]} \, d\xi}$$

$$\text{then} \quad w_c(x) = -\frac{\beta}{4} C_L \frac{\dfrac{[\,1 + 2\beta k\, w_t(x)\,]}{[\,1 + 3\beta k\, w_t(x)\,]}}{\displaystyle\int_0^1 \frac{[\,1 + 2\beta k\, w_t(\xi)\,]^2}{[\,1 + 3\beta k\, w_t(\xi)\,]}\, d\xi}$$

and therefore

$$C_{D\,opt} = \frac{\beta}{4} C_L^2 \frac{1}{\displaystyle\int_0^1 \frac{[\,1 + 2\beta k\, w_t(\xi)\,]^2}{[\,1 + 3\beta k\, w_t(\xi)\,]}\, d\xi}$$

The drag value is slightly lower than the result using a first order analysis. The first order result is obtained by setting $k = 0$.

$$\frac{C_{D\,opt}}{C_L^2} = \frac{\beta}{4}$$

The second order drag may be evaluated for any specific thickness distribution. As an example, a biconvex thickness distribution can be used.

$$z_t(x) = 2\tau x(1 - x) \qquad w_t(x) = 2\tau(1 - 2x)$$

First consider the following:

$$\frac{(1 + 2a)^2}{(1 + 3a)} = \frac{2^2}{3^2}\frac{(\frac{3}{2} + 3a)^2}{(1 + 3a)} = \frac{2^2}{3^2}\frac{[\frac{1}{2} + (1 + 3a)]^2}{(1 + 3a)}$$

$$= \frac{2^2}{3^2}\left\{\frac{1}{2^2(1 + 3a)} + 1 + (1 + 3a)\right\}$$

Now let $a(x) = \beta\, k\, w_{\ell}(x) = 2\,\beta k \tau\,(1 - 2x)$

$$= \frac{1}{3} e\,(1 - 2x) \qquad \text{where} \quad e = 6\,\beta\, k\, \tau$$

Then let

$$f = \int_0^1 \frac{dx}{(1 + 3a)} = \int_0^1 \frac{dx}{[1 + e(1 - 2x)]}$$

$$= \frac{1}{e}\,\frac{1}{2} \log [1+e(1-2x)]\Big|_1^0 = \frac{1}{e}\,\frac{1}{2} \log \frac{(1+e)}{(1-e)}$$

Therefore:

$$\int_0^1 \frac{[1 + 2\beta\, k\, w_{\ell}(x)]^2}{[1 + 3\beta\, k\, w_{\ell}(x)]}\, dx = \int_0^1 \frac{[1 + 2\,a(x)]^2}{[1 + 3\,a(x)]}\, dx$$

$$= \frac{1}{9} \int_0^1 \left\{ \frac{1}{(1 + 3a)} + 8 + 12a \right\} dx$$

$$= \frac{1}{9} \int_0^1 \left\{ \frac{1}{(1 + 3a)} + 8 + 4e(1 - 2x) \right\} dx$$

$$= \frac{1}{9} (f + 8)$$

and $$C_{D_{OPT}} = \frac{\beta}{4} C_L^2 \frac{9}{(f + 8)}$$

Since $\lim_{e \to 0} f = 1$ this result reduces to the first order result as $e \to 0$

If we set $w_c(x) = c$ (the first order result), we get

$$C_D = \frac{4}{\beta} \int_0^1 [1 + 3 \beta k w_t(x)] c^2 \, dx$$

$$C_L = -\frac{4}{\beta} \int_0^1 [1 + 2 \beta k w_t(x)] c \, dx$$

and whenever the thickness distribution integrates to zero.

$$\frac{C_{D_{FLAT}}}{C_L^2} = \frac{4}{4} \frac{\int_0^1 [1 + 3 \beta k w_t(x)] \, dx}{\left\{ \int_0^1 [1 + 2 \beta k w_t(x)] \, dx \right\}^2} = \frac{\beta}{4}$$

The ratio of the optimum camber distribution drag to the uncambered airfoil drag at the same value of C_L is:

$$\frac{C_{D_{OPT}}}{C_{D_{FLAT}}} = \frac{9}{(f + 8)}$$

The angle of attack of the optimum camber airfoil also differs from first order result, since there is some lift due to the camber. The angle of attack is the integral of $w_c(x)$ over the chord.

$$\alpha = \int_0^1 w_c(x) \, dx$$

therefore

$$\alpha_{opt} = \frac{\beta}{4} C_L \frac{\int_0^1 \frac{[\,1 + \frac{2}{3} e\,(1 - 2x)\,]}{[\,1 + e\,(1 - 2x)\,]}\,dx}{\frac{1}{9}(f + 8)} = 3\,\frac{(f + 2)}{(f + 8)}\,\frac{\beta}{4}\,C_L$$

The results for the biconvex airfoil will be presented and discussed in section 6.1.2.

4.3.4 Second Order Wing Optimization

Again the optimization problem consists of mimimizing the expression for drag while satisfying a set of constraints on C_L, center of pressure, etc, and again we will assume the thickness distribution to be given. However if second order pressures are considered, the influence of the lift on the thickness drag must be considered. This was demonstrated in the previous two dimensional example. Since in the calculation of second order Cp's, derivatives of camber geometry must be computed, the camber optimization is conducted by considering the camber to be composed of a sum of unit camber functions with smooth derivatives. The set of functions must be complete enough to describe any optimum. There would be a set of functions at each span station consisting of a local angle of attack (twist) and some additional functions which integrate to zero in the chordwise direction.

Let zv(x,j,k) be the camber z/c value, at x/c = x, for the k'th camber function, on span station j. An appropriate set of camber constraint functions might consist of the following functions for each span station j.

$$z/c = \int_0^x wv(x)\,dx = 0 \quad \text{for all k, at all span stations} \neq j$$

i.e. the camber constraint function at span station j contributes no camber at any other span station. On span station j:

$$z/c = zv(x,j,1) = -x$$

$$= zv(x,j,2) = x(1-x)$$

$$= zv(x,j,3) = x(1-x)(1-2x)$$

$$= zv(x,j,4) = x(1-x)(1-4x)(3-4x)$$

$$= zv(x,j,5) = x(1-x)(1-2x)(x-A)(x-B)$$

where

$$A = (2-\sqrt{2})/4$$
$$B = (2+\sqrt{2})/4$$

Therefore the camber and camber normal velocities for each panel may be written as the matrix product of a constraint matrix (Z_{ik} for the displacements, zv, and C_{ik} for the normal velocities, wv), and a vector of the unknown coefficients, x_k, of each camber constraint. If N is the total number of constraint functions:

$$zv_i = \sum_{k=1}^{N} Z_{ik} x_k \qquad i = 1, NTV$$

$$wv_i = \sum_{k=1}^{N} C_{ik} x_k \qquad i = 1, NTV$$

A set of unit solutions for the first order Cp's result from the camber constraint functions. This means the first order Cp's may be written as a linear sum in terms of the unknowns x_k. If P_{ik} represents the first order ΔCp at panel i due to camber constraint function k, then we can write:

$$\Delta Cp_i = \sum_{k=1}^{N} P^{(1)}_{ik} x_k \qquad i = 1, NTV$$

The second order Cp's may be written in terms of the first order solution.

If we let $Z(x,y) = Zv + Zt = \Psi(x,y) - \alpha_o(x-x)$

$$Cp^{(2)} = -2\,k(M)\left[\tfrac{1}{2}(1-M_\infty^2)\phi_x^2 + \tfrac{1}{2}\phi_y^2 + \tfrac{1}{2}(\phi_z + a_\infty)^2 - \tfrac{1}{2}a_\infty^2 + Z\,\phi_{xz} + \varphi_x\right]$$

with the second order boundary condition on φ

$$\varphi_z = (1-M_\infty^2)\,\phi_x Z_x + \phi_y Z_y + Z\left[(1-M_\infty^2)\,\phi_{xx} + \phi_{yy}\right]$$

where $\Box^2 \varphi = 0$

The second order Cp's may be broken into components with odd and even symmetry about the z = 0 plane of each panel.

$$\phi_x = u(\text{vortex-even}) + u(\text{thickness}) \pm u(\text{vortex-odd})$$

$$\phi_y = v(\text{vortex-even}) + v(\text{thickness}) \pm v(\text{vortex-odd})$$

$$\phi_z = w(\text{vortex-even}) + w(\text{thickness-even}) \pm w(\text{thickness})$$

The planar case is easier and will be considered first. In this case

$$u(\text{vortex-even}) = v(\text{vortex-even}) = w(\text{thickness-even}) = 0$$

and

$$\phi_x = ut \pm uv$$

$$\phi_y = vt \pm vv$$

$$\phi_z = wv \pm wt$$

where the v and t components are entirely due to vortex and thickness panel perturbations respectively. The additional terms are usually small and can be added when the nonplanar case is considered.

Planar Case

For the case of configurations confined to a single plane the first order thickness and vortex solutions are decoupled. The solutions may be performed independently and the perturbation velocities have either an odd or even symmetry. It will be shown that the planar case allows a direct solution for the camber coefficients x_k, even when second order Cp's are used. The nonplanar case will require an iterative solution. Written in terms of the first order vortex and thickness velocities at each panel:

$$\Delta Cp^{(2)} = -2\,k(M)\,[\;\beta^2 uv\,ut + vv\,vt + (wv + a_\infty)\,wt + wv_x\,Zt + wt_x\,Zv + \varphi_x^{ODD}\;]$$

$$\overline{Cp}^{(2)} = -2\,k(M)\,[\tfrac{1}{2}\beta^2(uv^2 + ut^2) + \tfrac{1}{2}(vv^2 + vt^2) + \tfrac{1}{2}(wv^2 - a_\infty^2) + \tfrac{1}{2}wt^2 + wv_x\,Zv + wt_x\,Zt + \varphi_x^{EVEN}\;]$$

Where φ satisfies $\Box^2\varphi = 0$, and the second order boundary condition on φ is given by:

$$\varphi_z^{ODD} = \beta^2(\,uv\,wt + ut\,wv\,) + vv\,\frac{\partial}{\partial y}Zt + vt\,\frac{\partial}{\partial y}Zv + Zt\,(\beta^2\frac{\partial}{\partial x}uv + \frac{\partial}{\partial y}vv\;) + Zv\,(\beta^2\frac{\partial}{\partial x}ut + \frac{\partial}{\partial y}vt\;)$$

$$\varphi_z^{EVEN} = \beta^2(\,uv\,wv + ut\,wt\,) + vv\,\frac{\partial}{\partial y}Zv + vt\,\frac{\partial}{\partial y}Zt + Zv\,(\beta^2\frac{\partial}{\partial x}uv + \frac{\partial}{\partial y}vv\;) + Zt\,(\beta^2\frac{\partial}{\partial x}ut + \frac{\partial}{\partial y}vt\;)$$

Using a coordinate transformation at each panel:

$\xi = x - Ty$ where T is the tangent of the panel sweep angle

$\eta = y$

we can write y derivatives in term of x derivatives and derivatives along lines of constant percent chord, $\frac{\partial}{\partial\eta}$ (ξ = const)

$$\frac{\partial}{\partial x} = \frac{\partial}{\partial\xi} \qquad \frac{\partial}{\partial y} = \frac{\partial}{\partial\eta} - T\,\frac{\partial}{\partial\xi}$$

Therefore we can write:

$$\varphi_{\bar{x}}^{odd} = \beta^2 (uv\, wt + ut\, wv) + vv(\frac{\partial}{\partial \eta} Zt - T\, wt) + vt(\frac{\partial}{\partial \eta} Zv - T\, wv)$$
$$+ Zt\, (\beta^2 \frac{\partial}{\partial x} uv + \frac{\partial}{\partial \eta} vv - T \frac{\partial}{\partial x} vv) + Zv\, (\beta^2 \frac{\partial}{\partial x} ut + \frac{\partial}{\partial \eta} vt - T \frac{\partial}{\partial x} vt)$$

$$\varphi_{\bar{x}}^{even} = \beta^2 (uv\, wv + ut\, wt) + vv(\frac{\partial}{\partial \eta} Zv - T\, wv) + vt(\frac{\partial}{\partial \eta} Zt - T\, wt)$$
$$+ Zv\, (\beta^2 \frac{\partial}{\partial x} uv + \frac{\partial}{\partial \eta} vv - T \frac{\partial}{\partial x} vv) + Zt\, (\beta^2 \frac{\partial}{\partial x} ut + \frac{\partial}{\partial \eta} vt - T \frac{\partial}{\partial x} vt)$$

The vortex solution velocities can be expressed in terms of the unit camber solutions. Since the thickness solution is given, the second order ΔCp's can be expressed as a linear combination of the unknown camber coefficients x_k.

$$\Delta Cp_i^{(2)} = \sum_{k=1}^{N} P_{ik}^{(2)} x_k \qquad i = 1, NTV$$

The second order even Cp solution can be expressed as a quadratic function of the unknowns x .

$$\overline{Cp}_i^{(2)} = \sum_{k=1}^{N} \sum_{\ell=1}^{N} \overline{P}_{ik\ell}^{(2)} x_k x_\ell \qquad i = 1, NTV$$

Therefore the drag coefficient may be written:

$$C_D = -\sum_{i=1}^{NTV}\sum_{k=1}^{N}\sum_{l=1}^{N}\left(P^{(1)}_{ik} + P^{(2)}_{il}\right) S_i C_{il}\, x_k x_l$$

$$-\sum_{i=1}^{NTV}\sum_{k=1}^{N}\sum_{l=1}^{N} 2\left(\bar{P}^{(1)}_{i} + \bar{P}^{(2)}_{ikl}\right) S_i wt_i\, x_k x_l$$

$$= \sum_{k=1}^{N}\sum_{l=1}^{N} Q_{kl}\, x_k x_l$$

By using the method of Lagrange multipliers, this quadratic form may be minimized in conjunction with the constraint functions which can be expressed as a linear combination of the unknown camber coefficients x_k.

5. FULL POTENTIAL ANALYSIS

The full potential equation either in conservative form or nonconservative form is frequently used for the treatment of transonic flow fields, where the local Mach number in general does not exceed ~1.4. However, if the assumptions of irrotationality and isentropicity are reasonably valid, then the full potential equation is expected to yield results comparable to Euler equations, even for supersonic/hypersonic flow fields. For preliminiary design studies, where quick turnaround is desired, the full potential methods can be an attractive substitute for expensive Euler methods and less accurate linear theory methods.

A nonlinear aerodynamic prediction technique based on the full potential equation in conservation form has been developed, during this contractual effort, for the treatment of supersonic flows. A detailed description of the method is already presented in two published papers, which are enclosed in the Appendix section for convenience. Reference 4 describes the method from the concept of positive artificial viscosity and diagonal dominance. Reference 5 presents the method in a more elegant way, in terms of the theory of characteristic signal propagation. Since the Appendix section clearly describes the full potential method, only the add-on material (not included in the published articles) will be presented in this section.

5.1 GRID GENERATION

Special procedures are necessary to generate a grid system around sharp leading edges of wings. A typical cross-sectional view of such a sharp leading edged wing-body is shown in Figure 5.1. If one generates a grid system without any special treatment, most likely the grid solver routine will fail to converge near the sharp leading edge. Even if convergence is achieved, the resulting grid will not have a smooth distribution due to collapsing grid cells near the leading edge. To avoid this, the code in its present form uses the following procedure. Referring to Figure 5.1, a user prescribed boundary (line A-B) is chosen such that it divides the whole domain of computation into a lower domain and an upper domain. Along the curve A-B, the user also prescribes the desired grid point distribution. Then, the grid generation routine is used to separately generate the grid in the upper and lower domain. By maintaining a reasonable mesh near the leading edge, the user can avoid nearly vanishing Jacobians arising due to collapsing grid cells. Figure 5.2 shows an example grid generated for a sharp leading edge wing-body configuration.

Another modification to the grid generation part of the code is the option of prescribing the geometry in the crossflow plane (constant ζ plane) at discrete points as shown in Figure 5.3. Then a cubic spline routine is used to distribute the grid points along the discretely prescribed geometry surface. Figure 5.4 shows the grid pattern generated around a typical wing-body cross-section whose shape was discretely prescribed. Use of this option in the code allows the user to input any arbitrarily shaped wing-body geometry.

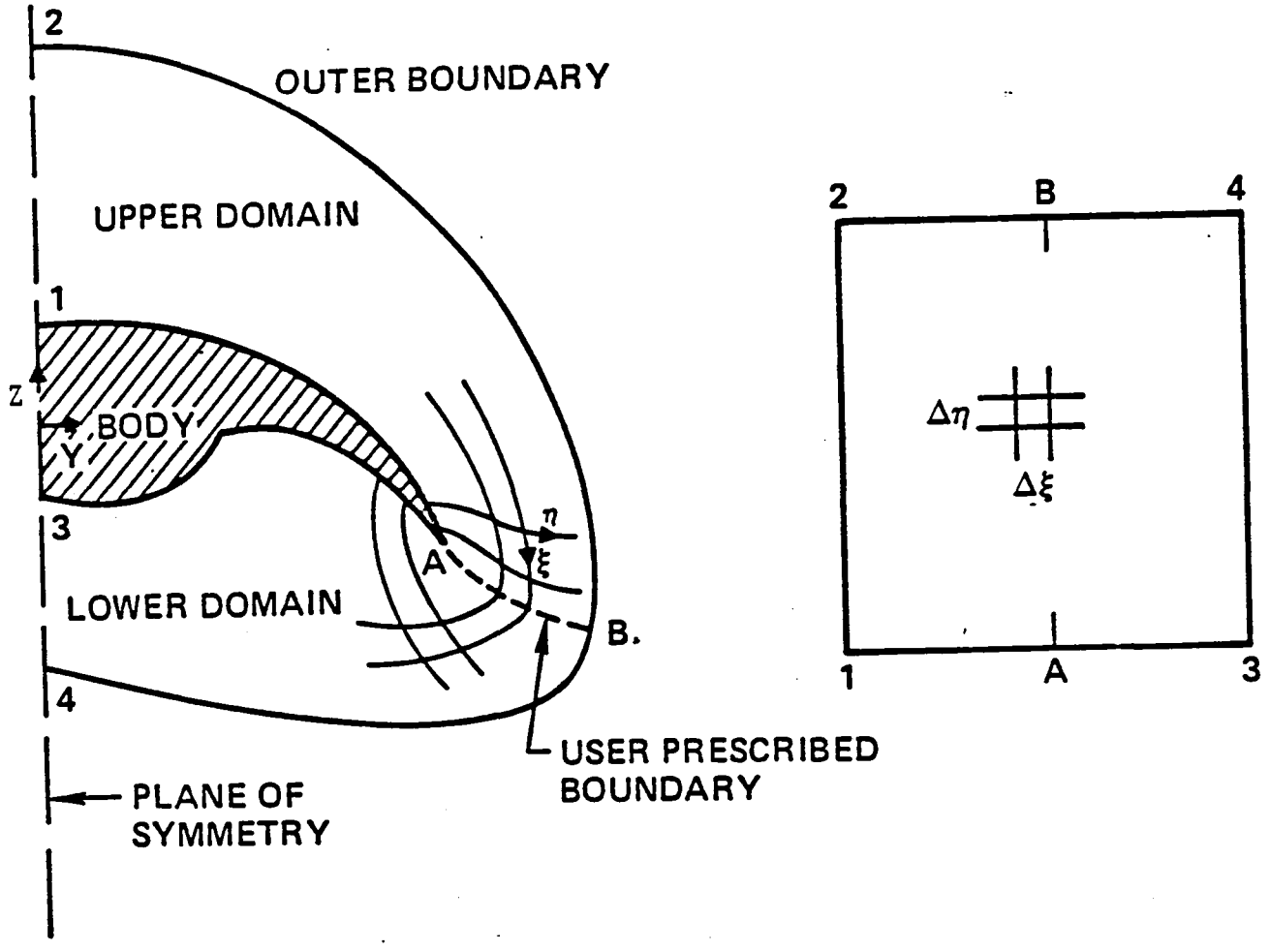

Figure 5.1. Double Domain Grid Generation Procedure

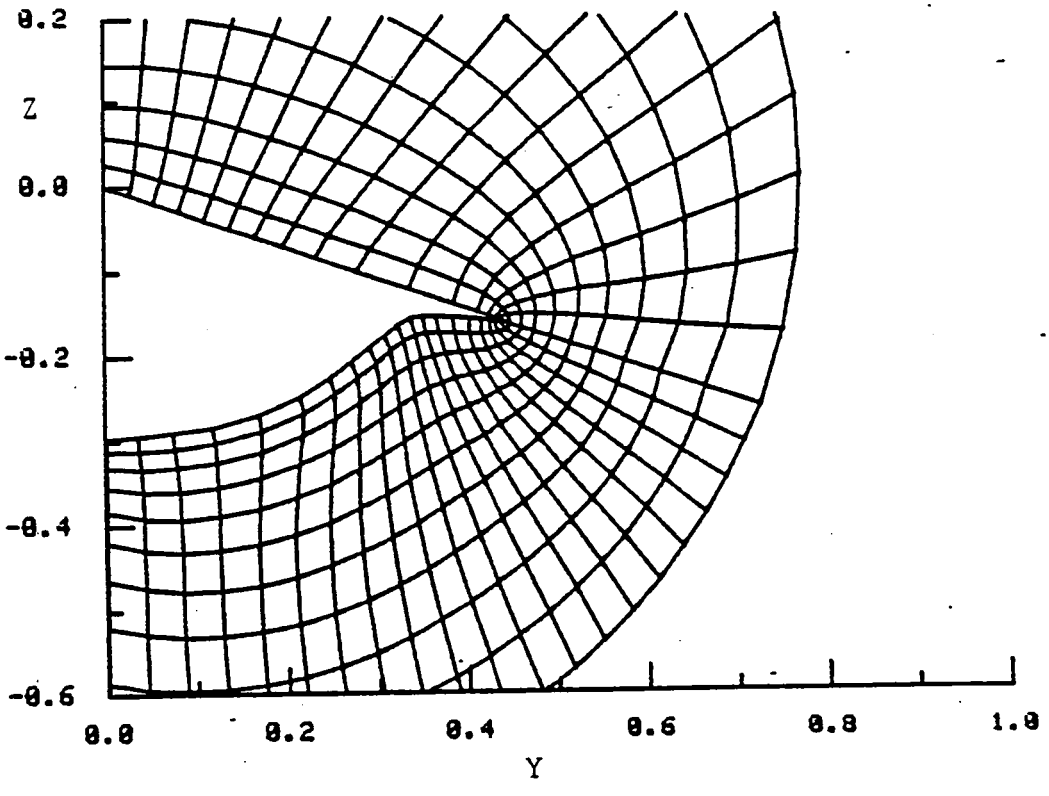

Figure 5.2. Grid Generation for a Sharp Leading Edge Wing-Body Configuration

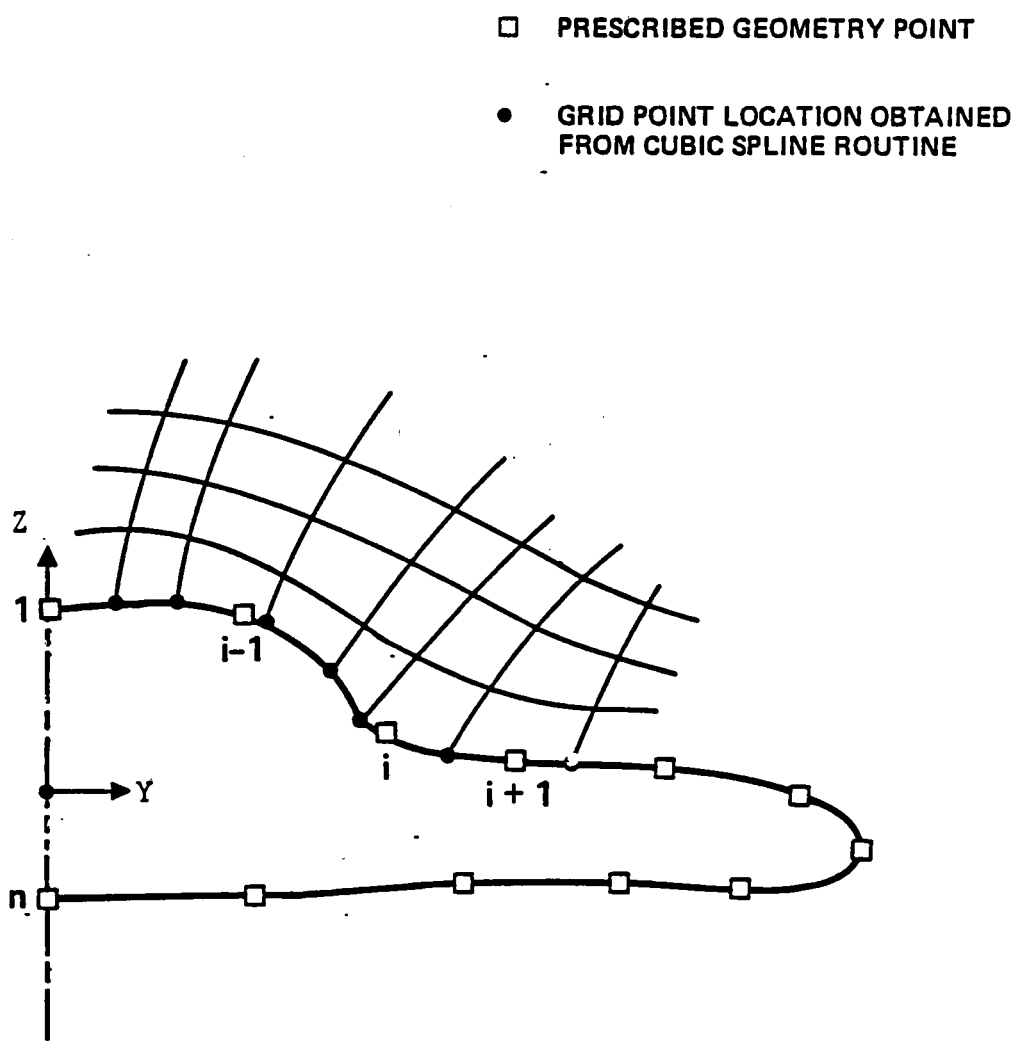

Figure 5.3. Discrete Geometry Input Option

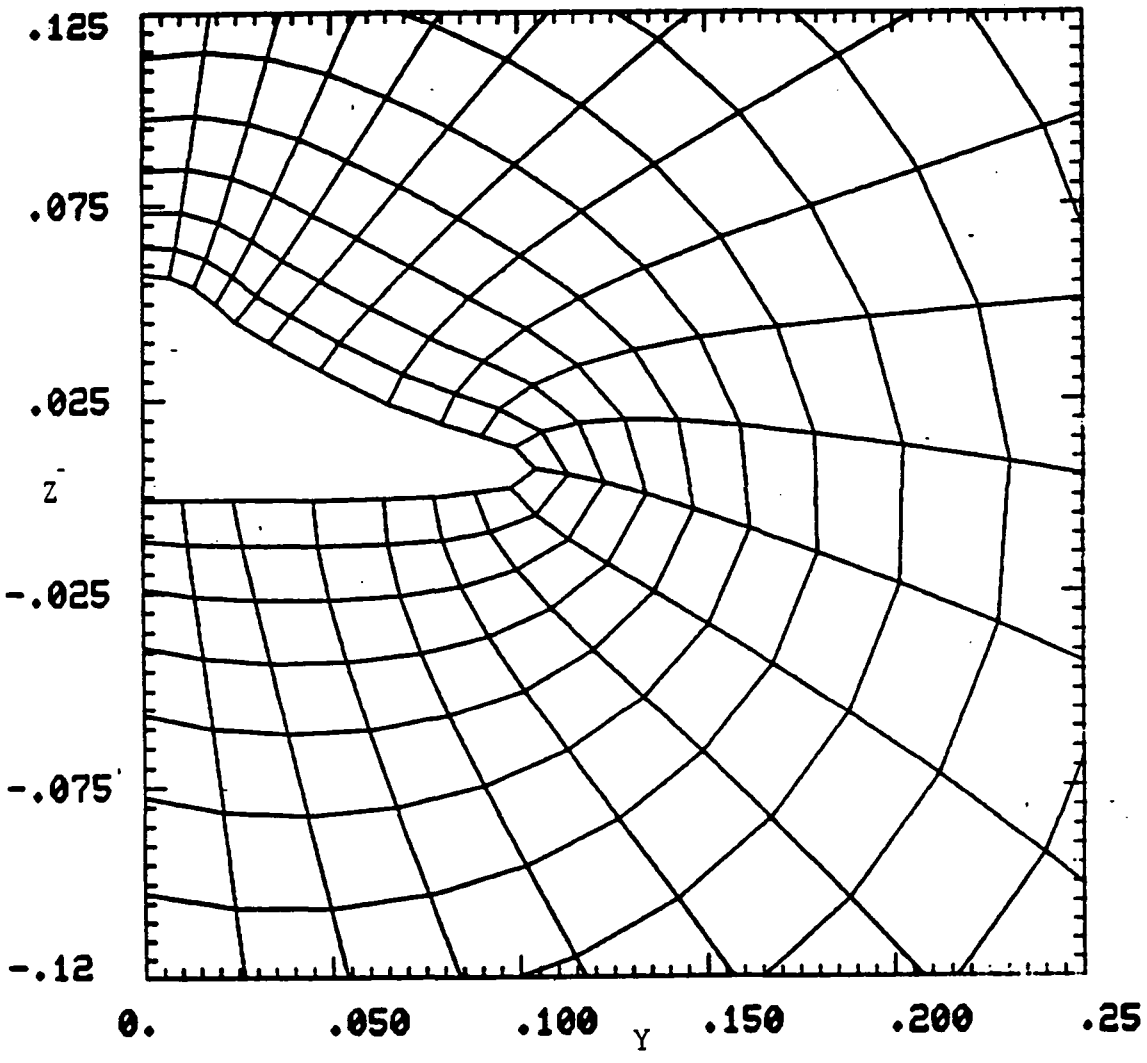

Figure 5.4. Grid Generation From Discrete Geometry Input Option

Another attractive option in the code is the ability to go from a crude (m x n) grid to a fine (p x q) grid calculation using appropriate interpolation routines that transfer the solution from (m x n) to (p x q) grid system. This capability is essential to handle wing-body combinations of the type shown in Figure 5.5. The calculation will proceed from the nose of the body to the plane where the wing originates from the fuselage using a (m x n) cruide grid distribution. Before starting the calculation over the wing the solution from this grid will be interpolated onto a (p x q) grid with clustering of points near the wing surface as shown in Figure 5.5. In this way, the shock that originates at the wing leading edge can be adequately resolved.

5.2 CROSSFLOW SWITCH

The code in its present form implements a robust density biasing scheme that is more continuously activated across the crossflow sonic line, than the previous method reported in Reference 5 (see Appendix section). The density biasing as reported in equations (15) and (16) of the above mentioned AIAA Paper, uses a multiplier $\nu = \mu\ (1 - a^2/q^2)$, with $\mu = 0$ for elliptic crossflow and $\mu = 1$ for hyperbolic crossflow. Thus, across the crossflow sonic line, the quantity ν has a discontinuous behavior since the total velocity q is always assumed to be greater than the speed of sound, a. This discontinuous behavior of the density biasing creates spurious oscillations near the shock wave as shown in the pressure contour plot of Figure 5.6 for cone at angle of attack. To avoid this oscillation, the current version of the density biasing uses the following:

$$\nu = \mu \left(1 - \frac{a_{22} a^2}{V^2} \right)$$

with

$$\mu = 0 \text{ when } a_{22} - \frac{V^2}{a^2} > 0$$

$$= 1 \text{ when } a_{22} - \frac{V^2}{a^2} < 0$$

Since the quantity $a_{22} - \frac{V^2}{a^2}$ goes to zero at the crossflow sonic line, the current version of the density biasing has a continuous behavior when it is turned on. The implementation of the new density biasing scheme produces a monotonic behavior across the shock wave, as shown by the pressure contour plot of Figure 5.7.

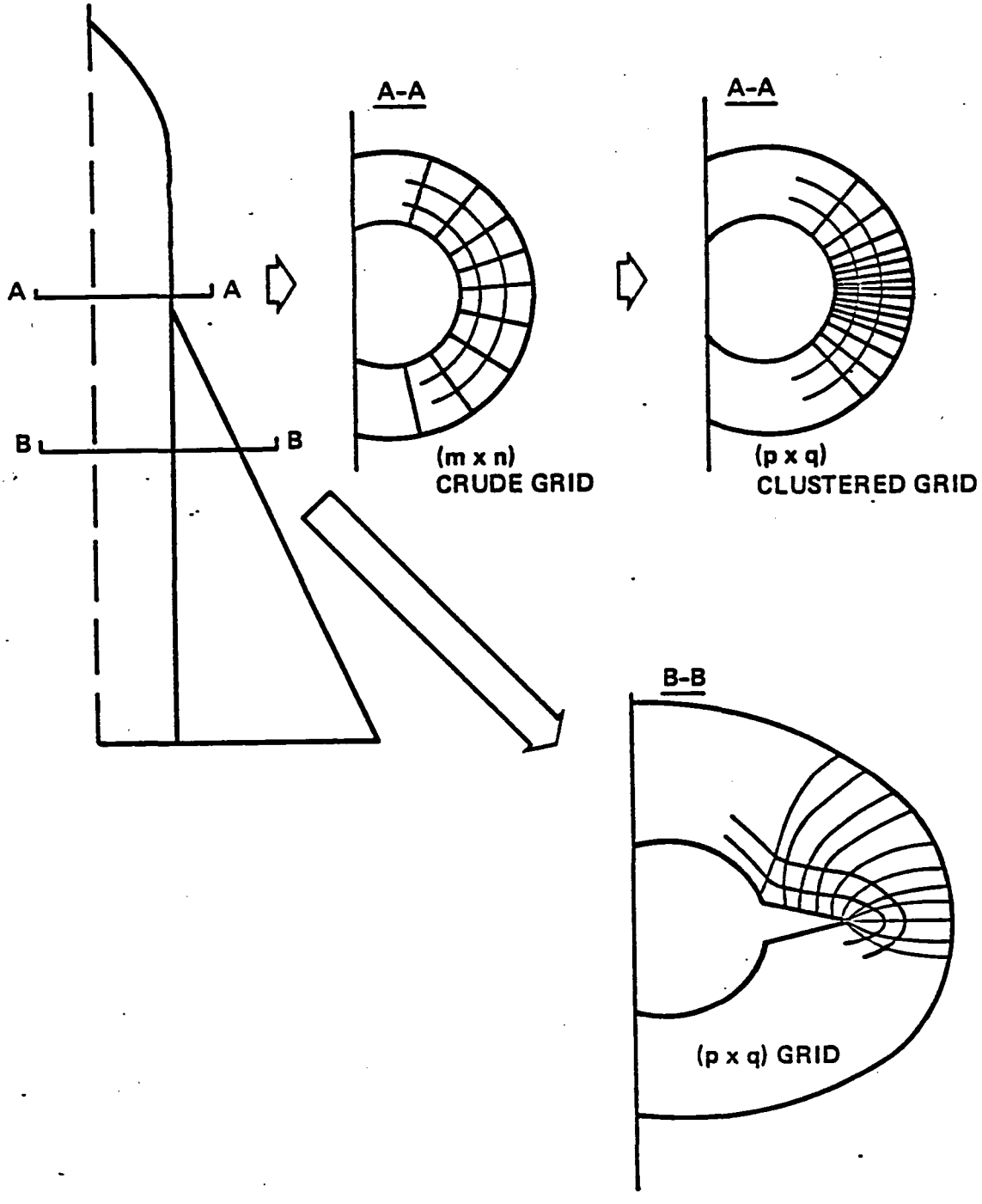

Figure 5.5. Proper Grid Arrangement for Wing-Body Combinations Using Interpolation Routines

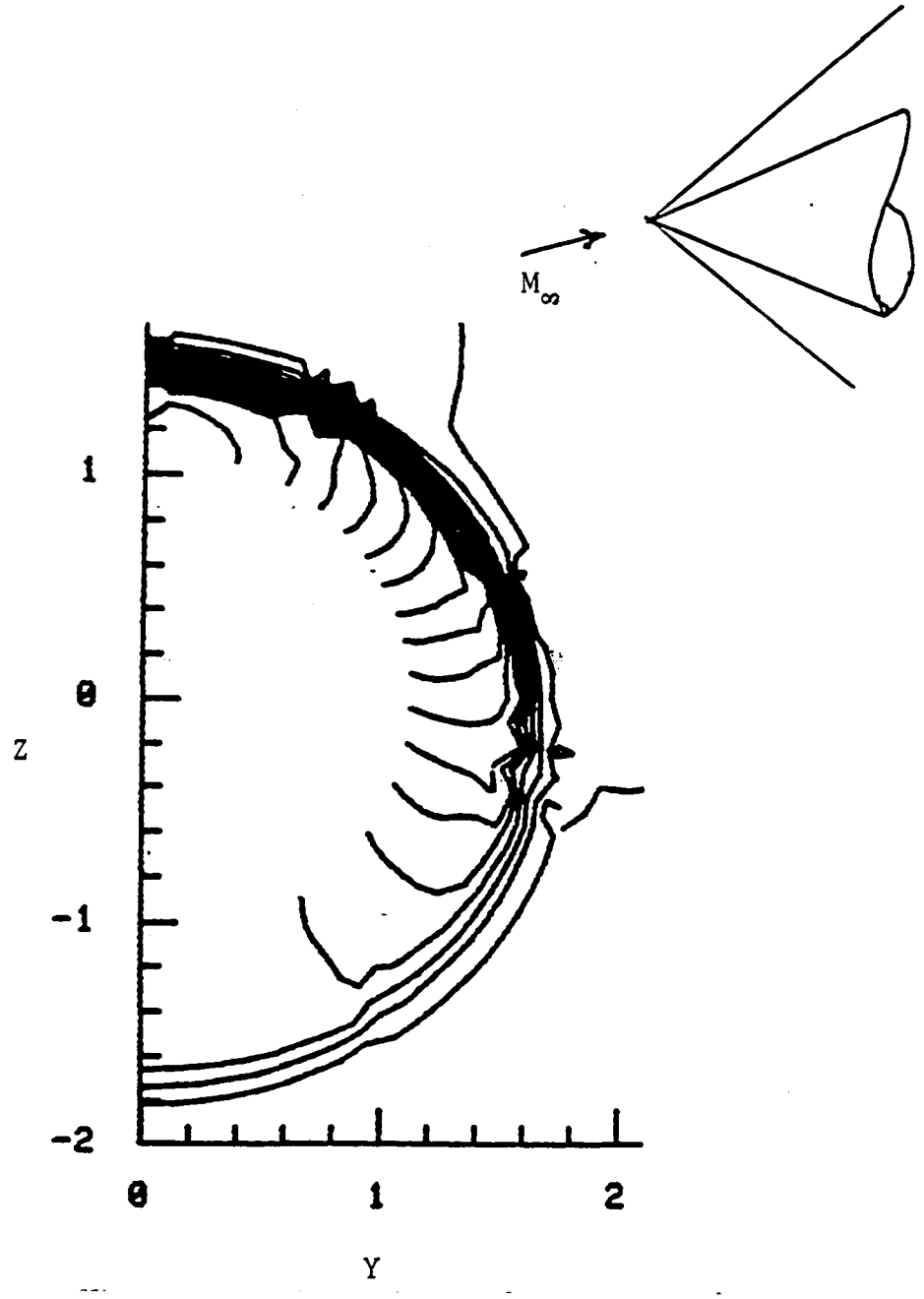

Figure 5.6. Crossplane Pressure Contours for a Cone at Angle of Attack M = 6, α =-4°. Old Density Biasing Switch Creating Oscillations near the Shock

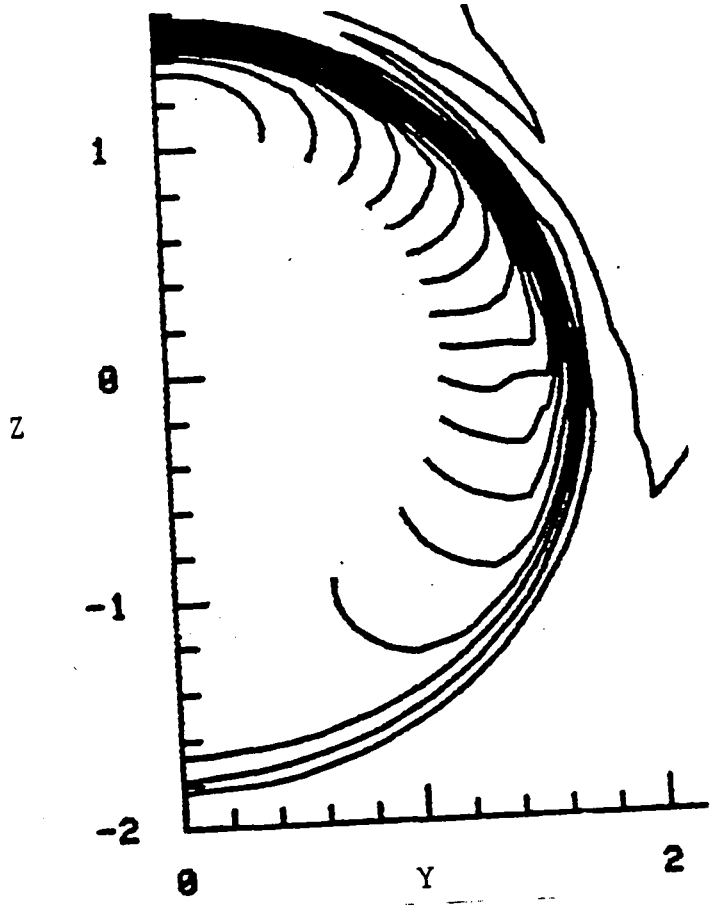

Figure 5.7. Crossplane Pressure Contours with the new Density Biasing Switch. Smoother Shock Profile. M = 6, α = -4°

6. RESULTS

6.1 SECOND ORDER

The wing-body small disturbance analysis[2] was extended in section 4.2 to consider multiple non planar lifting surface problems in order to model more realistic aircraft arrangements. The impact of a canard on the wing-body configuration of figure 3.2 will be presented in section 6.1.1 to illustrate this capability.

Nonlinear small disturbance optimization for a specified thickness was developed in section 4.3 to support advanced aerodynamic design studies. The analysis is sufficiently general to permit constraints on lift, trim, twist, and camber to be imposed. Minimum drag due to lift solutions for airfoil, wing, and wing-body model problems will be presented in sections 6.1.2 and 6.1.3. These results are the first supersonic non-linear potential optimum published to the knowledge of the contractor.

IBM 370 case time for the second order analysis of 30 CPU seconds for a typical aircraft arrangement and paneling density indicates the solution is responsive to preliminary design level of effort.

6.1.1 Multiple Surface Analysis

Prediction of the effect of a trapezoidal canard on the delta wing-body configuration of figure 3.2 was evaluated using first and second order analysis for the finite element model of figure 6.1.1. Wing chordwise net pressure distributions due to angle of attack at M = 6 are presented on figure 6.1.2 at four inboard span stations strongly influenced by the canard. The second order prediction for both the canard on and canard off cases exhibit a more forward chord loading which is consistent with measurements (e.g. figure 3.1) indicating a forward shift of the aerodynamic center location as the Mach number increases into the hypersonic range. The principal impact of the canard is to decrease the wing sectional loading inboard and increase it outboard of its tip location $\eta = .25$.

6.1.2 Two Dimensional Optimization

Minimum drag airfoil results were developed as a precursor effort to the three dimensional problem. An exact second order solution exists for this class of problems and is given by

$$C_p = \frac{2}{\beta}\left[\frac{\partial Z_t}{\partial x} \pm \frac{\partial Z_c}{\partial x}\right] + 2k\left[\frac{\partial Z_t}{\partial x} \pm \frac{\partial Z_c}{\partial x}\right]^2$$

where

$$\beta^2 = M_\infty^2 - 1 \qquad k = \frac{1}{\beta^2}\left[\frac{\gamma+1}{4}\frac{M_\infty^4}{\beta^2} - 1\right]$$

and +,- sign refer to the upper and lower surface respectively.

The resulting optima (see section 4.3.3) for specified thickness are

$$\frac{\partial z_c}{\partial x} = -\frac{\beta}{4} C_L \frac{g_1(x)}{g_2(x)} \left\{ \int_0^1 \frac{g_1^2(\bar{x})}{g_2(\bar{x})} d\bar{x} \right\}^{-1}$$

$$\frac{C_{D_{LIFT}}}{C_L^2} = \frac{\beta}{4} \left\{ \int_0^1 \frac{g_1^2(\bar{x})}{g_2(\bar{x})} d\bar{x} \right\}^{-1}$$

where $$g_i(x) = 1 + (i+1)\beta k \frac{dz_t}{dx}$$

These equations may be evaluated in closed form for an analytical thickness distribution. The solution for a biconvex airfoil $z_t = 2t\,x(1-x)$ is

$$\frac{\alpha_{OPT}}{C_L} = \frac{\beta}{4} \frac{3(f+2)}{(f+8)}$$

$$\frac{\partial z_c}{\partial x} = \frac{\beta}{4} C_L \frac{9}{(f+8)} \frac{\left[1 + \frac{2}{3}e(1-2x)\right]}{\left[1 + e(1-2x)\right]}$$

$$\frac{C_{D_{LIFT}}}{C_L^2} = \frac{\beta}{4} \frac{9}{(f+8)}$$

where $$e = 6\beta k t < 1$$

$$f = \frac{1}{2e} \ln \frac{1+e}{1-e}$$

The prediction for this case is presented on figure 6.1.3 as a function of the second order similarity parameter β k t which accounts for the nonlinear coupling between thickness and lift. First order (i.e. linear) levels are recovered in the limit $\epsilon \to 0$. Examination of the results indicate the optimum nonlinear drag levels become progressively lower than standard linear results as the Mach number or thickness or both increase. The reduction requires a small positive camber as indicated on the bottom of the figure. Nonlinear small disturbance compressibility also produces a more forward aerodynamic center location which is consistent with the three dimensional results of section 6.1.1 and figure 3.1.

6.1.3 Three Dimensional Optimization

First and second order trimmed optimum drag due to lift for the model problem of figure 6.1.4 is compared on figure 6.1.5 as a function of the longitudinal stability parameter dC_M/dC_L at M = 2 and a design $C_L = 0.1$. The abscissa scale may be alternately interpreted as the pitching moment at zero lift $C_{M_o} = -C_{L_D}\, dC_M/dC_L$. The second order nonlinear solution considers the coupling between thickness and lift for a five percent biconvex airfoil. Uncambered (i.e. flat plate) linear and nonlinear results are also presented to judge the potential benefit of optimization. Examination of figure 6.1.5 indicates a five percent improvement in lifting efficiency is achieved relative to the best linear optimum and occurs at approximately twice the longitudinal stability level ($dC_m/dC_L = -.072$ versus $-.14$). The three dimensional supersonic nonlinear optimum results are the first published to the knowledge of the contractor.

The first and second order optimum twist and camber for the minimum drag points of figure 6.1.5 are presented on figures 6.1.6 and 6.1.7 respectively. Both solutions have been constrained by the use of a linear combination of analytic functions to produce smooth deformation.

Second order analysis of the first order optimum and first order analysis of the second order optimum are also presented on figure 6.1.5 to establish the relative importance of the pressure and deformation differences between the linear and nonlinear solution. The former consideration is the more important of the two for the case under consideration. The results also provide insight into the test finding that linear designs typically exhibit maximum drag due to lift efficiency at a lift coefficient higher than the design condition. This is apparently due in part to the reduction in drag due to lift factor (for stable balance) resulting from nonlinear compressibility effects.

Optimization was also performed for a supersonic edge condition at M = 4.0. The results are presented as figure 6.1.8. The impact of twist and camber is small for both the first and second order computations. The former result is well known and has led to the use of planforms having a subsonic edge at cruise.

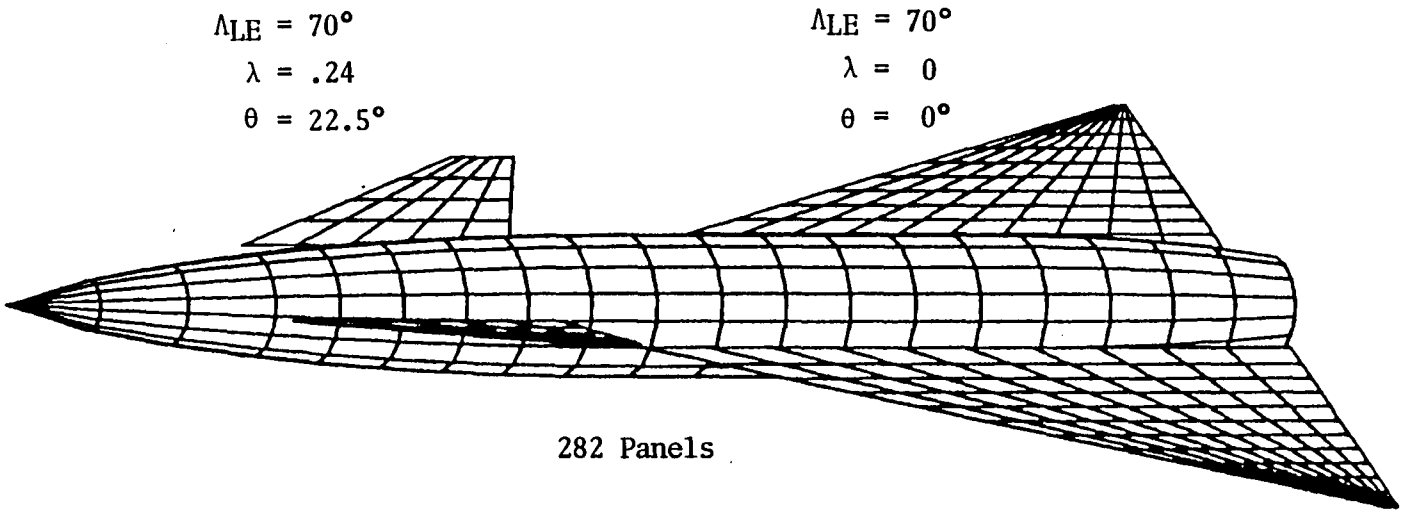

Figure 6.1.1. Wing-Body-Canard Finite Element Model

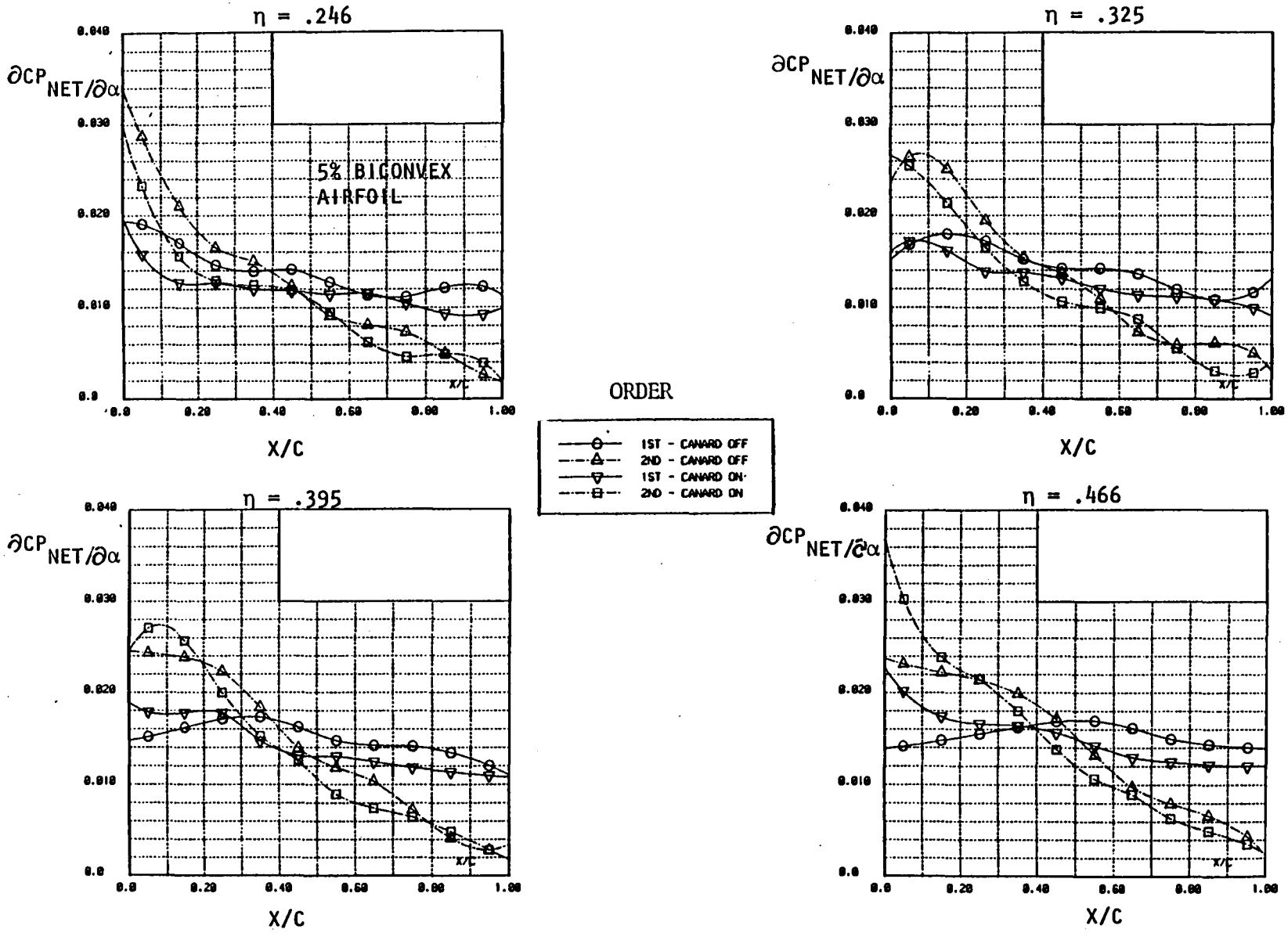

Figure 6.1.2. Effect of Canard on Wing Chord Load Due to Angle of Attack at M = 6

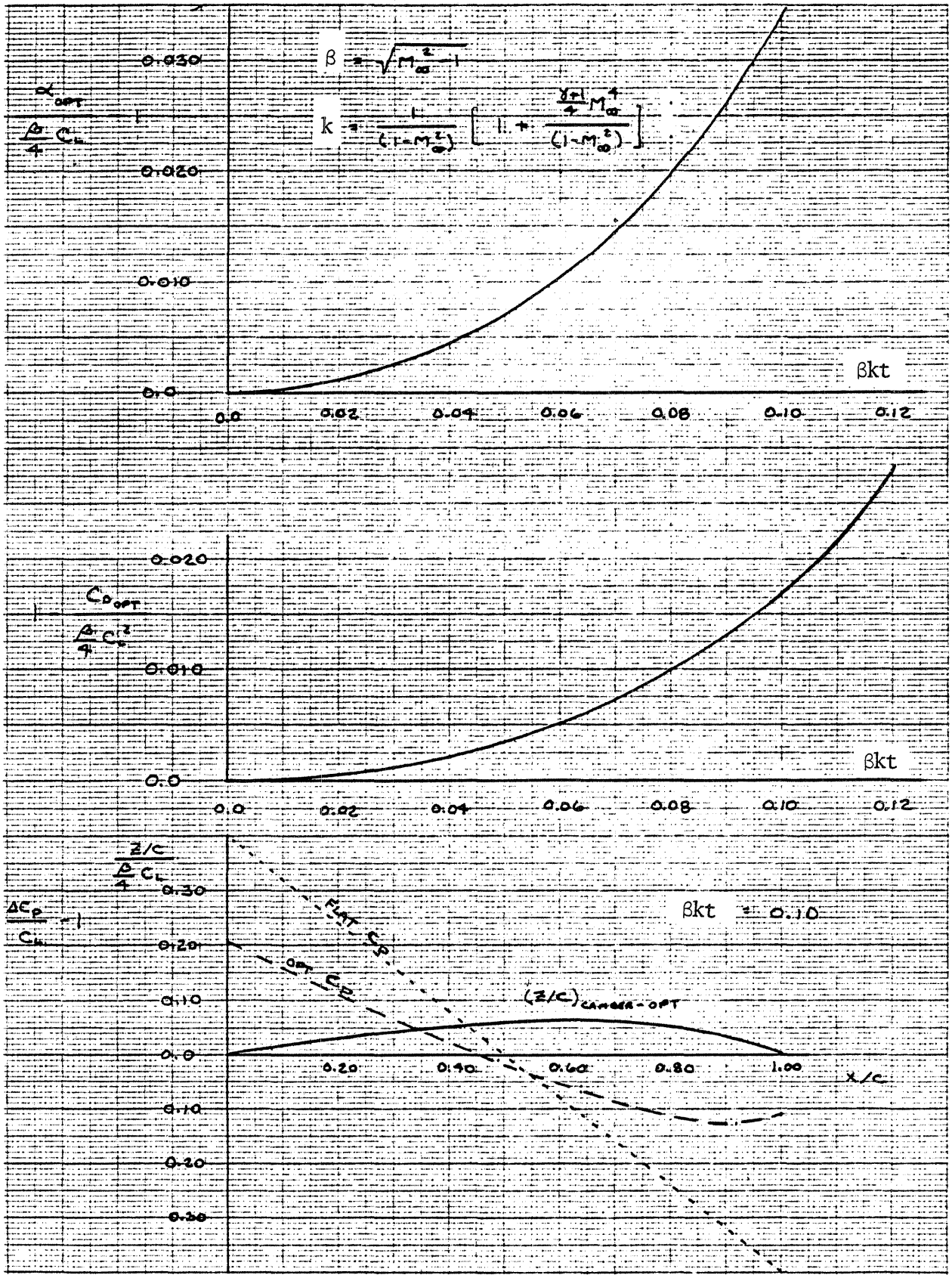

Figure 6.1.3. Second Order Optimum for a Biconvex Airfoil

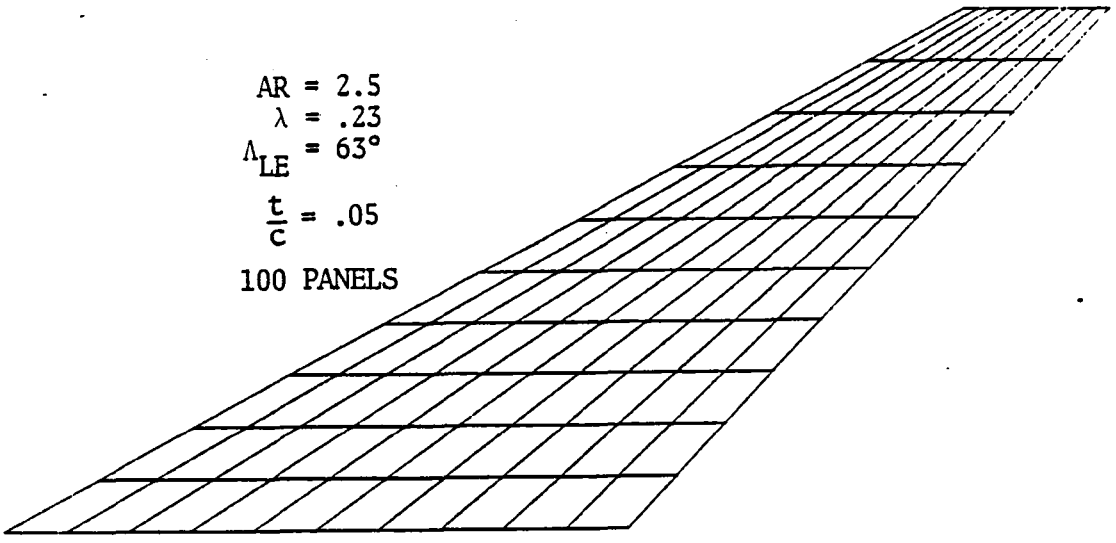

Figure 6.1.4. Three Dimensional Second Order Optimum Model Problem

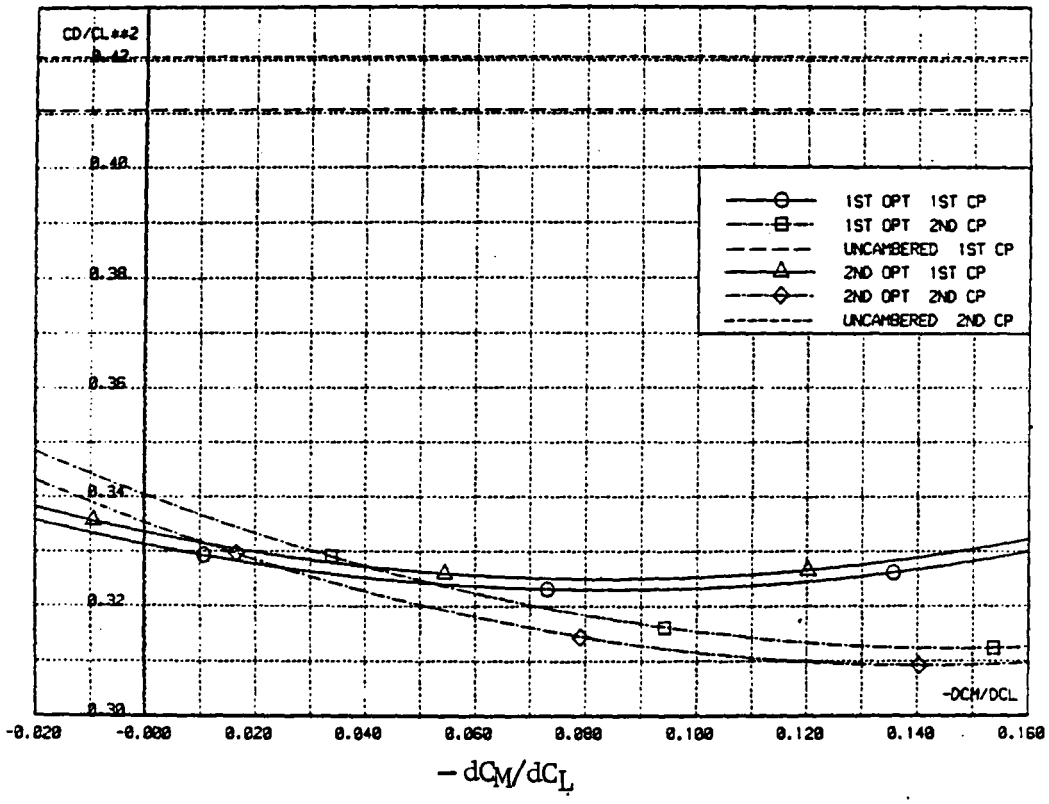

Figure 6.1.5. First and Second Order Optima for a Subsonic Edge Condition
$M = 2.0$, $C_L = 0.1$

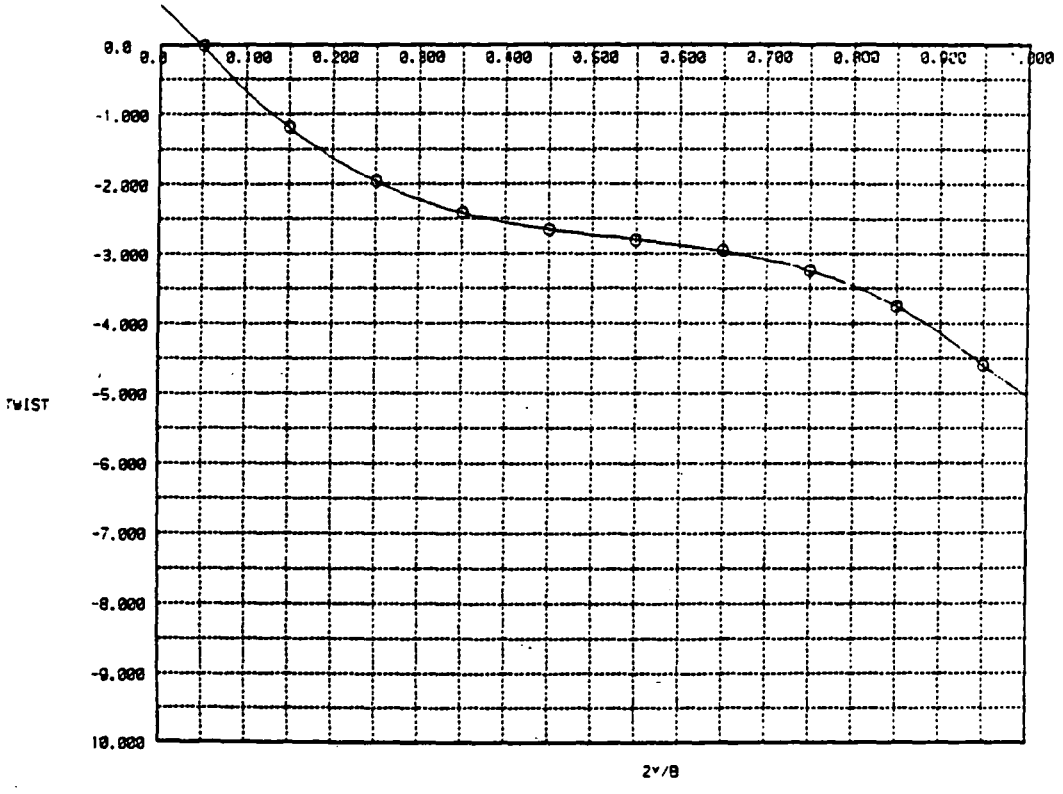

a) Twist

Figure 6.1.6. First Order Optimum Solution for dC_M/dC_L = -.072

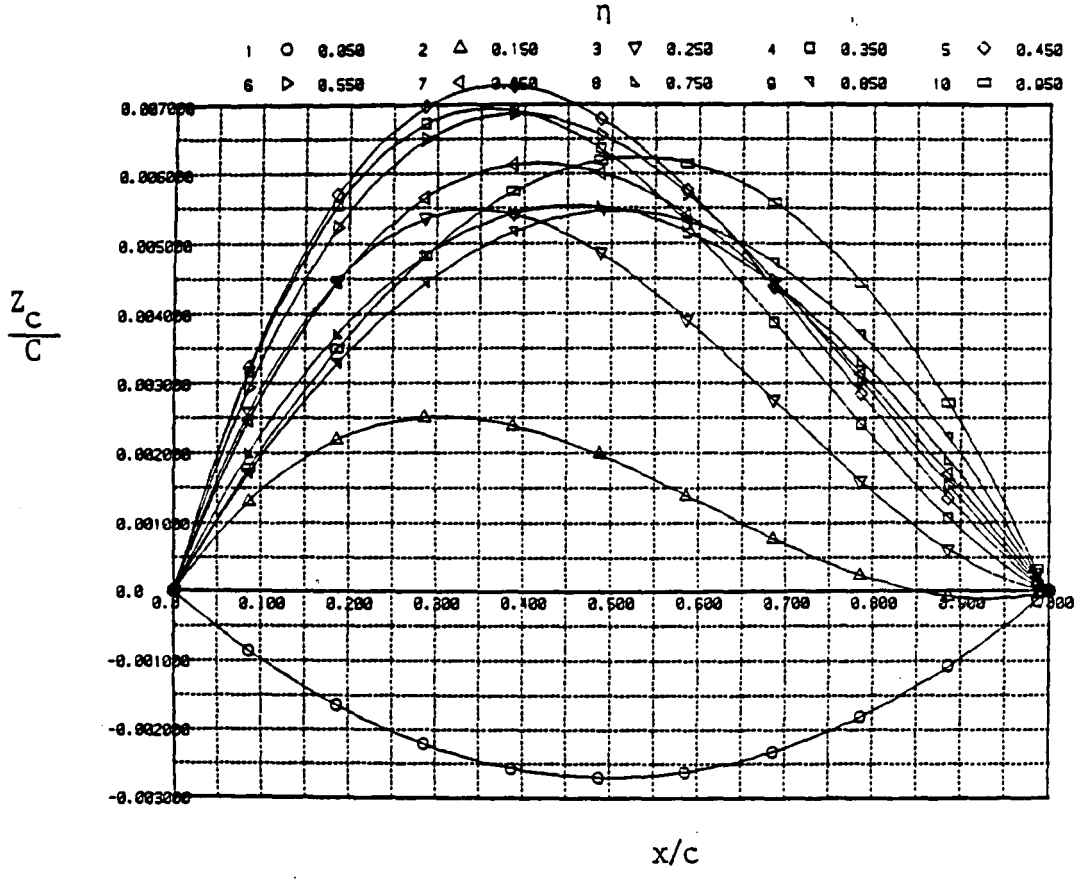

b) Camber

Figure 6.1.6. Completed

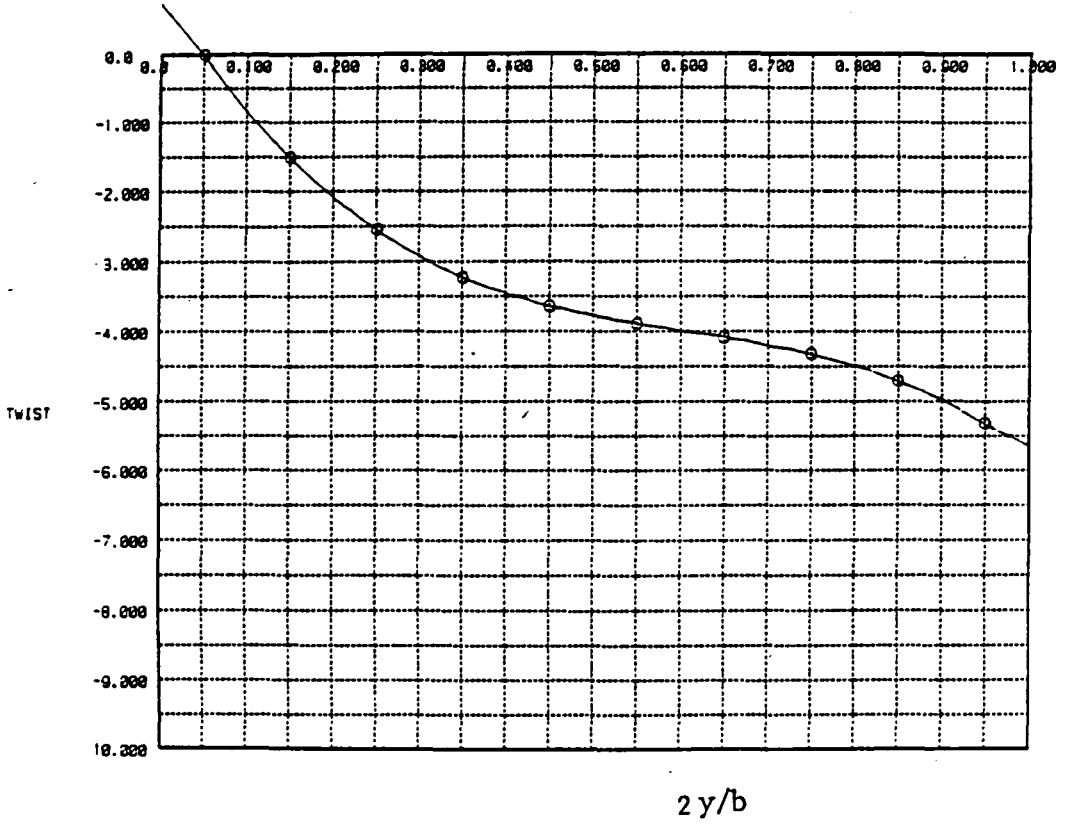

a) Twist

Figure 6.1.7. Second Order Optimum Solution for $dC_M/dC_L = -.14$

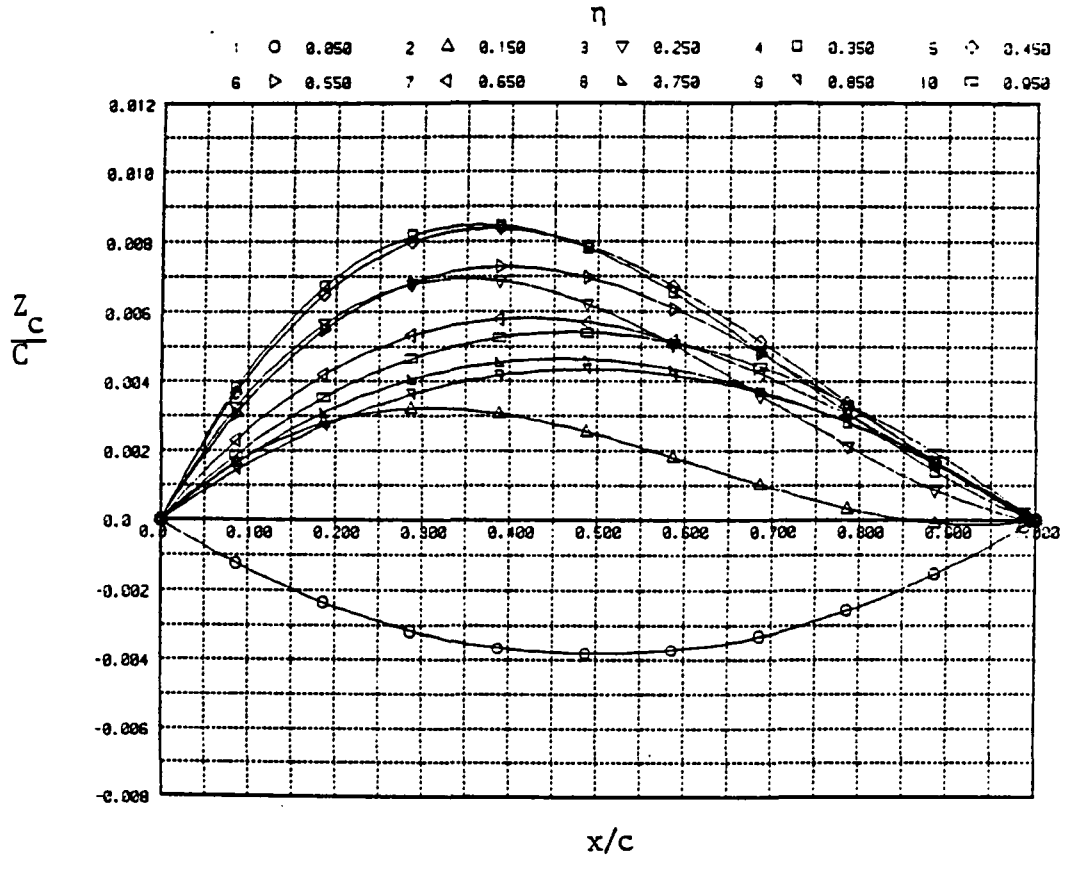

b. Camber

Figure 6.1.7. Completed

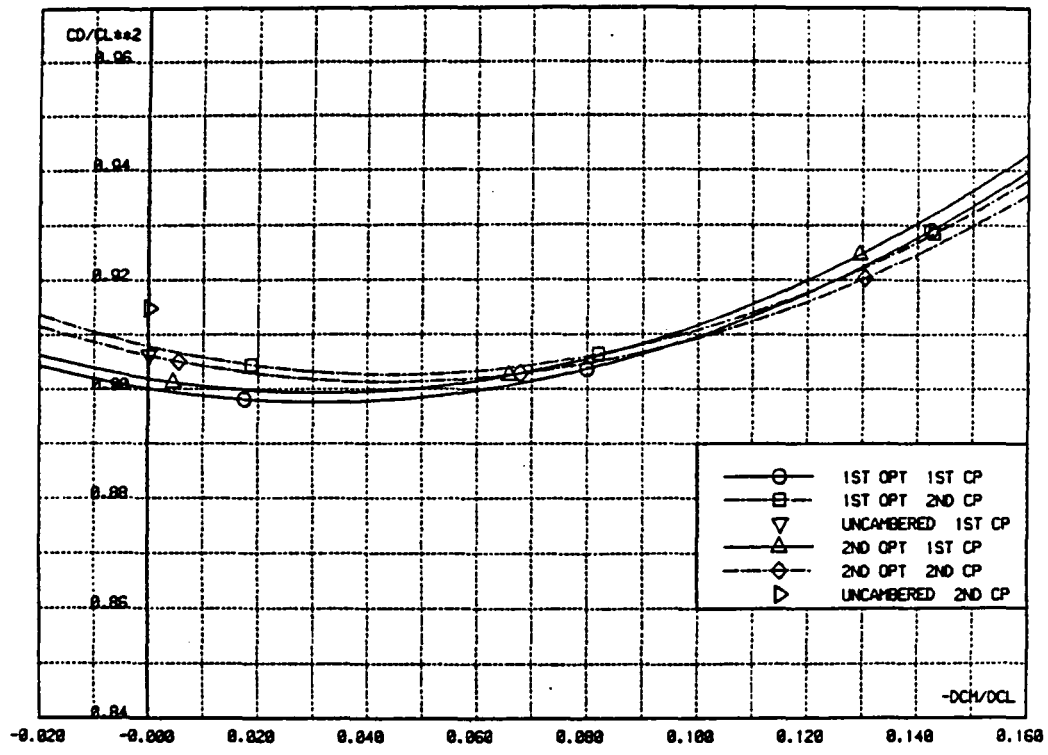

$-dC_M/dC_L$

Figure 6.1.8. First and Second Order Optima for a Supersonic Edge Condition
$M = 4.0$, $C_L = 0.1$

6.2 FULL POTENTIAL

Results from the conservative full potential formulation are presented for both conical and nonconical supersonic flows. The published papers enclosed in the Appendix section cover results for a wide variety of configurations that include a supersonic delta wing, cones at angle of attack, conical thin elliptic wings, and wing-body combinations, circular arc-cylinder body, and nonconical arrow-wing body combination.

One additional result not presented in the Appendix is reported in this section. Figures 6.2.1 and 6.2.2 show the grid arrangement at various marching planes for the Sears-Haack wing-body combination. The grid is smooth around the sharp leading edge generated using the double domain grid generation procedure described in Figure 5.1. The pressure distribution on the flat upper surface of the wing for $M_\infty = 6$, $\alpha = -4^\circ$ is shown in Figure 6.2.3 at the axial station $x/\ell = 0.759$. These are preliminary results from the code and further improvements are possible with the use of the newly developed discrete geometry input option. This will be pursued in the follow-on program.

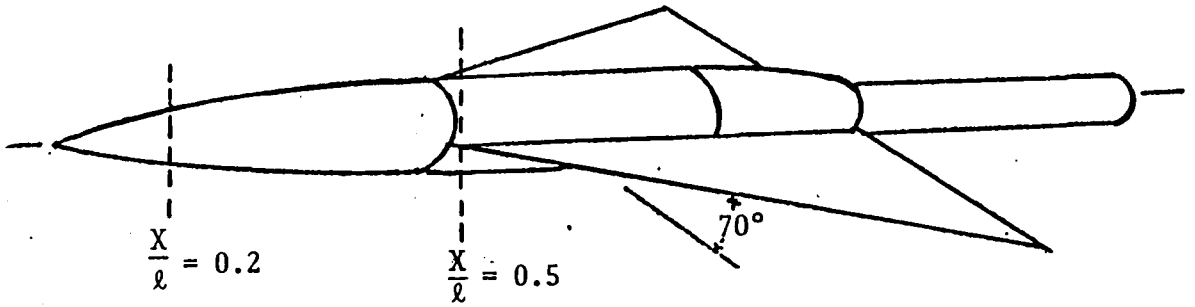

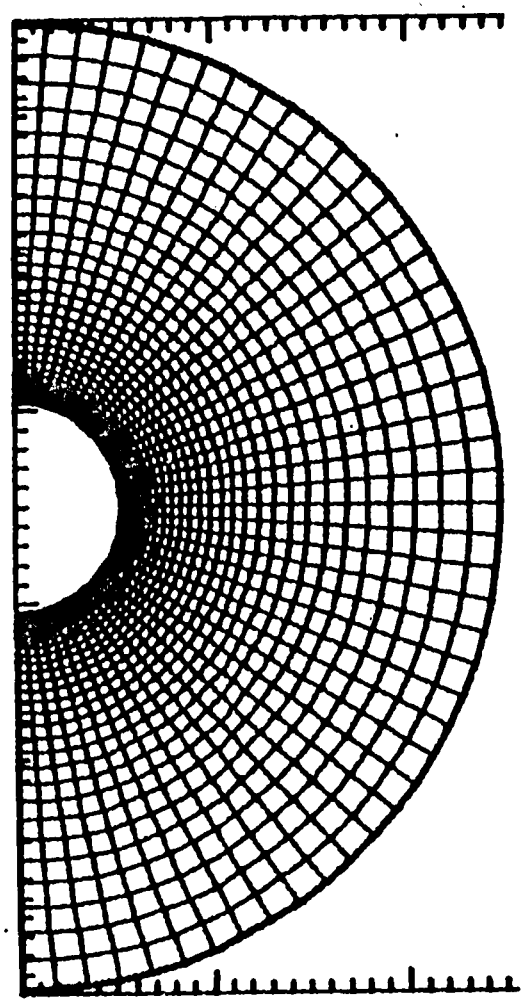

X/ℓ = 0.2

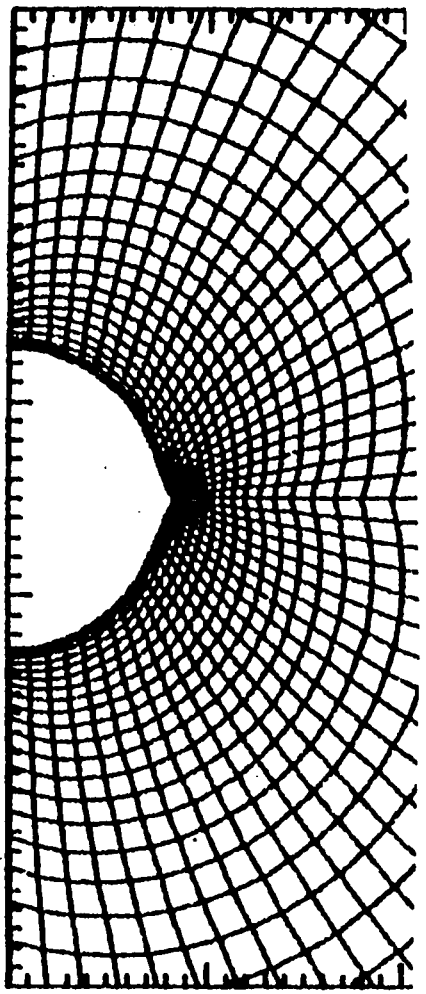

X/ℓ = 0.5

Figure 6.2.1. Grid Distribution for Sears-Haack Wing-body Combination

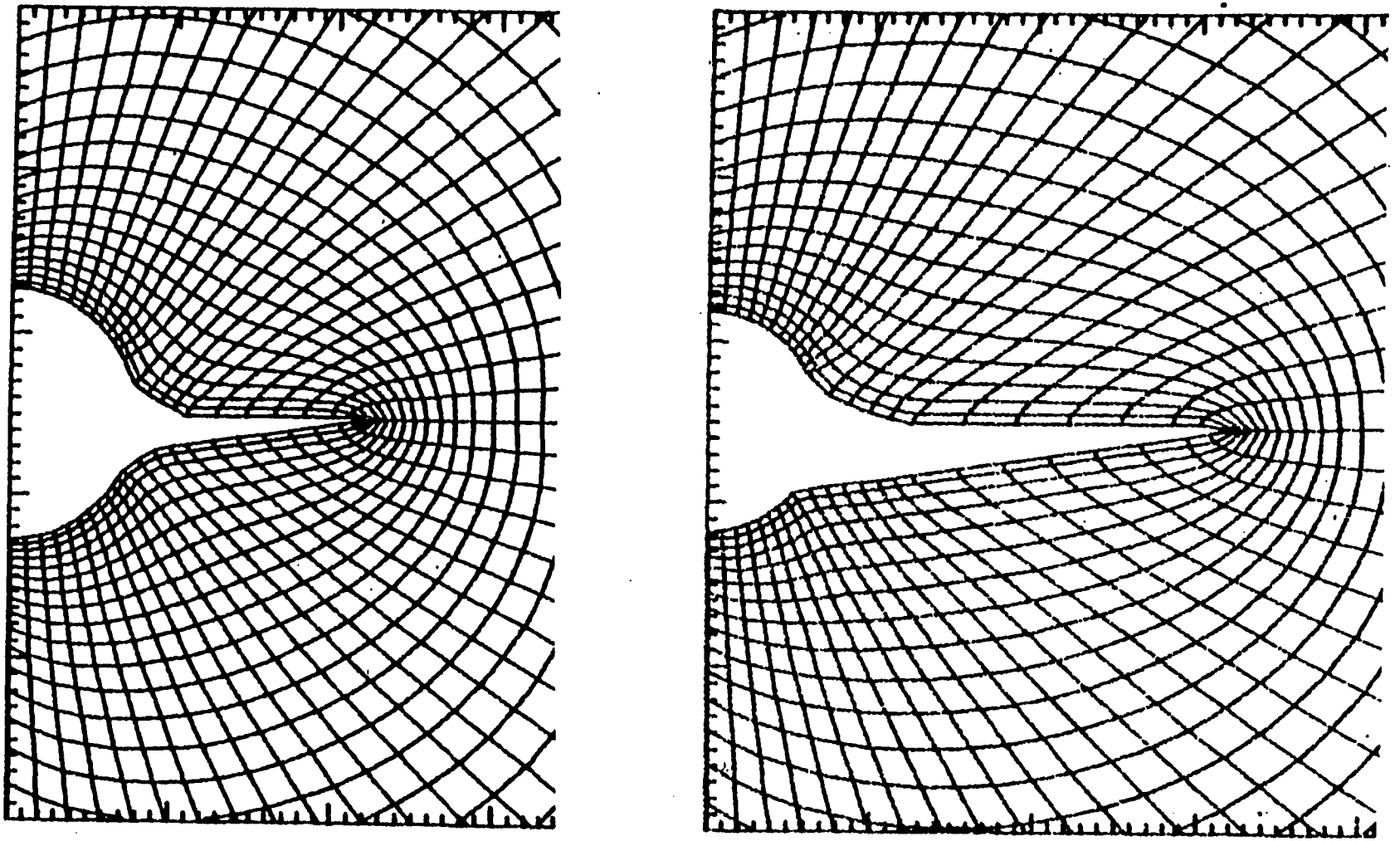

$\frac{X}{\ell} = 0.75$ $\frac{X}{\ell} = 0.95$

Figure 6.2.2. Grid Distribution at $\frac{X}{\ell} = 0.75$ and $\frac{X}{\ell} = 0.95$ for Sears-Haack Wing-Body Combination

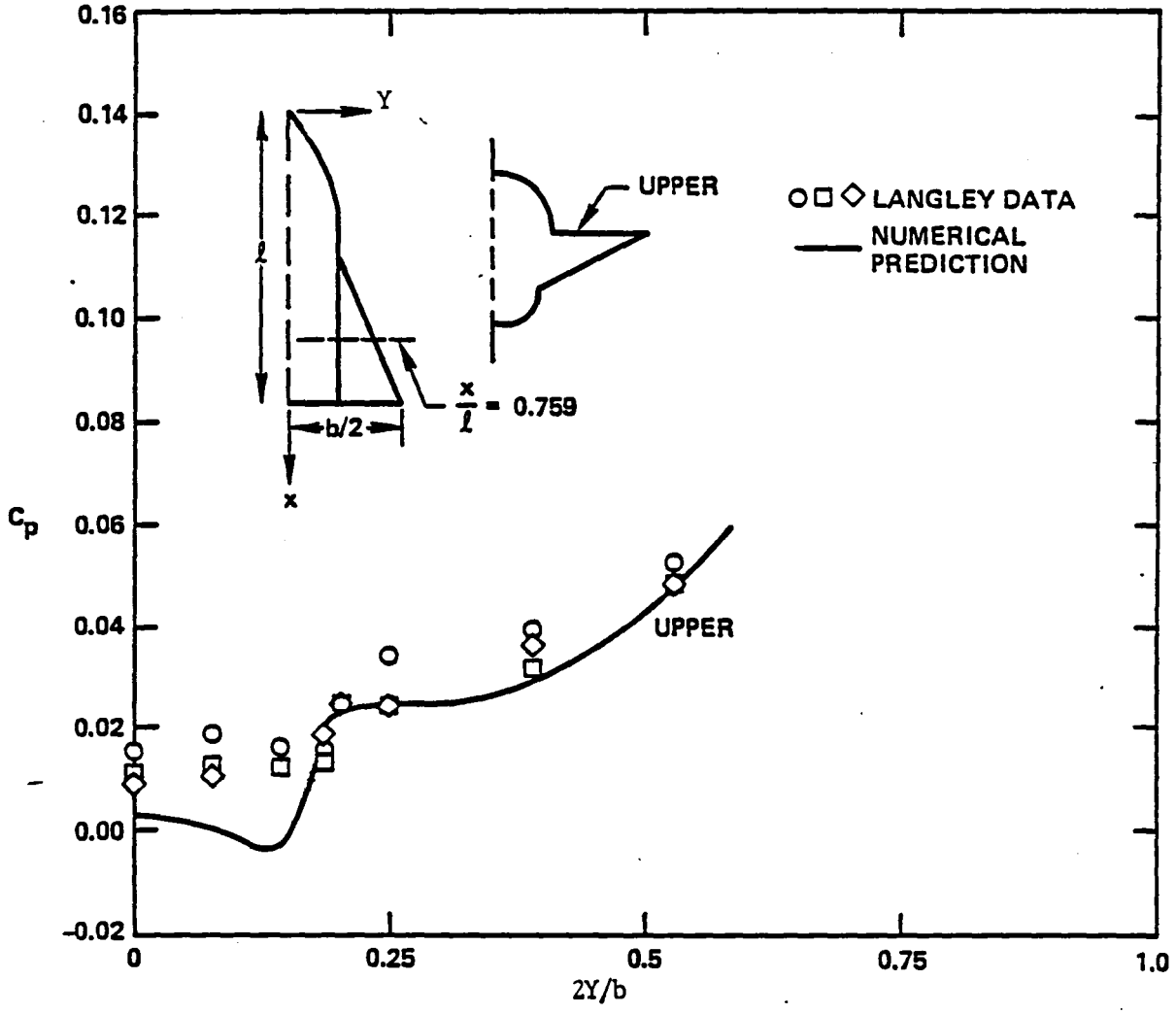

Figure 6.2.3. Sears-Haack Wing-Body Pressure Distribution at $M_\infty = 6.0$ and $\alpha = -4°$

7. CONCLUSIONS

Based on the theoretical development and comparison with higher order results/experimental measurements described in this document, the following conclusions are made.

1. Improved prediction of supersonic/hypersonic aerodynamic characteristics and surface pressures for general wing-body shapes has been demonstrated using nonlinear potential analysis for values of the hypersonic similarity parameter, $M\delta$, less than one.

2. Second order theory provides a systematic means of extending linear analysis for full configurations. Thirty second CPU solution time/Mach number is typical for a wing-body-canard analysis or wing-body optimization problems.

3. Full potential analysis successfully eliminates subsonic edge singularities and linear characteristics approximations of second order theory. The formulation is an order of magnitude faster than Euler solvers while maintaining comparable prediction accuracy.

4. Potential theory provides an advanced aerodynamic prediction technique that is responsive to the preliminary design problem at moderate hypersonic conditions.

8. REFERENCES

1. Clever, W. C., Malmuth, N. D., and Shankar, V., "Formulation of Aerodynamic Prediction Techniques for Hypersonic Configuration Design," NASA CR-158994, February 1979.

2. Clever, W. C. and Shankar, V., "Aerodynamic Prediction Techniques for Hypersonic Configuration Design," NASA CR-165651, March 1981.

3. Gunness, R. C., Knight, C. J., and Sylva, I.D., "Flow Field Analysis of Aircraft Configurations using a Numerical Solution to the Three Dimensional Unified Supersonic/Hypersonic Small-Disturbance Equations," NASA CR-1926, February 1972.

4. Shankar, V., "Conservative Full Potential, Implicit Marching Scheme for Supersonic Flows," AIAA Journal Vol. 20, No. 11 November 1982.

5. Shankar, V., "An Efficient Full Potential Implicit Method Based on Characteristics for Analysis of Supersonic Flows," AIAA Paper 82-0974, June 1982.

APPENDIX A CONTRACT PUBLICATIONS*

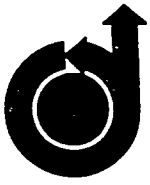

AIAA 81-1004R
Conservative Full Potential, Implicit Marching Scheme for Supersonic Flows

V. Shankar

* PERMISSION TO REPRINT THE PAPERS APPEARING IN THIS APPENDIX WAS GRANTED BY AIAA April 4, 1983

Reprinted from
AIAA Journal Volume 20, Number 11, November 1982, Page 1508

AMERICAN INSTITUTE OF AERONAUTICS AND ASTRONAUTICS • 1290 AVENUE OF THE AMERICAS • NEW YORK, NEW YORK, N.Y. 10104

AIAA 81-1004R

Conservative Full Potential, Implicit Marching Scheme for Supersonic Flows

Vijaya Shankar*
Rockwell International Science Center, Thousand Oaks, California

An aerodynamic prediction technique based on the full potential equation in conservation form is developed for the treatment of supersonic flows. This technique bridges the gap between simplistic linear theory methods and complex Euler solvers. A local density linearization concept and a second-order-accurate retarded density scheme, both producing the correct artificial viscosity, are introduced in developing an implicit marching scheme for solving the scalar potential ϕ. Results for conical flows over delta wings, cones, and wing-body combinations, and for nonconical flows over bodies of revolution at angles of attack are compared with Euler and nonconservative full potential calculations and experimental data. The present formulation requires an order of magnitude less computer time and significantly less computer memory over Euler methods.

I. Introduction

AERODYNAMIC prediction techniques that can handle significant geometric complexity for use in supersonic or hypersonic configuration design are based on either hypersonic impact methods[1] or linear theory analysis,[2] both of which require minimum response time and cost. However, shortcomings are present in both the impact and linearized methods. Aside from these simplified techniques, limited capabilities also exist for calculating supersonic flowfields using very complex Euler codes,[3-6] using either shock capturing[3] or shock fitting[4-6] methods. The use of these codes as viable aerodynamic prediction techniques for configuration design is, however, not practical due to their slow response time (requirement of large computer memory) and excessive computer cost per run due to strict stability requirements. Thus, we have on one end of the spectrum, very simplified codes that require minimum computer time to provide less accurate results and, on the other end, very complex Euler codes that require excessive computer time to provide quality results.

In an attempt to bridge this gap between simplistic linear theory methods and complex Euler solvers, several methodologies such as the second-order potential analysis,[7] hypersonic small disturbance theory,[8] and, more recently, nonconservative full potential methods[9,10] have been considered by various investigators. The second-order theory,[7] in spite of the significant improvements reported, suffers from the lack of nonlinearity in resolving proper cross flow shocks and sonic lines. Also, the singularities inherent in the formulation create difficulties in the numerical treatment of subsonic leading edges. The finite difference analysis of the hypersonic small disturbance theory[8] indicates that the solution procedure is as complex as that for the Euler equation and not particularly responsive to preliminary design level of effort.

Recently, Grossman[9] and Grossman and Siclari[10] have computed supersonic flowfields over conical and nonconical cambered and twisted delta wings with remarkable success using the nonconservative full potential equation and a transonic relaxation method. However, their approach is made complicated by the use of global conformal mappings which apply only to certain classes of configurations. Also, the nonconservative form of the full potential equation is in terms of second derivatives of the potential ϕ, which, when a transformation is applied, generates a large number of first and second derivative transformation terms.

The full potential method proposed in this paper is significantly different from that of Refs. 9 and 10. First of all, the method is based on the conservative form of the full potential equation, since for a shock capturing procedure to conserve mass across the shock wave,[11] it is essential that the equation be cast in conservation form.[12] Second, the method can accommodate a numerical or analytical mapping procedure that is either orthogonal or nonorthogonal without complicating the form of the equation, in contrast to Refs. 9 and 10. Third, the method is based on an approximate factorization implicit algorithm that can yield convergence much faster than the conventional successive line over-relaxation method.[10] Finally, the method is not an adaptation of a transonic code using type dependent operators, but a scheme specifically developed and tailored for supersonic marching problems using a density linearization concept and has no step size restrictions.

To validate the present methodology, results are shown for a variety of conical and nonconical geometries and are compared with Euler solutions and full potential results of Refs. 9 and 10. Results indicate that the method works just as fast and efficient for nonconical flows as in the case of conical geometry treatment. Results also indicate that the method is very useful in computing very high-speed flows ($M_\infty \sim 2$-6) for the moderate flow deflection angles ($\alpha \sim 4$-10 deg) where the neglect of entropy generation does not seriously distort the main features of the flowfield.

The present method can also handle more complicated geometries (realistic wing-body combinations) than the ones reported in the paper, but requires a suitable grid generation routine, especially near wing-body junction regions. In a subsequent paper,[13] results for nonconical wing-body flows will be presented along with a formal method of characteristics treatment for cross flow signal propagation.

II. Formulation

The conservative form of the full potential equation in Cartesian coordinates x, y, z can be written as

$$\frac{\partial(\rho u)}{\partial x} + \frac{\partial(\rho v)}{\partial y} + \frac{\partial(\rho w)}{\partial z} = 0 \tag{1}$$

where ρ is the density and u, v, w are the velocity components. They are calculated as the gradient of the potential ϕ,

$$u = \phi_x; \quad v = \phi_y; \quad w = \phi_z \tag{2}$$

Presented as Paper 81-1004 at the AIAA Fifth Computational Fluid Dynamics Conference, Palo Alto, Calif., June 22-23, 1981; submitted June 24, 1981; revision received March 22, 1982.

*CFD Project Leader. Associate Fellow AIAA.

The density ρ is computed from the isentropic formula

$$\rho=\left[1-\frac{\gamma-1}{2}M_\infty^2(u^2+v^2+w^2-1)\right]^{1/\gamma-1} \tag{3}$$

If the density is normalized with respect to the freestream value, then the speed of sound a is given by

$$a^2=\rho^{\gamma-1}/M_\infty^2 \tag{4}$$

where M_∞ is the freestream Mach number.

The objective of the paper is to solve for the scalar potential ϕ from Eq. (1) subject to the surface tangency condition $\phi_n=0$ (n is normal to the body surface). Examining Eq. (1), it is very clear that ϕ appears in a nonlinear form due to the presence of the density term inside the derivative. The approach to be described here is a method that treats the density term in such a way that it produces the correct artificial viscosity needed for shock capturing and that enables one to solve for ϕ with relative ease.

In order to apply the surface tangency condition at the actual body location, a body-fitted coordinate transformation is essential. Introducing a body-fitted coordinate transformation, $\zeta=\zeta(x,y,z)$, $\eta=\eta(x,y,z)$, and $\xi=\xi(x,y,z)$, Eq. (1) transforms to

$$\left(\rho\frac{U}{J}\right)_\zeta+\left(\rho\frac{V}{J}\right)_\eta+\left(\rho\frac{W}{J}\right)_\xi=0 \tag{5}$$

where U, V, and W are the contravariant velocity components. Introducing the following notation for convenience:

$$U=U_1,\quad V=U_2,\quad W=U_3$$

$$x=x_1,\quad y=x_2,\quad z=x_3$$

$$\zeta=X_1,\quad \eta=X_2,\quad \xi=X_3$$

the contravariant velocities and density are given by

$$U_i=\sum_{j=1}^{3}a_{ij}\phi_{x_j}\qquad i=1,2,3$$

$$a_{ij}=\sum_{k=1}^{3}\frac{\partial X_i}{\partial x_k}\frac{\partial X_j}{\partial x_k}\qquad i=1,2,3,\quad j=1,2,3$$

$$\rho=\left[1-\left(\frac{\gamma-1}{2}\right)M_\infty^2\{U\phi_\zeta+V\phi_\eta+W\phi_\xi-1\}\right]^{1/(\gamma-1)} \tag{6}$$

The Jacobian of the transformation J is represented by

$$J=\frac{\partial(\zeta,\eta,\xi)}{\partial(x,y,z)}=\begin{bmatrix}\zeta_x & \zeta_y & \zeta_z\\ \eta_x & \eta_y & \eta_z\\ \xi_x & \xi_y & \xi_z\end{bmatrix} \tag{7}$$

Equation (5) is in terms of a general coordinate system (ζ,η,ξ) and can accommodate any kind of mapping procedure, either analytical (conformal mapping) or numerical type. Any numerical marching procedure applied to Eq. (5) to simulate a supersonic flow should have a truncation error whose leading terms represent a correct artificial viscosity. This is essential to ensure marching numerical stability and to exclude the formation of expansion shocks which are unphysical and correspond to a decrease in entropy. The nature of the required artificial viscosity can be studied by an analysis[14] of the canonical form of Eq. (5), which indicates that for stability, the form of artificial viscosity be

$$\frac{\rho}{Ja^2}\left\{1-\frac{a^2}{q^2}\right\}[\Delta\zeta U\{U\phi_{\zeta\zeta\zeta}+V\phi_{\eta\zeta\zeta}+W\phi_{\xi\zeta\zeta}\}$$
$$+\Delta\eta V\{U\phi_{\zeta\eta\eta}+V\phi_{\eta\eta\eta}+W\phi_{\xi\eta\eta}\}$$
$$+\Delta\xi W\{U\phi_{\zeta\xi\xi}+V\phi_{\eta\xi\xi}+W\phi_{\xi\xi\xi}\}] \tag{8}$$

assuming that U, V, W are positive. What this implies is that if the flowfield is hyperbolic ($q>a$), then solution can be obtained by marching along the hyperbolic flow direction s. Once the total velocity q becomes less than a, then marching along s is not possible. This is reflected in the fact that the effective artificial viscosity given by Eq. (8) is now negative.

Now we will proceed with the numerical procedure for solving Eq. (5), and show the resemblance of the resulting artificial viscosity to that of Eq. (8).

A. Treatment of $\frac{\partial(\rho U/J)}{\partial\zeta}$ in Eq. (5)

Consider the direction ζ to be the marching direction. The condition to be satisfied for this to be true will become evident at the end of this analysis. Both the density ρ and the contravariant velocity U are functions of the potential ϕ and the transformation metrics, as represented in Eq. (6). In order to finite difference this ζ derivative quantity in terms of ϕ only will require some linearization treatment of the density. This will be termed the "local density linearization" procedure. In the transonic formulation described by Holst,[15] the density is upwind biased and computed at the old level, while retaining central differencing for the (U/J) term at the current level. Such an upwind density bias is shown to produce the right artificial viscosity in Ref. 14. Referring to Fig. 1, for a pure supersonic marching problem (say we want to march from the ith plane to the $i+1$th plane), a transonic relaxation procedure[15] in the marching direction ζ is not appropriate because the solution ϕ at the $i+1$th plane is not influenced by the $i+2$th plane. Hence, the following marching procedure is developed.

Given the ϕ information at all the previous planes i, $i-1$, $i-2$,..., the problem is to compute ϕ at the $i+1$th plane. Now, expand the unknown $\rho=\rho(\phi)$ in terms of a neighboring known state denoted here by a subscript 0 (ith plane information would represent the neighboring known state for the $i+1$th plane).

$$\rho=\rho_0+\left(\frac{\partial\rho}{\partial\phi}\right)_0\Delta\phi+\ldots \tag{9}$$

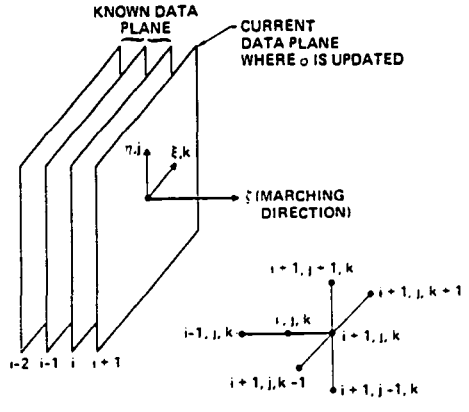

Fig. 1 Implicit computational molecule.

where $\Delta\phi=\phi-\phi_0$ and $\partial\rho/\partial\phi$ can be shown to be a differential operator[16]

$$\left(\frac{\partial\rho}{\partial\phi}\right)_0 \Delta\phi = -\frac{\rho_0}{a_0^2}\left\{U_0\frac{\partial}{\partial\zeta}+V_0\frac{\partial}{\partial\eta}+W_0\frac{\partial}{\partial\xi}\right\}(\phi-\phi_0) \quad (10)$$

Substituting Eqs. (9) and (10) into the first term in Eq. (5), we get

$$\frac{\partial(\rho U/J)}{\partial\zeta} \doteq \frac{\partial}{\partial\zeta}\left(\left[\rho_0-\frac{\rho_0}{a_0^2}\left\{U_0\frac{\partial}{\partial\zeta}+V_0\frac{\partial}{\partial\eta}+W_0\frac{\partial}{\partial\xi}\right\}(\phi-\phi_0)\right]\frac{U}{J}\right) \quad (11)$$

Substituting for U in terms of ϕ from Eq. 6 and rearranging Eq. (11) in terms of the potential difference $\Delta\phi$, we get

$$\frac{\partial(\rho U/J)}{\partial\zeta} \doteq \frac{\partial}{\partial\zeta}\left\{\frac{\rho_0}{J}\left[\left(a_{11}-\frac{U^2}{a^2}\right)_0\frac{\partial}{\partial\zeta}\Delta\phi+\left(a_{12}-\frac{UV}{a^2}\right)_0 \times\frac{\partial}{\partial\eta}\Delta\phi+\left(a_{13}-\frac{UW}{a^2}\right)_0\frac{\partial}{\partial\xi}\Delta\phi+U_0\right]\right\} \quad (12)$$

where the speed of sound a_0, the density ρ_0, and the contravariant velocities U_0, V_0, W_0, represent information at the neighboring known plane. The ζ derivative term of Eq. (12) will now be one-sided differenced. Assuming U is positive,

$$\frac{\partial(\ )}{\partial\zeta}=\frac{1}{\Delta\zeta}\{(\ )_{i+1,j,k}-(\ )_{i,j,k}\} \quad (13)$$

An upwind differencing of the form Eq. (13) applied to Eq. (12) can be shown to produce a truncation term whose leading term is

$$\frac{\rho}{Ja^2}\left\{1-\frac{a^2a_{11}}{U^2}\right\}U^2\phi_{\zeta\zeta\zeta}\Delta\zeta \quad (14)$$

which will always represent a positive artificial viscosity as long as

$$\frac{U^2}{a_{11}}>a^2 \quad (15)$$

The preceding relation sets the condition for ζ to be the marching direction, for if U^2/a_{11} is less than the square of the local speed of sound, then the artificial viscosity becomes negative and a marching instability will occur. This also implies that the projection of the total velocity vector q in the direction normal to the $\zeta=$const plane (η,ξ plane) is supersonic. For example, in a spherical system, for the radial direction r to be the marching direction, the radial velocity q_r must be supersonic. The similarity between the artificial viscosity term given by Eq. (14) and the first term appearing in Eq. (8) can be noted. When backward differenced, the terms in Eq. (12) will lead to a diagonally dominant tridiagonal set of equations for the unknown $\Delta\phi$ when coupled with the other two terms in Eq. (5). The mixed derivative terms like $\phi_{\zeta\eta}$ and $\phi_{\xi\xi}$ appearing in Eq. (12) will be upwind biased, depending on the sign of the coefficient multiplying them to preserve diagonal dominance and to provide the right artificial viscosity.

B. Treatment of $\frac{\partial(\rho V/J)}{\partial\eta}$ in Eq. (5)

This term will be written at the $i+1$th plane to make the resulting scheme fully implicit.

$$\frac{\partial(\rho V/J)}{\partial\eta}=\frac{\partial}{\partial\eta}\left\{\frac{\rho}{J}(a_{21}\phi_\zeta+a_{22}\phi_\eta+a_{23}\phi_\xi)\right\} \quad (16)$$

The density term ρ in Eq. (16) cannot be represented at the $i+1$th plane since that would result in a very complicated nonlinear form for ϕ. Hence, a density approximation is introduced by setting $\rho=\rho^*$ where $\rho^*=\rho_0$ for conical flow treatment. In the case of nonconical flows, while advancing from i to the $i+1$th plane, several iterations are performed within each cross flow plane (η,ξ) to refine the density ρ^* to properly account for the axial geometry variation. This is done by initially setting ρ^* to ρ_0 and then subsequently refining it by setting ρ^* to the previous iterate value of ρ at the current plane. In many cases where the axial variation of the geometry is gradual (especially for smaller step size calculations) it was found that setting $\rho^*=\rho_0$ even for nonconical flows produced very good results without having to refine the density subsequently.

Writing Eq. (16) in terms of the potential difference $\Delta\phi$

$$\frac{\partial(\rho V/J)}{\partial\eta} \doteq \left(\frac{\rho^*a_{21}}{J}\frac{\Delta\phi}{\Delta\zeta}\right)_\eta+\left(\frac{\rho^*a_{22}}{J}\frac{\partial}{\partial\eta}\Delta\phi\right)_\eta +\left(\frac{\rho^*a_{23}}{J}\frac{\partial}{\partial\xi}\Delta\phi\right)_\eta+\left(\frac{\rho^*a_{22}}{J}\frac{\partial}{\partial\eta}\phi_0\right)_\eta+\left(\frac{\rho^*a_{23}}{J}\frac{\partial}{\partial\xi}\phi_0\right)_\eta \quad (17)$$

A simple central differencing for the various terms in Eq. (17) will not be sufficient as that would not provide the desired artificial viscosity given by Eq. (8), required for shock capturing. To simulate an artificial viscosity of the form given by Eq. (8), the density will be upwind biased based on the previous work reported in Refs. 14-16. The density ρ^* will be replaced by a modified density $\tilde{\rho}^*$ given by

$$(\tilde{\rho}^*)_{j+\frac{1}{2},k}=(1-\nu_{j+\frac{1}{2},k})(\rho^*)_{j+\frac{1}{2},k} +\tfrac{1}{2}\nu_{j+\frac{1}{2},k}\{(1+\theta)(\rho^*)_{j+2m,k}+(1-\theta)(\rho^*)_{j-1+2m,k}\} \quad (18)$$

where $m=0$ when $(V_0)_{j+\frac{1}{2},k}>0$ and $m=+1$ when $(V_0)_{j+\frac{1}{2},k}<0$. When θ is set to zero, first-order accurate density biasing is achieved while $\theta=2$ gives second-order accuracy. The artificial viscosity coefficient $\nu_{j+\frac{1}{2},k}$ is computed as follows:

$$\nu_{j+\frac{1}{2},k}=[1-(a_0^2/q_0^2)]_{j+s,k} \quad (19)$$

where $s=0$ for $V_{j+\frac{1}{2},k}>0$ and $s=1$ for $V_{j+\frac{1}{2},k}<0$.

Treatment of density as represented by Eqs. (18) and (19) would always produce a positive artificial viscosity as long as the local total velocity q_0 is supersonic. If that becomes subsonic, then the marching procedure would fail and the problem have to be treated as a transonic problem.

The treatment of the $(\partial/\partial\xi)[\rho W/J]$ term in Eq. (5) is very similar to the just described $(\partial/\partial\eta)[\rho V/J]$ term, except that the density biasing will be in the ξ direction and will be based on the sign of W.

C. Implicit Factorization Algorithm

Combining the various terms in Eqs. (12) and (17), and the terms arising from $(\partial/\partial\xi)[\rho W/J]$ will result in a fully implicit representation of Eq. (5) which cannot be solved without introducing an approximate factorization procedure. After some rearrangement of the terms, the factored implicit scheme becomes

$$\left[1+\frac{A_3}{\beta\Delta\zeta}\frac{\partial}{\partial\xi}+\frac{1}{\beta}\frac{\partial}{\partial\xi}\left(\frac{\tilde{\rho}^*}{J}\frac{a_{31}}{\Delta\zeta}\right)+\frac{1}{\beta}\frac{\partial}{\partial\xi}\frac{\tilde{\rho}^*a_{33}}{J}\frac{\partial}{\partial\xi}\right] \times\left[1+\frac{A_2}{\beta\Delta\zeta}\frac{\partial}{\partial\eta}+\frac{1}{\beta}\frac{\partial}{\partial\eta}\left(\frac{\tilde{\rho}^*a_{21}}{J\Delta\zeta}\right) +\frac{1}{\beta}\frac{\partial}{\partial\eta}\frac{\tilde{\rho}^*a_{22}}{J}\frac{\partial}{\partial\eta}\right]\Delta\phi=R \quad (20)$$

This equation has the form

$$L_\xi L_\eta(\Delta\phi) = R \tag{21}$$

and it is implemented as follows:

$$L_\xi(\Delta\phi)^* = R \qquad L_\eta(\Delta\phi) = (\Delta\phi)^* \qquad \phi = \phi_0 + \Delta\phi \tag{22}$$

The various quantities appearing in Eq. (20) are given by

$$\beta = \frac{A_1}{(\Delta\zeta)^2} \qquad A_1 = \frac{\rho_0}{J}\left(a_{11} - \frac{U^2}{a^2}\right)_0$$

$$A_2 = \frac{\rho_0}{J}\left(a_{12} - \frac{UV}{a^2}\right)_0 \qquad A_3 = \frac{\rho_0}{J}\left(a_{13} - \frac{UW}{a^2}\right)_0 \tag{23}$$

and the right-hand side term R consists of various known quantities.

The algorithm Eq. (22) requires only scalar tridiagonal inversions. Also, the scheme does not pose any restrictions on the direction of sweep that are present in the successive line over-relaxation method.[9,10]

D. Freestream Truncation Errors

To subtract out any numerical truncation error due to incomplete metric cancellation,[16] it is essential to add the terms (especially for a highly stretched nonorthogonal grid)

$$\frac{\partial}{\partial\zeta}\left(\frac{\rho_\infty U_\infty}{J}\right) + \frac{\partial}{\partial\eta}\left(\frac{\rho_\infty V_\infty}{J}\right) + \frac{\partial}{\partial\xi}\left(\frac{\rho_\infty W_\infty}{J}\right) \tag{24}$$

to the right-hand side of Eq. (20).

E. Boundary Conditions

In order to solve for $\Delta\phi$ from Eq. (20), boundary conditions will have to be prescribed at all four boundaries as shown in Fig. 2 at the current $i+1$th plane. While performing the L_ξ operator in Eq. (21), boundary conditions in terms of $\Delta\phi^*$ will be required along the $k=2$ and $k=KMAX-1$ boundaries. For a pure angle-of-attack problem, $k=2$ and $k=KMAX-1$ can be considered as planes of symmetry across which all flow variables reflect. The quantity $\Delta\phi^*$, even though it has no physical significance, can be safely set

$$(\Delta\phi)^*_{i+1,j,KMAX} = (\Delta\phi)^*_{i+1,j,KMAX-2}$$

$$(\Delta\phi)^*_{i+1,j,1} = (\Delta\phi)^*_{i+1,j,3} \tag{25}$$

The L_η operator would require boundary conditions along $j=2$ and $j=JMAX$ in terms of $\Delta\phi$. Since $j=2$ is the body, the surface tangency condition

$$V = a_{21}\phi_\zeta + a_{22}\phi_\eta + a_{23}\phi_\xi = 0 \tag{26}$$

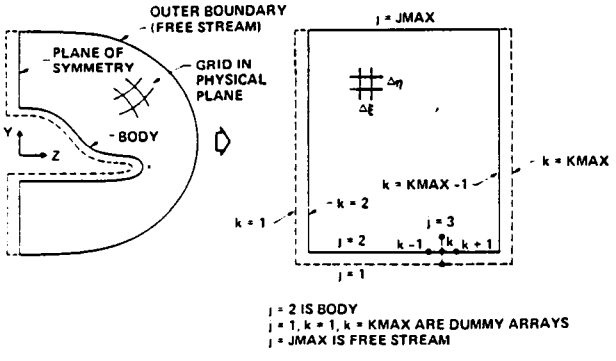

Fig. 2 Physical and computational plane.

will be set at all points $(i+1,2,k)$. Along $j=JMAX$, freestream $\Delta\phi$ will be imposed.

F. Grid System

As shown in Fig. 2, the physical space (x,y,z) is transformed into a body-fitted (ζ,η,ξ) computational space. The transformation is performed numerically by using the elliptic grid generation techniques originally developed by Thompson et al.,[17] and later modified by Steger and Sorenson,[18] and Middlecoff and Thomas.[19] The present full potential method does not require an orthogonal grid; however, the error introduced by the approximate factorization, Eq. (20), can be minimized if the grid is orthogonal in the cross flow plane (η,ξ). For conical flow calculations, the grid is generated only once, and, as the marching procedure continues, the grid is allowed to grow conically. For a general nonconical body, it would be necessary to construct the grid in every marching plane.

III. Results

Results are presented for both conical and nonconical supersonic flows. Comparisons are made with Euler[3,5] and full potential[9,10] results and experimental data. All the calculations were performed using a CDC 7600 machine.

A. Conical Flows

Besides validating the methodology, computation of conical flows is of interest for generating the initial data plane for nonconical calculations. For a conical geometry (radially invariant), the initial data plane with freestream conditions is chosen at some location $\zeta=\zeta_0$ (usually set at $\zeta=1$). The solution is then marched along ζ using Eq. (20) and boundary conditions. The conical flow calculation is assumed to have converged when the change in the root mean square density is less than 10^{-4}.

Supersonic Leading-Edge Delta Wing

Figure 3 shows the compression surface pressures for a supersonic leading-edge delta wing at $M_\infty=6$, angle of attack $\alpha=-8$ deg, and leading-edge sweep $\Lambda=70$ deg. The present full potential solution compares well with the Euler solution[19] and experimental data. Also shown are the results from the first- and second-order linear theory.[7] Using a 30×40 grid in the (η,ξ) plane, the present approach required 40 iterations to achieve convergence, and 12-15 s of computer time to produce the results shown in Fig. 3.

It is interesting to note that in spite of the limitations of the full potential theory, even at a very high Mach number of 6, the comparison is in reasonable agreement with the Euler

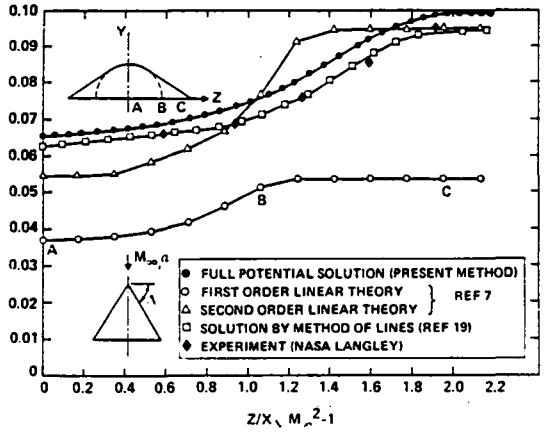

Fig. 3 Predicted compression surface pressure for a 70-deg sweep delta wing at $M_\infty=6$, $\alpha=-8$ deg.

solution and is significantly better than the second-order theory. The discrepancy between the full potential and Euler results is mainly due to neglect of entropy generation in the present approach.

Circular Cone and Ellipse

Figure 4 shows the surface pressure distribution for a circular cone, half angle 7.5 deg, $M_\infty = 3$ at 15 deg angle of attack. At this angle of attack the cross flow Mach number becomes supersonic as the flow turns around the cone from the windward symmetry to the leeward symmetry. This cross flow supersonic region is terminated by the formation of an embedded shock on the cone surface. This is evident from the results of Fig. 4. Grid clustering near the cross flow shock was used both in the Euler calculation of Kutler,[3] and in the present method, to finely resolve the pressure jump. The present calculation required 25 s of computer time, using a 30×60 grid in the (η, ξ) plane.

The liftoff of the vortical singularity on the leeward symmetry plane associated with the formation of the embedded shock is shown in Fig. 5. The location where the contravariant velocity V goes through zero on the leeward symmetry plane ($W = 0$) denotes the location of the vortical singularity. The behavior of the cross flow streamlines converging to the vortical singularity is also shown in Fig. 5.

Figure 6 shows the full potential and Euler cross flow Mach number contours for the circular cone case. The presence of the embedded shock wave in both the results is very clear. The location of the vortical singularity liftoff is also shown in the figure. The Euler result is very oscillatory near the vortical singularity location while the present method predicts a smoother flowfield in the vicinity of the vortical singularity.

The surface pressure distribution on an elliptic cone $\theta_c = 18.39$ deg, $\delta_c = 3.17$ deg at $M_\infty = 1.97$ and $\alpha = 10$ deg is shown in Fig. 7. The results of the present study are compared with Euler calculations of Siclari,[5] full potential results of Grossman,[9] and the linearized thin wing solution of Jones and Cohen.[20] The agreement between the various nonlinear methods is very good, including the position and strength of the embedded shock wave.

Wing-Body Combination

Figure 8 shows the numerically generated grid distribution in the cross flow plane (η, ξ) of a conical wing-body combination. The design of this conically cambered delta wing to achieve shockless recompression is reported in Ref. 21. Figure 9 shows the pressure distribution around this wing-body combination at $M_\infty = 2$, and $\alpha = 7.81$ deg. The leading-edge sweep Λ is 57 deg. The comparison of the results from the present method with the experimental data[21] is excellent. The calculation used a 15×49 grid in the (η, ξ) plane and required less than a minute of computer time.

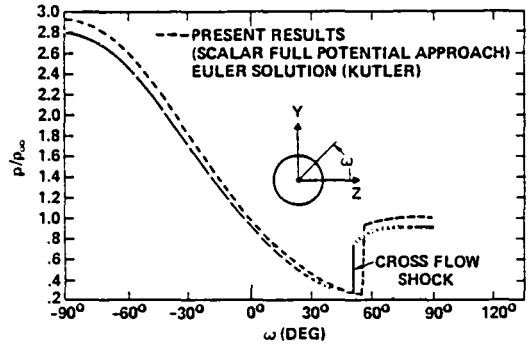

Fig. 4 Surface-pressure distribution for cone at angle of attack; $M_\infty = 3$, $\alpha = 15$ deg, $\theta_c = 7.5$ deg.

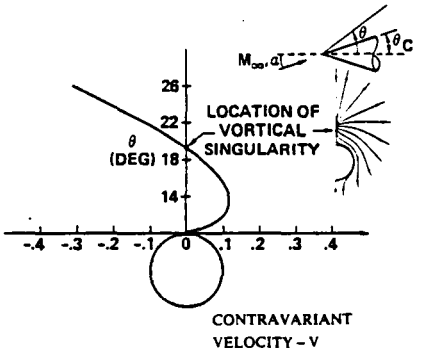

Fig. 5 Vortical singularity liftoff for a circular cone at $M_\infty = 3$, $\alpha = 15$ deg, $\theta_c = 7.5$ deg.

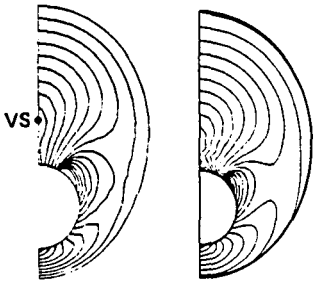

Fig. 6 Comparison of cross flow Mach number contours for cone at angle of attack; $M_\infty = 3$, $\alpha = 15$ deg, $\theta_c = 7.5$ deg (VS = vortical singularity).

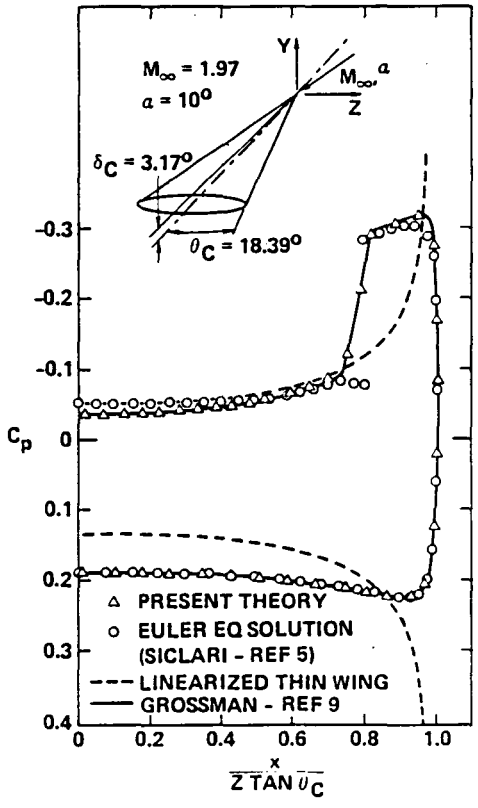

Fig. 7 Surface-pressure distribution on an elliptic cone; $M_\infty = 1.97$, $\theta_c = 18.39$ deg, $\delta_c = 3.17$ deg, $\alpha = 10$ deg.

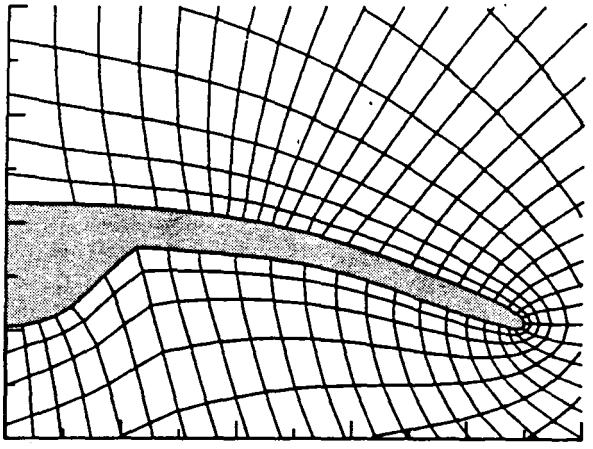

Fig. 8 Computational grid around a wing-body combination.

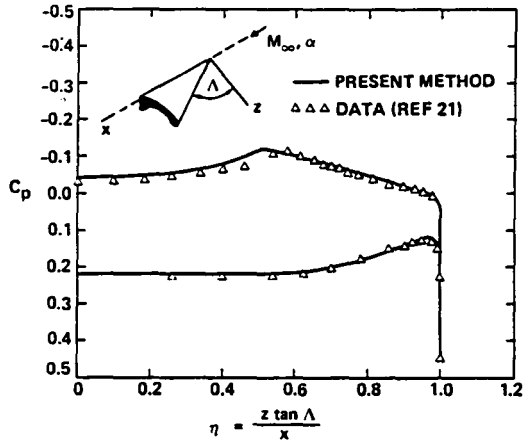

Fig. 9 Surface-pressure distribution for a conically cambered wing-body combination; $M_\infty = 2$, $\alpha = 7.81$ deg, $\Lambda = 57$ deg.

B. Nonconical Flows

Results are also presented for nonconical bodies of revolution and compared with experimental data. The initial data plane for the nonconical marching calculation is first obtained by performing a conical calculation over an assumed very small conical nose. This conical calculation usually takes 20-30 iterations on a typical 30×30 grid in the (η, ξ) plane. The nonconical calculations did not exhibit any increase in computational time over the conical procedure. As mentioned earlier, for the applications considered here where the cross flow station does not vary substantially from the previous one, it was found that there was no need to iterate the solution at each cross flow plane (η, ξ) to converge the density, and plottable accuracy was achieved by simply marching right along the body. However, if the body changes shape appreciably, the current implicit procedure might take 3-5 iterations per cross flow plane to refine the solution.

Reference 22 contains experimental data for several bodies of revolution at various Mach numbers and angles of attack. The shape chosen for comparison here is a circular arc-cylinder body. After the initial data plane was computed using a conical nose assumption, the current method typically used 60 marching steps to reach the end of the body but the calculations are not subject to any step size restriction. A typical calculation required 40-45 s of computer time. Figure 10 shows the circumferential surface pressure distribution at two different axial stations ($x/\ell = 0.225$ and 0.425) for 4 and 8 deg angles of attack at $M_\infty = 2.3$. The results from the present method are compared with experimental data,[22] showing very good agreement for the windward region with some

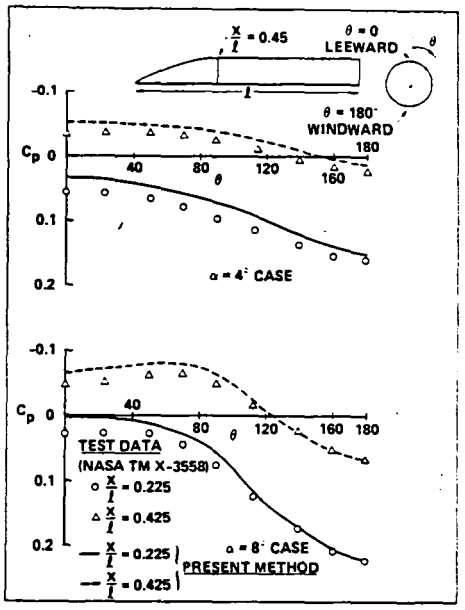

Fig. 10 Circumferential pressure distribution for a circular-arc-cylinder body at $M_\infty = 2.3$.

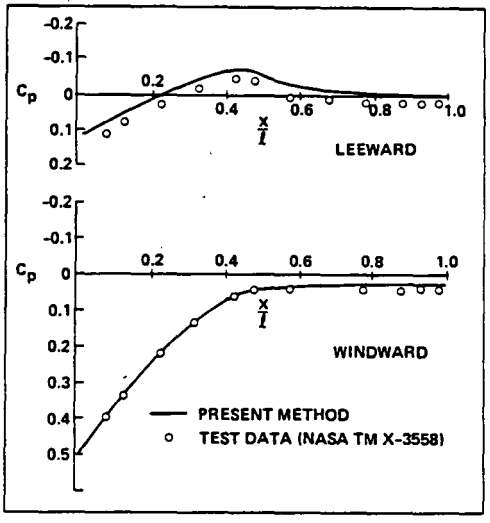

Fig. 11 Surface-pressure distribution for a circular-arc-cylinder body at $\alpha = 8$ deg, $M_\infty = 2.3$.

discrepancy on the leeward side, possibly due to boundary-layer buildup.

Figure 11 shows the surface pressure distribution in the axial direction along the windward and leeward plane of symmetry, at $M_\infty = 2.3$ and $\alpha = 8$ deg. Again, results from the present method compare very well with the experimental data.[22]

IV. Conclusions

An aerodynamic prediction technique based on the full potential equation in conservation form is developed for the treatment of supersonic flowfields. A local density linearization concept and a second-order accurate density biasing scheme are introduced in developing an implicit marching procedure. The method produces results that compare well with Euler solvers, and requires an order of magnitude less computer time and significantly less computer memory over existing Euler codes for the cases presented in the paper. In a subsequent paper,[13] results for more complicated nonconical wing-body flows are presented, along

with a formal theory for the characteristic signal propagation in the cross flow plane.

Acknowledgment

This work was supported in full by NASA Langley Research Center under Contract NAS1-15820.

References

[1] Brooke, D. and Vondrasek, D. V., "Feasibility of Combining Linear Theory and Impact Theory Methods for the Analysis and Design of High Speed Configurations," NASA CR 3069, Dec. 1978.

[2] Woodward, F. A., Tinoco, E. N., and Larsen, J. W., "Analysis and Design of Supersonic Wing-Body Combinations, Including Flow Properties in the Near Field. Part I—Theory and Application," NASA CR 73106, 1967.

[3] Kutler, P., "Computation of Three-Dimensional, Inviscid Supersonic Flows," *Lecture Notes in Physics*, Vol. 41, Springer-Verlag, New York, 1975, pp. 293-374.

[4] Marconi, F., Salas, M., and Yeager, L., "Development of a Computer Code for Calculating the Steady Super/Hypersonic Inviscid Flow Around Real Configurations, Vol. I—Computational Techniques," NASA CR 2675, April 1976.

[5] Siclari, M. J., "Investigation of Cross Flow Shocks on Delta Wings in Supersonic Flow," *AIAA Journal*, Vol. 18, Jan. 1980, p. 85.

[6] Moretti, G., "Conformal Mappings for the Computation of Steady Three-Dimensional Supersonic Flows," *Numerical/Laboratory Computer Methods in Fluids Mechanics*, edited by A. A. Pouring and V. I. Shah, ASME, New York, 1979, pp. 13-28.

[7] "Formulation of Aerodynamic Prediction Techniques for Hypersonic Configuration Design," NASA CR 158994, Feb. 1979.

[8] Gunness, R. C. Jr., Knight, C. J., and Sylvia, E. D., "Flow Field Analysis of Aircraft Configurations using a Numerical Solution to the Three-Dimensional Unified Supersonic/Hypersonic Small-Disturbance Equations," NASA CR 1926, Feb. 1972.

[9] Grossman, B., "Numerical Procedure for the Computation of Irrotational Conical Flows," *AIAA Journal*, Vol. 17, Aug. 1979, pp. 828-837.

[10] Grossman, B. and Siclari, M. J., "The Nonlinear Supersonic Potential Flow over Delta Wings," AIAA Paper 80-0269, Jan. 1980.

[11] Jameson, A., "Transonic Potential Flow Calculations using Conservation Form," *AIAA Second Computational Fluid Dynamics Conference Proceedings*, 1975, pp. 148-155.

[12] Lax, P. D., "Weak Solutions of Nonlinear Hyperbolic Equations and Their Numerical Computation," *Communications on Pure and Applied Mathematics*, Vol. 7, No. 1, 1954, pp. 159-193.

[13] Shankar, V. and Osher, S., "An Efficient Full Potential Implicit Method Based on Characteristics for Analysis of Supersonic Flow," AIAA Paper 82-0974, June 1982.

[14] Jameson, A. and Caughey, D. A., "A Finite Volume Method for Transonic Potential Flow Calculations," AIAA Paper 77-635, June 1977.

[15] Holst, T. L., "A Fast, Conservative Algorithm for Solving the Transonic-Potential Equation," AIAA Paper 79-1456, July 1979.

[16] Steger, J. L. and Caradona, F. X., "A Conservative Implicit Finite Difference Algorithm for the Unsteady Transonic Full Potential Equation," Flow Simulations, Inc. Rept. 79-04, Dec. 1979.

[17] Thompson, J. F., Thames, F. C., and Mastin, C. W., "TOMCAT—A Code for Numerical Generation of Boundary-Fitted Curvilinear Coordinate Systems on Fields Containing Any Number of Arbitrary Two-Dimensional Bodies," *Journal of Computational Physics*, Vol. 24, 1977, p. 274.

[18] Steger, J. L. and Sorenson, R. L., "Automatic Mesh-Point Clustering Near a Boundary in Grid Generation with Elliptic Partial Differential Equations," *Journal of Computational Physics*, Vol. 33, Dec. 1979, p. 405.

[19] South, J. C. and Klunker, E. B., "Method for Calculating Nonlinear Conical Flows," NASA SP-228, 1969, pp. 131-158.

[20] Jones, R. T. and Cohen, D., *High Speed Wing Theory*, Princeton University Press, Princeton, N.J., 1960, pp. 157, 160.

[21] Miller, D. S., Landrum, E. J., Townsend, J. C., and Mason, W. H., "Pressure and Force Data for a Flat Wing and a Warped Conical Wing Having a Shockless Recompression at Mach 1.62," NASA TP 1759, April 1981.

[22] Landrum, E. J., "Wind Tunnel Pressure Data at Mach Numbers from 1.6 to 4.63 for a Series of Bodies of Revolution at Angles of Attack from −4 to 60°," NASA TM X-3558, Oct. 1977.

AIAA-82-0974
An Efficient Full Potential Implicit Method Based on Characteristics for Analysis of Supersonic Flows

V. Shankar, Rockwell International Science Center, Thousand Oaks, CA;
S. Osher, Univ. of California, Los Angeles, CA .

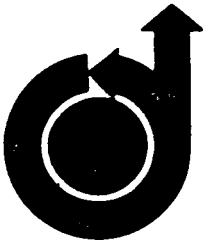

AIAA/ASME 3rd Joint Thermophysics, Fluids, Plasma and Heat Transfer Conference
June 7-11, 1982/St. Louis, Missouri

AN EFFICIENT FULL POTENTIAL IMPLICIT METHOD BASED ON CHARACTERISTICS FOR ANALYSIS OF SUPERSONIC FLOWS

Vijaya Shankar*
Rockwell International Science Center
Thousand Oaks, California 91360

Stanley Osher**
University of California
Los Angeles, California

Abstract

A nonlinear aerodynamic prediction technique based on the full potential equation in conservation form has been developed for the treatment of supersonic flows. The method uses the theory of characteristic signal propagation to accurately simulate the flow structure, which includes shock waves and mixed elliptic-hyperbolic crossflow. An implicit approximate factorization scheme is employed to solve the finite-differenced equation. The necessary body-fitted grid system in every marching plane is generated numerically, using an elliptic grid solver. Results are shown for conical and nonconical wing-body combinations and compared with experimental data and Euler calculations. The method demonstrates an enormous savings in execution time and memory requirements over Euler methods.

I. Introduction

Nonlinear aerodynamic prediction techniques based on the Euler equation[1-3] and the full potential equation[4-7] are steadily maturing into complex aerodynamic tools and becoming an attractive alternate approach to using the linearized panel methods.[8] Panel methods can handle very complicated geometries requiring minimal computer time to provide less accurate results, while the Euler solvers need expensive computer runs even for simple wing-body configurations. The full potential methods[6,7] are a substitute for the Euler methods[1,3] to avoid the requirement of excessive computer time and memory allocation. While using a full potential method for supersonic flows, one should be aware of the isentropic limitations of the theory. As a general rule, the full potential theory is expected to perform well when the product of the Mach number and the characteristic flow deflection angle is less than one ($M\delta \leq 1$).

The full potential method of Refs. 4-6 is based on the nonconservative form of the equation, while Ref. 7 and the present paper deal with the conservative form, to conserve mass across the shock.[9,10] In order to properly treat the supersonic flow structure, which includes shock waves and mixed elliptic-hyperbolic crossflow, the present method uses the theory of characteristic signal propagation based on the eigenvalue system of the full potential equation. An approximate factorization implicit scheme that includes a density biasing procedure in the crossflow plane activated by the eigenvalue system is incorporated to accelerate the computational efficiency. The implicit scheme does not pose any restrictions on the direction of sweep that are present in the successive line overrelaxation method (SLOR).[4-5]

The full potential as well as Euler methods require the application of boundary conditions at the actual body surface location. This, in general, necessitates the use of a body-fitted coordinate system. In the present method, the equation is cast in a most general arbitrary coordinate system and the appropriate body-fitted grid is generated numerically, employing an elliptic grid solver.[11]

The paper presents various results for conical and nonconical wing-body configurations and comparison is made with experimental data and Euler solution. The effect of the density biasing based on the characteristic signal propagation is demonstrated in terms of a sharper pressure profile across the shock wave. References 5 and 6 present excellent results at low supersonic Mach numbers, while Reference 7 and the present paper demonstrate the capability of the conservative full potential approach in handling even very high Mach number flows ($M_\infty \sim 4\text{-}6$, $\alpha \sim 0\text{-}8°$). All the calculations reported in this paper were performed using the CDC 7600 machine and clearly demonstrated an order of magnitude or more reduction in computer time over Euler methods. A typical nonconical wing-body calculation takes less than 2 minutes of execution time to produce results comparable with experimental data.

II. Formulation

The conservative full potential equation cast in an arbitrary coordinate system defined by, $\zeta = \zeta(x,y,z)$, $\eta = \eta(x,y,z)$, and $\xi = \xi(x,y,z)$, takes the form

$$\left(\rho \frac{U}{J}\right)_\zeta + \left(\rho \frac{V}{J}\right)_\eta + \left(\rho \frac{W}{J}\right)_\xi = 0 , \quad (1)$$

where U, V, and W are the contravariant velocity components. Introducing the following notation for convenience

$$U = U_1 \quad , \quad V = U_2 \quad , \quad W = U_3$$

$$x = x_1 \quad , \quad y = x_2 \quad , \quad z = x_3$$

$$\zeta = X_1 \quad , \quad \eta = X_2 \quad , \quad \xi = X_3$$

the contravariant velocities and density are given by

*Member Technical Staff, Associate Fellow AIAA

**Professor, Department of Mathematics

$$\left.\begin{aligned} U_i &= \sum_{j=1}^{3} a_{ij}\phi_{X_j} \qquad i = 1,2,3 \\ a_{ij} &= \sum_{k=1}^{3} \frac{\partial X_i}{\partial x_k}\frac{\partial X_j}{\partial x_k} \qquad \begin{matrix} i = 1,2,3 \\ j = 1,2,3 \end{matrix} \\ \rho &= \left[1 - \left(\frac{\gamma-1}{2}\right) M_\infty^2 \left\{ U\phi_\zeta + V\phi_\eta + W\phi_\xi - 1 \right\}\right]^{1/(\gamma-1)} \end{aligned}\right\} \quad (2)$$

The Jacobian of the transformation J is represented by

$$J = \frac{\partial(\zeta,\eta,\xi)}{\partial(x,y,z)} = \begin{bmatrix} \zeta_x & \zeta_y & \zeta_z \\ \eta_x & \eta_y & \eta_z \\ \xi_x & \xi_y & \xi_z \end{bmatrix}. \quad (3)$$

Equation (1) is in terms of a general coordinate system (ζ,η,ξ) and can accommodate any kind of mapping procedure, either analytical (conformal mapping) or numerical type. Use of Eq. (1) to simulate the supersonic flow by marching in the ζ direction, first requires the establishment that the equation is indeed hyperbolic with respect to the marching direction. The nature of Eq. (1) can be analyzed by studying the eigenvalue system of Eq. (1). Combining the irrotationality condition in the (ζ,η) and (ζ,ξ) plane and Eq. (1), one can write the following matrix equation.

$$Aq_\zeta + Bq_\eta + Cq_\xi = 0 \quad (4)$$

where

$$A = \begin{bmatrix} \frac{1}{J}(\rho U)_{\phi_\zeta} & \frac{1}{J}(\rho U)_{\phi_\eta} & \frac{1}{J}(\rho U)_{\phi_\xi} \\ 0 & 1 & 0 \\ 0 & 0 & 1 \end{bmatrix}$$

$$B = \begin{bmatrix} \frac{1}{J}(\rho V)_{\phi_\zeta} & \frac{1}{J}(\rho V)_{\phi_\eta} & \frac{1}{J}(\rho W)_{\phi_\xi} \\ -1 & 0 & 0 \\ 0 & 0 & 0 \end{bmatrix}$$

$$C = \begin{bmatrix} \frac{1}{J}(\rho W)_{\phi_\zeta} & \frac{1}{J}(\rho W)_{\phi_\eta} & \frac{1}{J}(\rho W)_{\phi_\xi} \\ 0 & 0 & 0 \\ -1 & 0 & 0 \end{bmatrix}$$

$$q = \begin{pmatrix} \phi_\zeta \\ \phi_\eta \\ \phi_\xi \end{pmatrix}$$

The subscripts in Eq. (4) denote differentiation with respect to that variable.

In order for Eq. (4) or Eq. (1) to be hyperbolic in ζ direction the following two conditions must be satisfied.

(1) A^{-1} must exist

(2) All real linear combinations of $A^{-1}B$ and $A^{-1}C$ must have real eigenvalues (characteristics). This implies $A^{-1}(\alpha B + \beta C)$ must have real eigenvalues for all combinations of α and β satisfying $\alpha^2 + \beta^2 = 1$.

When the above two conditions are applied to Eq. (4), the following criteria is obtained for ζ to be the marching direction.

$$(\rho U)_{\phi_\zeta} = \rho\left(a_{11} - \frac{U^2}{a^2}\right) < 0 \quad (5)$$

Where the transformation metric a_{11} is defined in Eq. (2) and a is the local speed of sound. Equation (5) is the most general form. For example, in a spherical system (r,θ,ϕ), for the radial direction r to be the marching direction, according to Eq. (5), the radial velocity q_r must be supersonic. In a Cartesian system (x,y,z), for x to be the marching direction, the velocity u has to be supersonic. For convenience, the derivation of Eq. (5) for a Cartesian system is described in Appendix A, and the derivation for an arbitrary coordinate system (ζ,η,ξ) has been derived in a similar manner.

Thus far, the condition for ζ to be a marching direction has been identified from the characteristic theory. Thes means the (η,ξ) plane will be treated as a marching plane, which will be defined from now on in this paper as the crossflow plane (the real crossflow is the projection of the velocity vector on a unit sphere with center at the origin). Even though, the flow is supersonic in the marching direction (i.e., hyperbolic type), the behavior of the flow structure in the crossflow plane (η,ξ) can be a mixed elliptic-hyperbolic type. Depending on the nature of the flow at a crossflow plane grid point (whether elliptic, parabolic or hyperbolic), the η and ξ derivative terms in Eq. (1) will be appropriately modeled. Again, the theory of characteristics will dictate how the signals are propagated in the crossflow plane.

A. Crossflow Signal Propagation

The nature of the flow in the (η,ξ) plane can be analyzed by separately studying the eigenvalues of $A^{-1}B$ and $A^{-1}C$. The eigenvalue character of $A^{-1}B$ will determine the η- derivative treatment and similarly $A^{-1}C$ for the ξ derivative. For illustration, only the study of $A^{-1}B$ is shown here, and $A^{-1}C$ follows the same procedure.

The eigenvalues λ of $A^{-1}B$ are obtained by solving $(A^{-1}B - \lambda I) = 0$. Since A^{-1} is assumed to exist (condition (1) before Eq. (5)), the following is true.

$$B - \lambda A = \begin{bmatrix} \left\{\frac{1}{J}(\rho V)_{\phi_\zeta} - \frac{\lambda}{J}(\rho U)_{\phi_\zeta}\right\} & \left\{\frac{1}{J}(\rho V)_{\phi_\eta} - \frac{\lambda}{J}(\rho U)_{\phi_\eta}\right\} & \left\{\frac{1}{J}(\rho V)_{\phi_\xi} - \frac{\lambda}{J}(\rho U)_{\phi_\xi}\right\} \\ -1 & -\lambda & 0 \\ 0 & 0 & -\lambda \end{bmatrix} = 0 \quad (6)$$

Solving for λ,

$$\lambda_{1,2} = \frac{\left\{(\rho U)_{\phi_\eta} + (\rho V)_{\phi_\zeta}\right\} \pm \sqrt{\left\{(\rho U)_{\phi_\eta} + (\rho V)_{\phi_\zeta}\right\}^2 - 4(\rho U)_{\phi_\zeta}(\rho V)_{\phi_\eta}}}{2(\rho U)_{\phi_\zeta}} \quad (7)$$

Now, analyzing λ_1 and λ_2 the following combinations are possible.

(1) λ_1 is positive (or) λ_1 is negative
    λ_2 is negative λ_2 is positive
(2) λ_1 and λ_2 both positive
(3) λ_1 and λ_2 both negative
(4) λ_1 or λ_2 is zero

These possible combinations are schematically shown in Fig. (1). Each one of these combinations describe a different feature of the flow in the crossflow direction η. Referring to Fig. (1) diagram the following descriptions are made.

Case 1

Here, one eigenvalue is positive and one negative This implies an elliptic type crossflow because the characteristic signals are brought into the point P from both the positive and negative direction of η.

Case 2

Here, both the characteristics are positive, which means the characteristic signals propagate into the point P only from below and anything happening above the point P doesn't influence that point. This describes a hyperbolic type crossflow point with a positive contravariant velocity V.

Case 3

Here, the characteristic signals propagate from above into the point P and similar to case 2, this describes a hyperbolic type crossflow with a negative contravariant velocity V.

Case 4

Here, one of the eigenvalues is zero and describes a parabolic type crossflow. This will represent the crossflow sonic line.

The transition from an elliptic to a hyperbolic crossflow type takes place through a parabolic point, which is indicated by one of the eigenvalues going to zero. Thus, by monitoring the eigenvalues λ_1 and λ_2 one can precisely model the crossflow plane terms. Depending on whether it is elliptic or hyperbolic, appropriate finite difference models for the η derivative term in Eq. (1) are chosen. This will be described later in this paper.

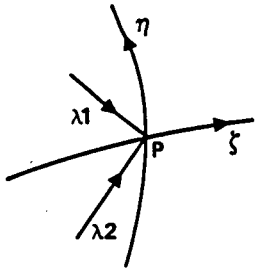

CASE 1. ELLIPTIC CROSSFLOW

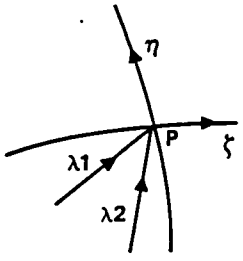

CASE 2. HYPERBOLIC CROSSFLOW POSITIVE V

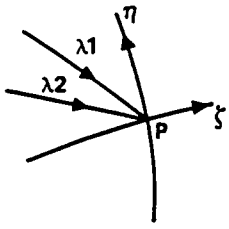

CASE 3. HYPERBOLIC CROSSFLOW NEGATIVE V

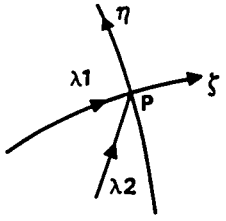

CASE 4. PARABOLIC CROSSFLOW

Fig. 1. Eigenvalue structure in (ζ,η) plane.

One can readily see from Eq. (7), that one of the eigenvalues go to zero when

$$(\rho V)_{\phi_\eta} = 0 \quad (8)$$

From the definition of ρ and V from Eq. (2), one can write

$$(\rho V)_{\phi_\eta} = \rho\left\{a_{22} - \frac{V^2}{a^2}\right\} \quad (9)$$

Thus, when $a_{22} = \frac{V^2}{a^2}$ occurs, the method will anticipate a switch in the character of the crossflow, and realize the onset of the formation of a supercritical crossflow.

Besides providing a valuable information regarding the type of crossflow, the eigenvalues λ_1 and λ_2 of $A^{-1}B$ and similarly λ_3 and λ_4 of $A^{-1}C$ can also be used to determine the Courant number in η and ξ direction for a given step size $\Delta\zeta$.

$(\lambda max)_\eta \frac{\Delta\zeta}{\Delta\eta}$ = Courant Number in η direction.

$(\lambda max)_\xi \frac{\Delta\zeta}{\Delta\xi}$ = Courant Number in ξ direction.

Where $(\lambda max)_\eta$ and $(\lambda max)_\xi$ define the maximum of (λ_1,λ_2) and (λ_3,λ_4) respectively.

B. Treatment of $\left(\rho\frac{U}{J}\right)_\zeta$ in Eq. (1)

The direction ζ has been identified to be the hyperbolic marching direction satisfying the condition given by Eq. (5). Referring to Fig. (2), this derivative term will be backward differenced as,

$$\left(\rho\frac{U}{J}\right)_\zeta = \frac{(a_1 - \theta b_1)\left\{\left(\rho\frac{U}{J}\right)_{i+1} - \left(\rho\frac{U}{J}\right)_i\right\} - \theta b_1\left\{\left(\rho\frac{U}{J}\right)_i - \left(\rho\frac{U}{J}\right)_{i-1}\right\}}{a_1\Delta\zeta_1 - \theta b_1(\Delta\zeta_1 + \Delta\zeta_2)} \quad (10)$$

where

$$a_1 = (\Delta\zeta_1 + \Delta\zeta_2)^2$$

$$b_1 = (\Delta\zeta_1)^2$$

θ = 0 first order accurate

= 1 second order accurate

Given the velocity potential ϕ information at all previous planes i, i-1, i-2, ..., the problem is to compute ϕ at the current plane i+1. Equation (10) involves both the density and contravariant velocity at the (i+1) plane, and both are functions of ϕ (Eq. 1). In order to write Eq. (10) in terms of ϕ only will require a local linearization procedure. This is done as follows:

$$(\rho U)_{i+1} \doteq (\rho U)_i + \left[(\rho U)_\phi\right]_i \Delta\phi + \ldots \quad (11)$$

where

$$(\rho U)_\phi = \rho_\phi U + \rho U_\phi$$

$$\Delta\phi = \phi_{i+1} - \phi_i$$

Substituting for ρ_ϕ and U_ϕ into Eq. (11), and grouping various terms,

$$(\rho U)_{i+1} \doteq \rho_i\left[\left(a_{11} - \frac{U^2}{a^2}\right)_i \frac{\partial(\Delta\phi)}{\partial\zeta} + \left(a_{12} - \frac{UV}{a^2}\right)_i \frac{\partial(\Delta\phi)}{\partial\eta} + \left(a_{13} - \frac{UW}{a^2}\right)_i \frac{\partial(\Delta\phi)}{\partial\xi} + U_i\right] \quad (12)$$

The above locally linearized equation involves only $\Delta\phi$ as the unknown to be solved for. To maintain the conservative differencing, both $(\rho U)_{i+1}$ and $(\rho U)_i$ appearing in the first term of Eq. (10) will be linearized. That is, $(\rho U)_i$ will be linearized about (i-1) plane values. The upwind differencing of the ζ derivative term as shown in Eq. (10) will produce a truncation term whose leading term is $\left\{1 - \frac{a^2 a_{11}}{U^2}\right\} U^2\phi_{\zeta\zeta\zeta}\,\Delta\zeta$. This will always represent a positive artificial viscosity as long as the marching condition dictated by the characteristic theory, Eq. (5), is satisfied.

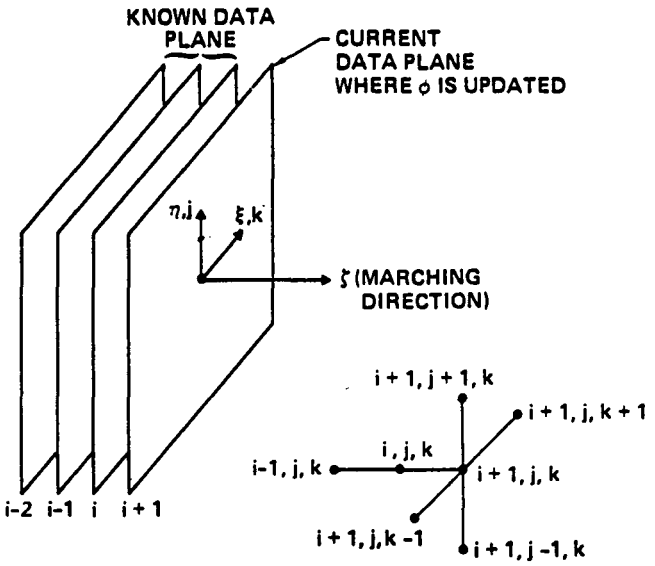

Fig. 2. Implicit computational molecule

C. Treatment of the Crossflow Term $\left(\rho\frac{V}{J}\right)_\eta$ in Eq. (1)

Similar to the treatment of the (ρU) term, the $(\rho V)_{i+1}$ will also be linearized as,

$$(\rho V)_{i+1} = (\rho V)_i + \left[(\rho V)_\phi\right]_i \Delta\phi + \ldots \quad (13)$$

$$= \rho_i\left[\left(a_{21} - \frac{UV}{a^2}\right)_i \frac{\partial\Delta\phi}{\partial\zeta} + \left(a_{22} - \frac{V^2}{a^2}\right)_i \frac{\partial\Delta\phi}{\partial\eta} + \left(a_{23} - \frac{VW}{a^2}\right)_i \frac{\partial\Delta\phi}{\partial\xi} + V_i\right]$$

The above linearized expression for $(\rho V)_{i+1}$ will be plugged inside the η derivative term of Eq. (1). It involves only $\Delta\phi$ as the unknown variable. The finite difference model for the $\left(\rho\frac{V}{J}\right)_\eta$ term will be dictated by the theory of characteristic signal propagation as described in Section A of this paper. When the eigenvalues of $A^{-1}B$ represent case 1 in Fig. 1 (one positive and one negative eigenvalue representing an elliptic type), then all the terms in $\left(\rho\frac{V}{J}\right)_\eta$ will be central differenced. For this case, $\left(a_{22} - \frac{V^2}{a^2}\right)$ is positive, and central differencing of the $\left(\rho\frac{V}{J}\right)_\eta$ term along with the backward differencing of the $\left(\rho\frac{U}{J}\right)_\zeta$ term as in Eq. (10) will preserve the diagonal dominance. For cases 2 and 3 of Fig. 1, the crossflow behaves like hyperbolic type, and $\left(a_{22} - \frac{V^2}{a^2}\right)$ is negative. Then, central differencing of the terms in Eq. (13) is inappropriate, as it will destroy the diagonal dominance, and also will not provide the necessary artificial viscosity to avoid the formation of expansion shocks. Thus, when λ_1 and λ_2 are both positive or

both negative (hyperbolic type), the terms in $\left(\rho\frac{V}{J}\right)_\eta$ should be upwind differenced depending on the direction of V. However, such an upwind differencing in the η direction will not give rise to a tridiagonal system, and in general, the overall system will be pentadiagonal in nature. In order to preserve the tridiagonal nature of the implicit scheme, rather than upwind differencing the ϕ derivatives, the density biasing concept[7,12] is implemented when the crossflow is hyperbolic.

The procedure is as follows:

$$\left(\rho\frac{V}{J}\right)_\eta \doteq \frac{\partial}{\partial\eta}\left\{\frac{\tilde{\rho}}{J}\left(a_{21}\phi_\zeta + a_{22}\phi_\eta + a_{23}\phi_\xi\right)\right\} \qquad (14)$$

Here, the density ρ has been replaced by $\tilde{\rho}$ defined to be (referring to Fig. 2)

$$\tilde{\rho}_{i+1,j+\frac{1}{2},k} = \left(1 - \nu_{j+\frac{1}{2},k}\right)\rho^*_{j+\frac{1}{2},k} + \frac{1}{2}\nu_{j+\frac{1}{2},k}$$

$$\left\{(1+\theta)\,\rho^*_{j+2m,k} + (1-\theta)\,\rho^*_{j-1+2m,k}\right\} \qquad (15)$$

where m=0 when $\left(V_0\right)_{j+\frac{1}{2},k} > 0$, = +1 when $\left(V_0\right)_{j+\frac{1}{2},k} < 0$. When θ is set to zero, first order accurate density biasing is achieved while θ=2 gives second order accuracy. The artificial viscosity coefficient $\nu_{j+\frac{1}{2},k}$ is computed as follows:

$$\nu_{j+\frac{1}{2},k} = \mu\left(1 - \frac{a^2}{q^2}\right)_{i,j+s,k} \qquad (16)$$

where, q is the local total velocity, a is the speed of sound and

$$s=0 \text{ for } V_{j+\frac{1}{2},k} > 0$$

$$=1 \text{ for } V_{j+\frac{1}{2},k} < 0$$

$$\mu=0 \text{ for } \left(a_{22} - \frac{V^2}{a^2}\right)_{i,j+\frac{1}{2},k} > 0 \text{ (elliptic crossflow)}$$

$$=1 \text{ for } \left(a_{22} - \frac{V^2}{a^2}\right)_{i,j+\frac{1}{2},k} < 0 \text{ (hyperbolic crossflow)}$$

Thus, the density biasing is switched off when the eigenvalues λ_1 and λ_2 exhibit an elliptic crossflow. All the ϕ derivative terms are central differenced in Eq. (14). Treatment of the density as represented by Eqs. (15) and (16) would always produce a positive artifical viscosity when the crossflow is hyperbolic. The local total velocity is always assumed to be greater than the speed of sound, otherwise the marching procedure would fail.

In Eq. (15), the evaluation of ρ^* depends on whether the flow is conical or nonconical. For conical flows all ρ^* quantities are evaluated at the i-th plane. For nonconical flows, at each nonconical marching plane, initially ρ^* is set to be the value at the i-th plane and then subsequently iterated to convergence by setting ρ^* to the previous iterated value of ρ at the current i+1 plane.

A similar density biasing procedure is implemented for the $\left(\rho\frac{W}{J}\right)_\xi$ term in Eq. (1). Activating the density biasing based on the eigenvalue structure of $A^{-1}B$ and $A^{-1}C$ has proved to be very efficient in predicting sharp shock profiles The same concept can also be employed for transonic applications.

Combining the various terms of Eq. (1) as represented by Eqs. (10), (14) and (15) together with the terms arising from $\left(\rho\frac{W}{J}\right)_\xi$ will result in a fully implicit model. This is solved using an approximate factorization implicit scheme. The details are given in Ref. 7. The boundary condition at the body surface is the flow tangency condition, which is easily applied by setting the contravariant velocity V to zero at all body points.

III. Grid System

The transformation of the physical space (x,y,z) to a body-fitted computational space (ζ,η,ξ) is performed numerically by using the elliptic grid generation technique of Ref. 11. The body geometry at every marching plane is prescribed along with a suitable outer boundary where free stream conditions are imposed. Since the equation is cast in a general coordinate system, the marching plane (constant ζ) can either be a constant x plane or a spherical (constant r) plane as long as the marching criteria (Eq. 5) is satisfied. Given the geometry shape and the prescribed outer boundary, the following set of elliptic equations are solved to generate the interior grid.

$$\xi_{yy} + \xi_{zz} = P(\xi,\eta)$$

$$\eta_{yy} + \eta_{zz} = Q(\xi,\eta) \qquad (17)$$

The forcing terms P and Q are properly chosen to achieve two main desirable features: (1) to cluster grid points to a boundary, and (2) to force grid lines to intersect the boundary in a nearly orthogonal fashion.

Once the grid is generated, all the metric terms a_{ij} in Eq. (2) and the Jacobian J in Eq. (3) are computed by numerical differentiation. To subtract out any numerical truncation error in the free stream due to incomplete metric cancellation,[13] it is essential to add the terms (especially for a highly stretched nonorthogonal grid).

$$\frac{\partial}{\partial\zeta}\left(\frac{\rho_\infty U_\infty}{J}\right) + \frac{\partial}{\partial\eta}\left(\frac{\rho_\infty V_\infty}{J}\right) + \frac{\partial}{\partial\xi}\left(\frac{\rho_\infty W_\infty}{J}\right) \qquad (18)$$

to the right hand side of the finite differenced model of Eq. (1).

IV. Results

A series of calculations were performed for conical and nonconical geometries at various Mach numbers ($M_\infty \sim 2$ to 6) and angles of attack ($\alpha \sim 0$ to $10°$), to validate the full potential characteristic switch methodology, and assess the feasibility of using numerical grid solvers for complex configurations. The results from this study are compared with experimental data and Euler simulation.

The generality of the formulation allows one to choose any ζ as the marching direction, provided the condition given by Eq. (5) is satisfied. Thus, depending on the geometry definition and the flowfield character one could choose either a constant x-plane marching or constant r-plane spherical marching.

The effect of on, off density biasing based on characteristic signals in the crossflow plane (η,ξ), described by Eq. (16), is demonstrated in terms of the crossflow Mach number (M_{CF}) distribution in the shock region in Fig. 3. When density biasing is applied everywhere[7], including at elliptic crossflow points, it introduces unnecessary artificial viscosity and tends to smear the discontinuities like shocks in the flow field. This is seen by the dash line crossflow Mach number distribution across the bow shock and across the embedded shock on a cone surface in Fig. 3. When the density biasing is switched off at crossflow elliptic points, the shocks appear as a sharper discontinuity (usually within two mesh intervals) as shown by the solid line distribution in Fig. 3. All the calculations to be presented here, were achieved using the second order accurate implicit scheme (θ=1 in Eq. 10), with on,off density biasing activator μ in Eq. 16.

Figure 4 shows the grid arrangement in the marching plane for a conically cambered wing-body combination. The elliptic grid solver with orthogonality constraints near the surface, required 40 to 60 iterations to converge to within 10^{-8} error in the residual. Figure 5 shows the pressure distribution at $M_\infty = 2$ and angles of attack of 7.81° and 10.82°. The leading edge sweep is moderate (57°), and spherical plane marching is implemented (instead of x-plane marching) to avoid low supersonic Mach number components along x-direction near the leading edge. The results are compared with experimental data given in Ref. 14. The comparison is excellent. The marching step size $\Delta\zeta$ is chosen by monitoring the eigenvalues and setting the Courant number to about 20. The numerical formulation, being a conservative form, predicts a stronger crossflow recompression on the leeward side than the ones seen in experiments. On a 20 x 49 (η,ξ) grid, the method requires about a minute of CDC 7600 time. The conical flow field is assumed to have converged when the change in root mean square density in the marching plane is reduced to less than 10^{-5}.

Figure 6 shows the surface pressure distribution on a flat conical wing-body (that is not designed to weaken the crossflow shock formation) at two different angles of attack (1.72° and 5.71°) and Mach number of 2. The experimental data and the numerical prediction are in excellent agreement and clearly indicate the presence of an embedded crossflow shock.

Even though the full potential theory is restricted by the isentropic assumption, one will be surprised to find out that the theory can be effectively utilized to predict even very high Mach number flows as long as $M\delta$ is less than or of the order of one ($M\delta \leq 1$). This is demonstrated in Fig. 7, which shows the results for a Sears-Haack body at $M_\infty = 6$ and different angles of attach (0°, 4°, 8°). The numerical prediction is compared with an unpublished NASA Langley data, and the agreement is excellent. Constant x-plane marching is implemented for this configuration.

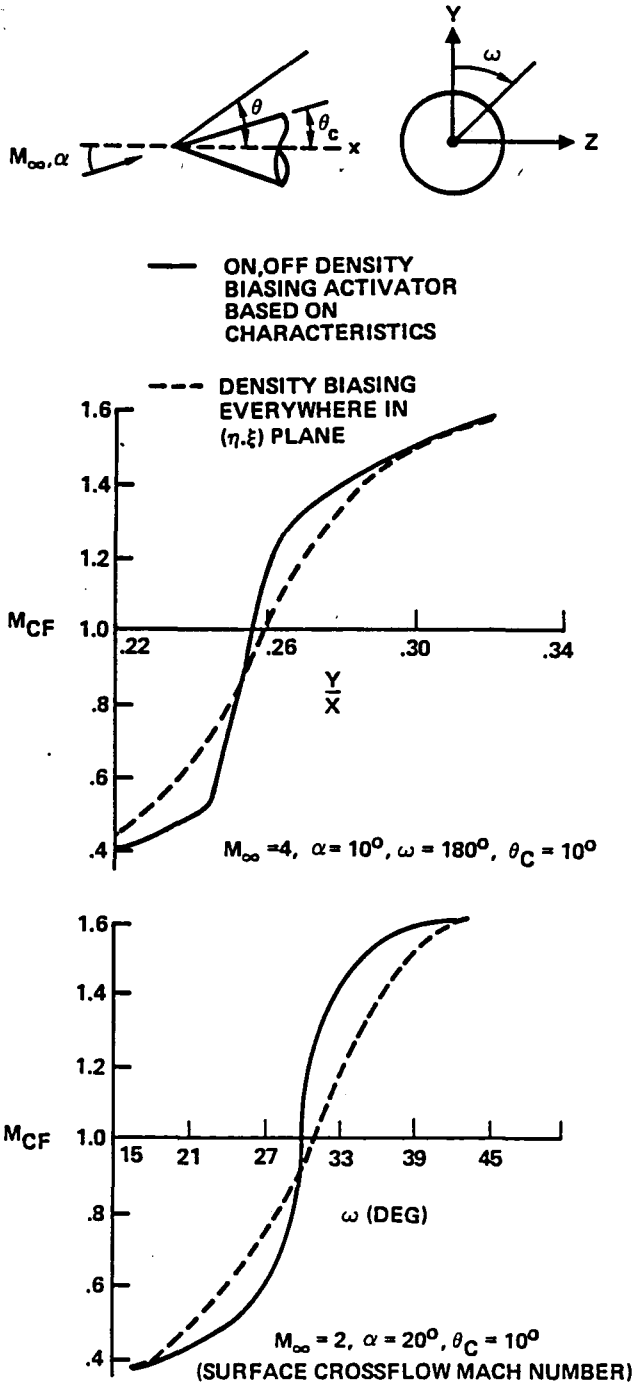

Fig. 3. Effect of density biasing activator on the crossflow Mach number distribution in the shock region

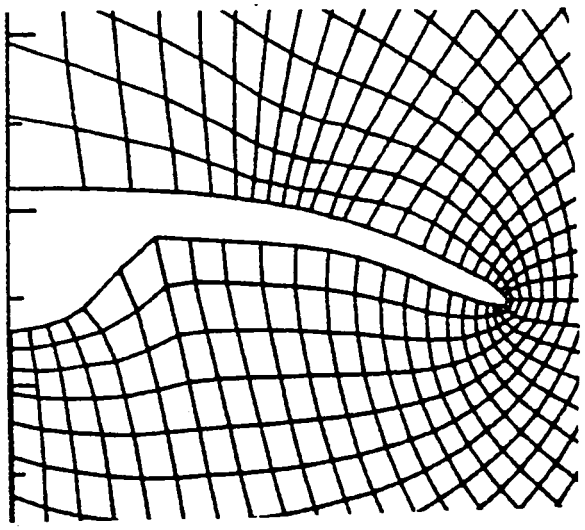

Fig. 4. Grid arrangement in the marching plane for a conically cambered wing-body combination

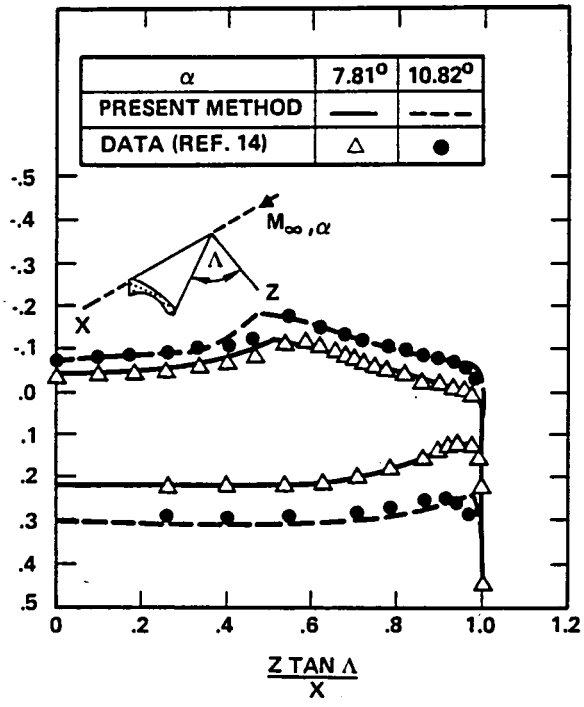

Fig. 5. Surface pressure distribution on a conically cambered wing-body combination $M_\infty = 2$

Figure 8 shows a schematic of a symmetric arrow wing-body configuration. The actual geometry shape is prescribed analytically as detailed in Ref. 15. Series of computer runs were made for this configuration at different Mach numbers and angles of attach and some results are presented here. First, an initial data plane near the nose region of the configuration is established by assuming a conical nose shape. The nonconical marching is then initiated. At each nonconical marching plane, the density is iterated to convergence (ρ^* in Eq. 15 usually takes 2 to 3 cycles, to converge to 10^{-5} error tolerance) before proceeding to the next marching plane. The grid at each marching plane is generated using the elliptic grid solver. Figures 9a to 9d show series of results at x/ℓ of 0.3, 0.5, 0.65 and 0.8 respectively. The full potential results are compared with the experimental data and Euler simulation in Ref. 15. Figure 9a, which

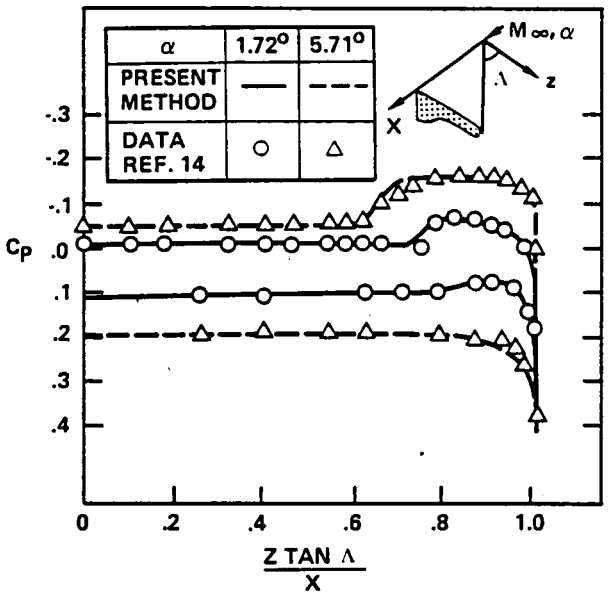

Fig. 6. Surface pressure distribution on a flat conical wing-body combination $M_\infty = 2$

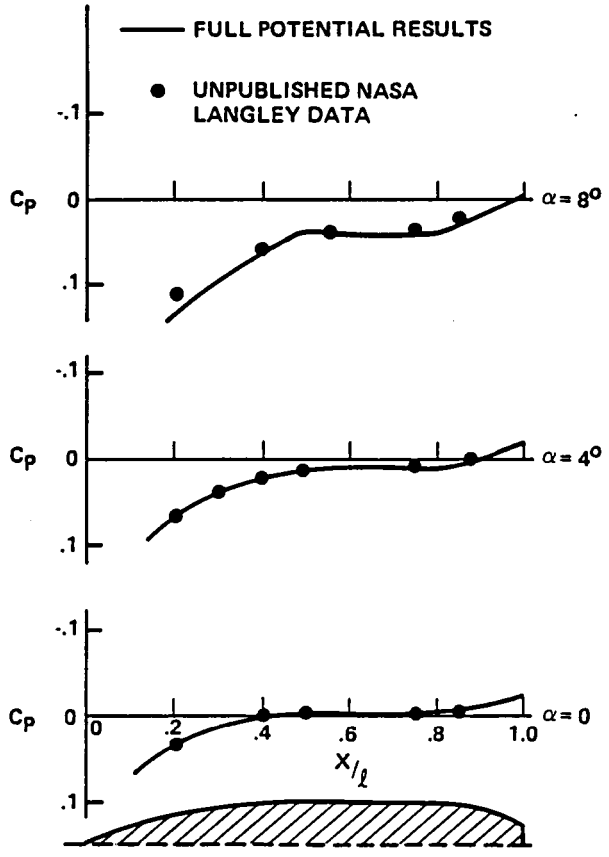

Fig. 7. Pressure distribution on Sears-Haack body at $M_\infty = 6$. Windward plane of symmetry.

shows results for x/ℓ of 0.3, clearly demonstrates the accuracy of the full potential simulation. It is surprising to see that the present full potential method compares with the experimental data even better than the Euler calculation even at a high Mach number of 4.63. Similar excellent full potential results are shown in Fig. 9b for x/ℓ of 0.5 and compared with data from Ref. 15. The striking full potential results are shown in Fig. 9c, where the unphysical oscillations experienced by the Euler simulation at M_∞ = 2.36 near the wing-body junction area are not seen in the present method and comparison with experimental data is more dramatic. Figure 9d shows the pressure distribution at x/ℓ of 0.8, where the wing is separated from the body. The wake is simulated by assuming a planar shape, and imposing pressure equality (in the present method, it will be density equality due to full potential formulation) across the cut. Again, the full potential results are in good agreement with the Euler solution and experimental data.

Figure 10 shows an angle of attack case, M_∞ = 4.63, α = 3° for the same symmetric arrow wing-body configuration. The results are compared with the data of Ref. 15 at x/ℓ of 0.65, and the agreement is good even near the wing body function region.

A typical arrow wing-body calculation using a 20 x 49 grid in the (η,ξ) plane and choosing a marching step size Courant number of 3, required 2 minutes of CPU time for the entire calculation, which includes the numerical grid generation at each plane and the conical initial data plane. This represents an enormous savings in computer execution cost over other nonlinear methods, especially Euler solvers.

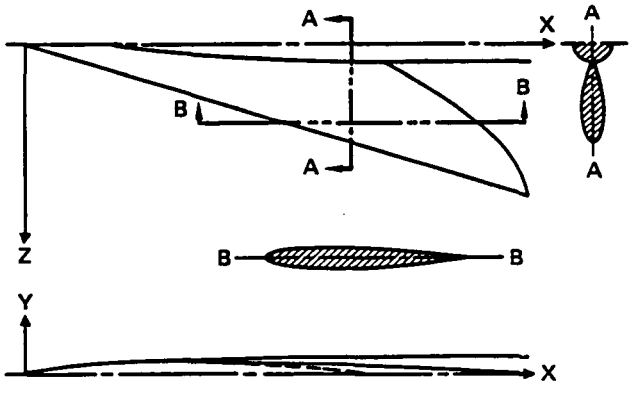

Fig. 8. Top and side views of a typical arrow wing-body configuration

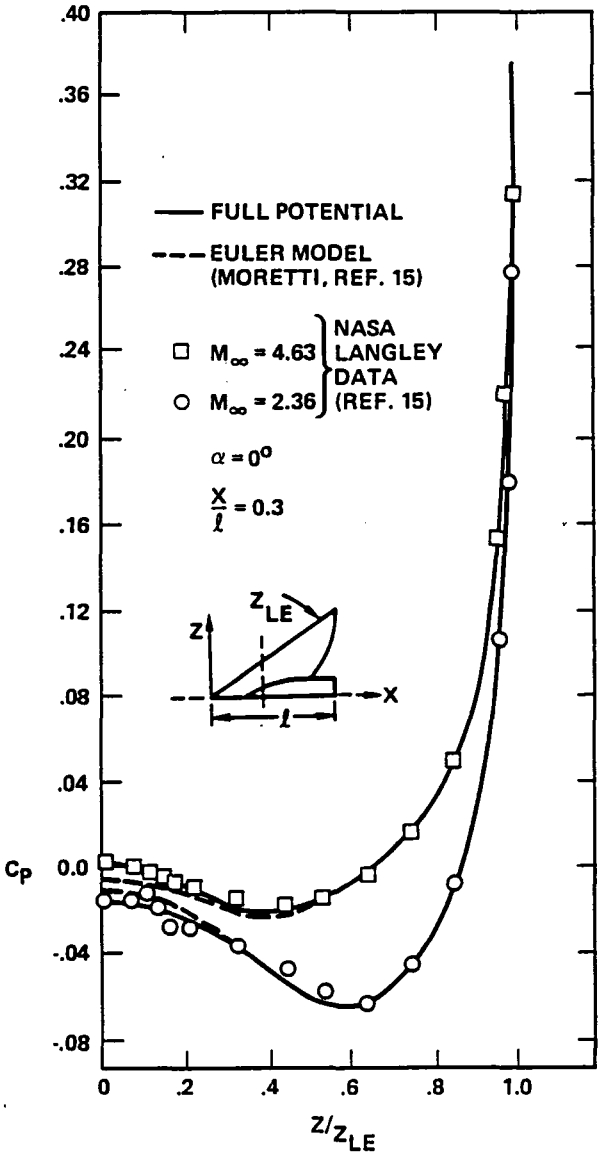

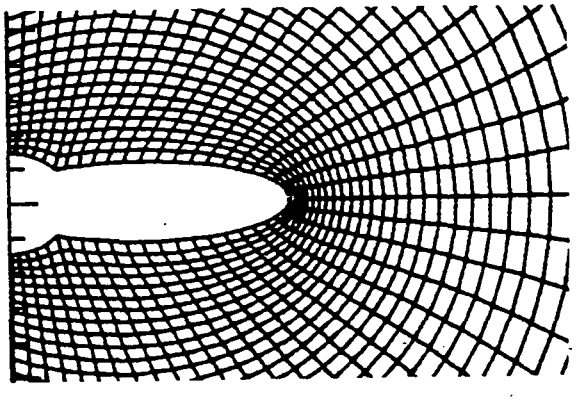

Fig. 9a. Grid arrangement and surface pressure distribution for a symmetric arrow wing at x/ℓ = 0.3

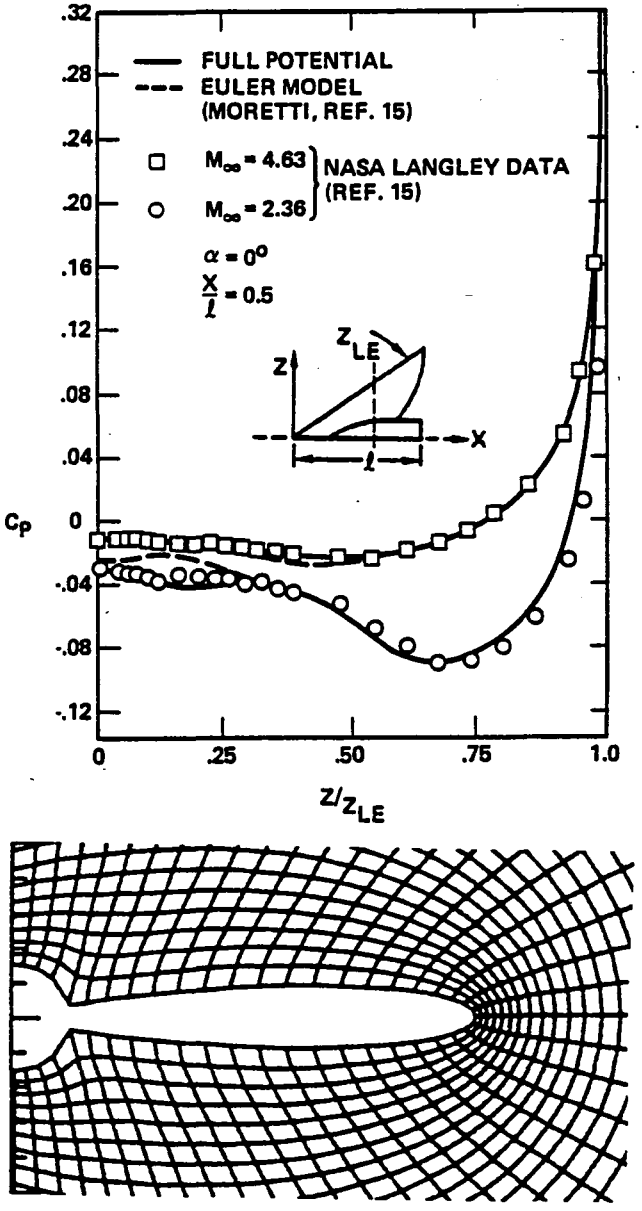

Fig. 9b. Arrow wing pressure distribution at $x/\ell = 0.5$

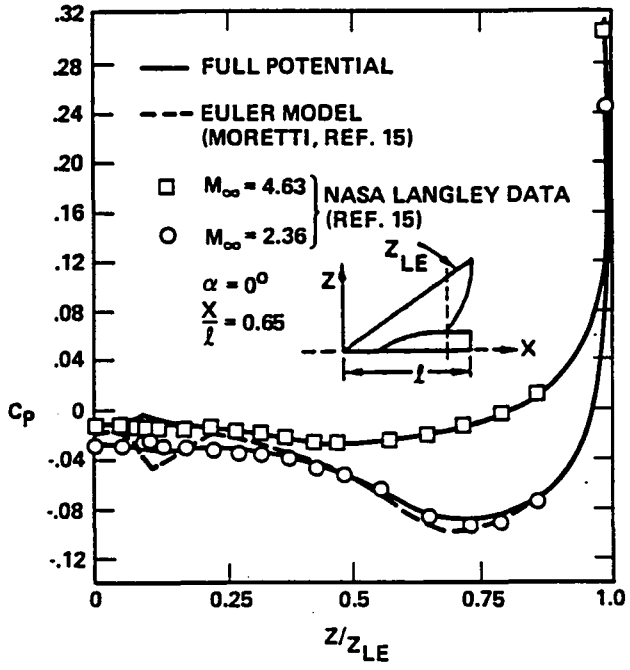

Fig. 9c. Arrow wing pressure distribution at $x/\ell = 0.65$

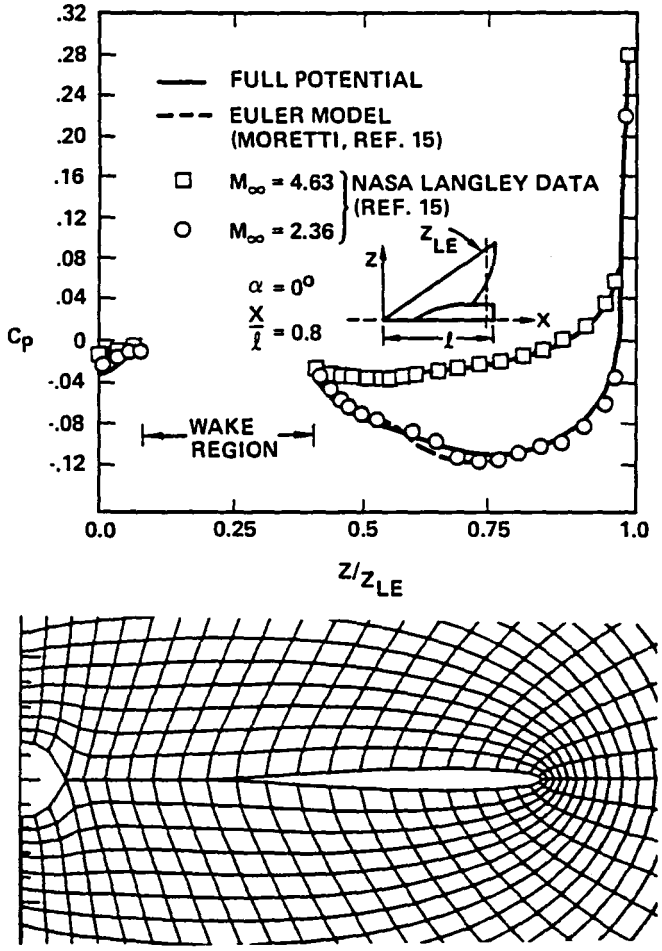

Fig. 9d. Arrow wing pressure distribution at $x/\ell = 0.8$

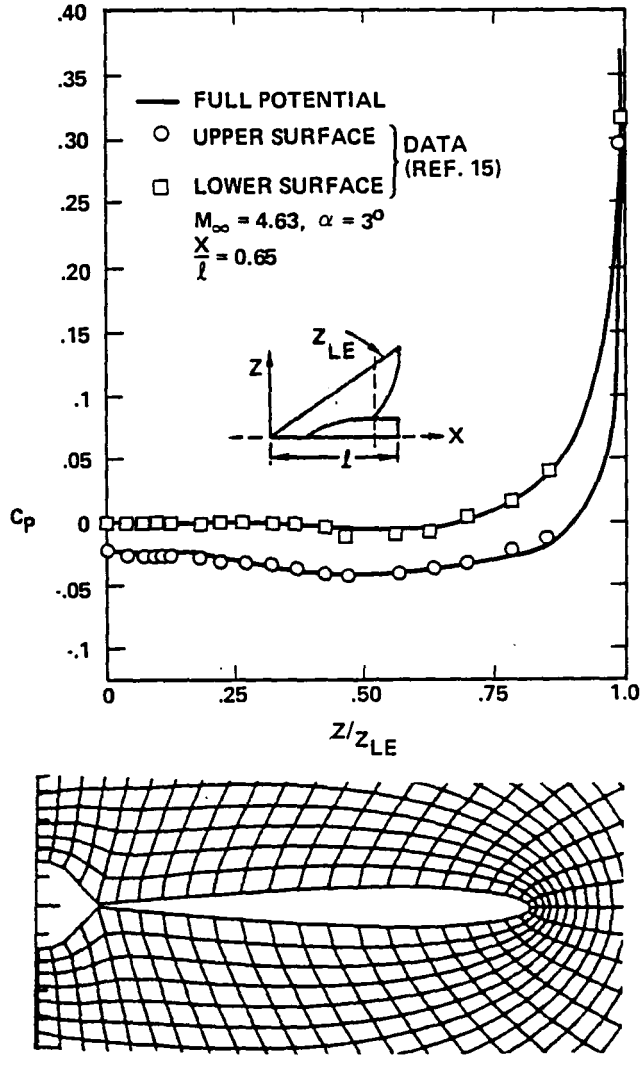

Fig. 10. Angle of attack solution for the arrow wing at $x/\ell = 0.65$

V. Conclusions

A nonlinear full potential aerodynamic prediction capability based on a sound mathematical theory of characteristic signal propagation has been developed. The method uses a general body-fitted coordinated system and numerical mapping techniques. The on, off density biasing activator in the crossflow plane has proved to be very effective in capturing sharp shock profiles. Results for conical and nonconical flows at various Mach numbers and angles of attach are shown to be in excellent agreement with experimental data and Euler results. The enormous savings in computational cost exhibited by the present approach, makes it a very promising substitute for the less accurate linearized panel methods, and expensive Euler solvers for use as a preliminary design tool. The future work will involve automatic grid generation for wing-body-nacelle-canard configurations and better wake treatment.

Appendix A

Derivation of the marching condition (Eq. 5) for a Cartesian system

The Cartesian system analog of Eq. (4) is given by

$$Af_x + Bf_y + Cf_z = 0 \qquad \text{(A1)}$$

where,

$$A = \begin{bmatrix} (\rho u)_u & (\rho u)_v & (\rho u)_w \\ 0 & 1 & 0 \\ 0 & 0 & 1 \end{bmatrix}$$

$$B = \begin{bmatrix} (\rho v)_u & (\rho v)_v & (\rho v)_w \\ -1 & 0 & 0 \\ 0 & 0 & 0 \end{bmatrix}$$

$$C = \begin{bmatrix} (\rho w)_u & (\rho w)_v & (\rho w)_w \\ 0 & 0 & 0 \\ -1 & 0 & 0 \end{bmatrix}$$

$$f = \begin{pmatrix} u \\ v \\ w \end{pmatrix}$$

Equation (A1) is hyperbolic with respect to x-direction if

1) A^{-1} exist

2) $A^{-1}(\alpha B + \beta C)$ must have real eigenvalues for all α and β satisfying $\alpha^2 + \beta^2 = 1$

Since A^{-1} is assumed to exist, the eigenvalues of $A^{-1}(\alpha B + \beta C)$ can be obtained by solving

$$(\alpha B + \beta C - \lambda A) = 0 \qquad \text{(A2)}$$

Substituting for A, B and C from Eq. (A1) into Eq. (A2), the roots of the equation are obtained.

$$\lambda_{1,2} = \frac{-\frac{u}{a^2}(v\alpha+w\beta) \pm \sqrt{\frac{u^2}{a^4}(v\alpha+w\beta)^2 - \left(1-\frac{u^2}{a^2}\right)\left\{1-\frac{(v\alpha+w\beta)^2}{a^2}\right\}}}{1-\frac{u^2}{a^2}} \qquad \text{(A3)}$$

Eq. (A3) will have real values as long as the square root term is real. This implies, the quantity inside the square root must be positive. Simplifying the quantity inside the square root, the condition becomes

$$\frac{u^2 + (v\alpha + w\beta)^2}{a^2} - 1 > 0 \qquad \text{(A4)}$$

Let

$$\left.\begin{aligned} \alpha &= \cos\theta \\ \beta &= \sin\theta \end{aligned}\right\} \Rightarrow \alpha^2 + \beta^2 = 1$$

$$v = \bar{q}\cos\bar{\theta}$$

$$w = \bar{q}\sin\bar{\theta}$$

where,

$$\bar{q} = \sqrt{v^2 + w^2}$$

$$\tan\bar{\theta} = w/v.$$

Substituting these into Eq. (A4) and simplifying results in

$$\frac{u^2 + \bar{q}^2\cos^2(\bar{\theta} - \theta)}{a^2} - 1 > 0 \qquad \text{(A5)}$$

Since this condition must hold for all combinations of θ and $\bar{\theta}$, Eq. (A5) implies (for $\bar{\theta} - \theta = \pi/2$)

$$\boxed{\frac{u^2}{a^2} - 1 > 0}, \text{ for x to be the marching direction} \qquad \text{(A6)}$$

Eq. (A6) is a special case of Eq. (5) in Section II.

Acknowledgement

This work was supported in full by NASA Langley Research Center under Contract NAS1-15820.

References

1. Marconi, F., Salas, M., and Yeager, L., "Development of a Computer Code for Calculating the Steady Super/Hypersonic Inviscid Flow Around Real Configurations, Vol. I — Computational Techniques," NASA CR 2675.
2. Kutler, P., "Computation of Three-Dimensional, Inviscid Supersonic Flows," in Lecture Notes in Physics 41, Springer-Verlag, New York, 1975.
3. Siclari, M.J., "Investigation of Cross Flow Shocks on Delta Wings in Supersonic Flow," AIAA J., Vol. 18, No. 1, January 1980, p. 85.
4. Grossman, B., "Numerical Procedure for the Computation of Irrational Conical Flows," AIAA J., Vol. 17, No. 8, 1979.
5. Grossman, B. and Siclari, M.J., "The Nonlinear Supersonic Potential Flow over Delta Wings," AIAA Paper No. 80-0269, January 1980.
6. Siclari, M.J., "Computation of Nonlinear Supersonic Potential Flow Over Three-Dimensional Surfaces," AIAA Paper No. 82-0167, presented at the AIAA 20th Aerospace Sciences Meeting, Orlando, Florida, Jan. 82.
7. Shankar, V., "A Conservative Full Potential, Implicit, Marching Scheme for Supersonic Flows," to appear in AIAA Journal, November 1982.
8. Carmichael, R.L., and Erickson, L.L., "Pan Air - A Higher Order Panel Method for Predicting Subsonic or Supersonic Linear Potential Flows About Arbitrary Configurations," AIAA Paper No. 81-1255.
9. Jameson, A., "Transonic Potential Flow Calculations using Conservation Form," AIAA Second Computational Fluid Dynamics Conference Proceedings, 1975, pp. 148-155.
10. Lax, P.D., "Weak Solutions of Nonlinear Hyperbolic Equations and Their Numerical Computation," Communications on Pure and Applied Mathematics, Vol. 7, No. 1, 1954, pp. 159-193.
11. Steger, J.L. and Sorenson, R.L., "Automatic Mesh-Point Clustering Near a Boundary in Grid Generation with Elliptic Partial Differential Equations," Journal of Computational Physics, Vol. 33, No. 3, December 1979, p. 405.
12. Holst, T.L., "Fast, Conservative Algorithm for Solving the Transonic Full Potential Equation," AIAA Journal, Vol. 18, No. 12, Dec. 1980, pp. 1431-1439.
13. Steger, J.L. and Caradona, F.X., "A Conservative Implicit Finite Difference Algorithm for the Unsteady Transonic Full Potential Equation," FSI Report 79-04, December 1979.
14. Miller, D.S., Landrum, E.J., Townsend, J.C. and Mason, W.H., "Pressure and Force Data for a Flat Wing and a Warped Conical Wing Having a Shockless Recompression at Mach 1.62," NASA TP 1759, April 1981.
15. Townsend, J.C., "Pressure Data for Four Analytically Defined Arrow Wings in Supersonic Flow," NASA TM 81835, September 1980.

1. Report No.	2. Government Accession No.	3. Recipient's Catalog No.
NASA CR-166078		

4. Title and Subtitle	5. Report Date
NONLINEAR POTENTIAL ANALYSIS TECHNIQUES . . FOR SUPERSONIC/HYPERSONIC CONFIGURATION DESIGN	March 25, 1983
	6. Performing Organization Code

7. Author(s)	8. Performing Organization Report No.
W.C. Clever and V. Shankar	NA-82-1170
	10. Work Unit No.

9. Performing Organization Name and Address	11. Contract or Grant No.
Rockwell International P. O. Box 92098 Los Angeles, California 90009	NAS1-15820
	13. Type of Report and Period Covered
12. Sponsoring Agency Name and Address	Contractor report
National Aeronautics and Space Administration Langley Research Center Hampton, Virginia 23665	14. Sponsoring Agency Code

15. Supplementary Notes

Technical monitors: Noel Talcott and Kenneth Jones
Final Report

16. Abstract

Approximate nonlinear inviscid theoretical techniques for predicting aerodynamic characteristics and surface pressures for relatively slender vehicles at moderate hypersonic speeds were developed. Emphasis was placed on approaches that would be responsive to preliminary configuration design level of effort. Second order small disturbance and full potential theory was utilized to meet this objective.

Numerical pilot codes were developed for relatively general three dimensional geometries to evaluate the capability of the approximate equations of motion considered. Results from the computations indicate good agreement with higher order solutions and experimental results for a variety of wing, body, and wing-body shapes for values of the hypersonic similarity parameter $M\delta$ approaching one. Case computational times of a minute were achieved for practical aircraft arrangements.

17. Key Words (Suggested by Author(s))	18. Distribution Statement
Aerodynamic theory Potential analysis Supersonic/Hypersonic	[illegible] Distribution

19. Security Classif. (of this report)	20. Security Classif. (of this page)	21. No. of Pages	22. Price
Unclassified	Unclassified	82	

End of Document